SYNTHETIC FERRIMAGNETS AND MAGNETO-PLASMONIC STRUCTURES FOR ULTRAFAST MAGNETIZATION SWITCHING

by

Bradlee Beauchamp

A Dissertation

Submitted to the Faculty of Purdue University

In Partial Fulfillment of the Requirements for the degree of

Doctor of Philosophy

School of Materials Engineering

West Lafayette, Indiana

August 2020

THE PURDUE UNIVERSITY GRADUATE SCHOOL
STATEMENT OF COMMITTEE APPROVAL

Dr. Ernesto E. Marinero, co-chair

School of Materials Engineering

Dr. David Bahr, co-chair

School of Materials Engineering

Dr. Supriyo Datta

School of Electrical and Computer Engineering

Dr. Shriram Ramanathan

School of Materials Engineering

Approved by:

Dr. David Bahr

To my parents and family for always believing in me, to my partner for her unwavering support and love, and to my pets for their unconditional love.

ACKNOWLEDGMENTS

tunneling measurements. I extend my thanks also to Dr. Andreas Berger at the Nanoscience Research Center, Spain for magneto-optic measurements of garnet materials.

A special thanks is given to all the members of the Birck Nanotechnology Center that have helped make facility such a special place to work. Thank you especially to Dr. Neil Dilley for providing me your guidance and expertise regarding magnetic characterization and film growth. I would also like to thank Dave Lubelski for training me and providing guidance regarding sputter deposition. Thank you to Dr. Alexander Kildishev for providing the computing resources to employ COMSOL finite element analysis modelling software. Additional members of Birck that I would like to thank for training me and advising me include Dan Hosler, Tim Miller, Joon Park, Bill Rowe, Jeremiah Shepherd, Dr. Yi Xuan, and Dr. Nithin Raghunathan.

TABLE OF CONTENTS

LIST OF TABLES

LIST OF FIGURES

LIST OF ABBREVIATIONS

AF	antiferromagnetic
AOS	all-optical switching
BIG	bismuth iron garnet
cc	cubic centimeter
CIPT	current-in-plane tunneling
CMOS	complementary metal-oxide-semiconductor
CoCrPt	cobalt chromium platinum
CoCrPtTa	cobalt chromium platinum tantalum
CoFeB	cobalt iron boron
$CoFe_2O_4$	cobalt ferrite
EXAFS	extended x-ray absorption fine structure
FEA	finite element analysis
FM	ferromagnet
FMR	ferromagnetic resonance
FOM	figure of merit
fs	femtosecond
FWHM	full width at half maximum
GdFeCo	gadolinium iron cobalt
GGG	gadolinium gallium garnet
GHz	gigahertz
GMR	giant magnetoresistance
IEC	Interlayer exchange coupling
IFE	inverse Faraday effect
IP	in-plane
LLG	Landau-Lifshitz-Gilbert
LLGS	Landau-Lifshitz-Gilbert-Slonczewski
LSPR	localized surface plasmon resonance
MgO	magnesium oxide

MOKE	magneto-optic Kerr effect
MPS	magneto-plasmonic stack
MTJ	magnetic tunnel junction
nm	nanometers
NPS	non-plasmonic stack
OMF	opto-magnetic field
OP	out-of-plane
PLD	pulsed laser deposition
PMA	perpendicular magnetic anisotropy
ps	picosecond
RE	rare-earth
RKKY	Ruderman-Kittel-Kasuya-Yosida
RTA	rapid thermal annealing
SFM	synthetic ferrimagnet
Si_3N_4	silicon nitride
SiO_2	silicon dioxide
SOT	spin-orbit torque
SPP	surface plasmon polariton
STT	spin-transfer torque
SQUID	superconducting quantum interference device
TbFeCo	terbium iron cobalt
TEM	transmission electron microscopy
THz	terahertz
TiN	titanium nitride
TM	transition metal
TMR	tunneling magnetoresistance ratio
VSM	vibrating-sample magnetometer
XAS	x-ray absorption spectroscopy
XMCD	x-ray magnetic circular dichroism
XRD	x-ray diffraction
ZnO	zinc oxide

ABSTRACT

The response time of magnetization switching in current spintronic devices is limited to nanosecond timescales due to the precessional motion of the magnetization during reversal. To overcome this limit two routes of investigation leading to novel recording and logic devices are considered in this thesis: 1) Magnetic tunnel junction structures where the recording and reference layers are replaced by synthetic ferrimagnets and switching is induced by spin transfer torque and 2) Hybrid magneto-photonic devices where switching is induced by plasmon-enhanced all-optical switching. To circumvent limitations of the materials and magnetic properties of CoFeB, the most utilized alloy in spintronics, hcp-CoCrPt, a material that exhibits superior perpendicular anisotropy and thermal stability, is chosen as the ferromagnetic electrode in this work. Whereas actual devices based on the two schemes aforementioned are still in the process of being fabricated, through collaborative work with our international collaborators, this thesis describes fundamental magnetic and structural characterization needed for the realization of said ultrafast switching devices. The magnetic switching behavior of CoCrPt-Ru-CoCrPt synthetic ferrimagnets with perpendicular magnetic anisotropy have been studied in the temperature range from 2K to 300K. It was found that two sets of magnetic transitions occur in the CoCrPt-Ru-CoCrPt ferrimagnet systems studied. The first set exhibits three magnetization states in the 50K – 370K range, whereas the second involves only two states in the 2K and 50K range. The magnetic hysteresis curves of the synthetic ferrimagnet are assessed using an energy diagram technique which accurately describes the competition between interlayer exchange coupling energy, Zeeman energy, and anisotropy energy in the system. This energy diagram analysis is then used to predict the changes in the magnetic hysteresis curves of the synthetic ferrimagnet from 200K to 370K. This represents the potential operation temperature extrema that a synthetic ferrimagnet could be expected to operate at, were it to be utilized as a free layer in a memory or sensor spintronic device in the device configuration described in this dissertation.

Circularly polarized fs laser pulses generate large opto-magnetic fields in magnetic materials, through the inverse Faraday effect. These fields are attributed to be largely responsible for achieving ultrafast all-optical magnetization switching (AOS). All experimental demonstrations of AOS thus far have been realized on thin films over micron-sized irradiated regions. To achieve magnetization switching speeds in the ps and potentially fs time regimes, this work proposes the

use of surface plasmon resonances at the interface of hybrid magneto-photonic heterostructures. In addition to the ability of plasmon resonances to confine light in the nm scale, the resonant excitation can largely enhance induced opto-magnetic fields in perpendicular magnetic anisotropy materials. This requires strong spin-photon coupling between the plasmonic and the magnetic materials, which thus requires the minimization of seed layers used for growth of the magnetic layer. This work reports on the development of ultrathin (1 nm thick) interlayers to control the growth orientation of hcp-Co alloys grown on the refractory plasmonic material, TiN, to align the magnetic axis out-of-plane. CoCrPtTa seed layers down to 1 nm were developed to seed the growth of CoCrPt, and the dependence of the quality of the CoCrPt is investigated as Ta composition is varied in the seed layer. Whereas bismuth iron garnet (BIG) meets the magneto-optical requirements for a hybrid magneto-photonic material, its magnetic and structural properties are highly sensitive to the Bi:Fe ratio and must be grown epitaxially on single crystalline substrates. Therefore, in this work we have investigated alternative materials that offer superior magnetic properties and are amenable to growth on inexpensive substrates. Opto-magnetic field enhancements up to 2.6x in Co-ferrite magneto-photonic heterostructures have been obtained via finite element analysis modelling. Alternative materials for plasmon-enhanced all-optical switching such as Co/Pd multilayers have also been investigated. Successful growth of Co/Pd multilayers on TiN using ultrathin Ti interlayers has been achieved.

1. INTRODUCTION

1.1 Towards Ultrafast Magnetism in Memory and Logic Devices

Modern spin-transfer torque (STT) and spin-orbit torque (SOT) - switchable magnetic tunnel junctions (MTJ), are examples of spintronic devices, providing non-volatility, moderate magnetization switching speeds, and high information storage densities; this makes the MTJ an attractive candidate for advancing current computing and logic devices. The workhorse of MTJ devices has been the CoFeB-MgO materials system and in 2010 a device with the following characteristics was described in the literature: a tunneling magnetoresistance (TMR) ratio of 120%, a switching current of 49 µA, and high thermal stability down to 40 nm diameter nanopillars [1]. STT and SOT magnetization switching rely on the injection of charge currents into magnetic thin films to generate spin polarized currents that interact via transfer of angular momentum with the macroscopic magnetization. When the spin current is sufficiently large and the spin orientation is opposite to the magnetization, as first predicted by Slonczewski in 1996 [2], magnetization reversal can ensue. However, the magnetization reversal process in STT and SOT, as in the case of when applying and external magnetic field, occurs via precessional motion [3], and this is limited typically to nanosecond time scales (GHz frequencies). Sub-200ps switching in an MTJ with in-plane magnetization has been reported by Zhao *et al*. [4] for in-plane CoFeB-MgO based MTJs. In their work they report that reduction of the demagnetization field in the free layer by the interface perpendicular anisotropy, reduces the STT switching time. Current CMOS devices switch a couple of orders of magnitude faster (picoseconds) and operate in the THz range, thus creating a gap between spintronics and CMOS devices for memory and logic computing operations.

A comparison of switching speeds and energy required of potential devices for beyond-CMOS replacement has been conducted by Nikonov *et al*. [5]. In Fig. 1.1 a comparison is made using a 32-bit adder as a benchmark circuit, of devices operating under different physical principles and include electronic, spintronic, ferroelectric, orbitronic, and straintronic devices. The switching delay is plotted in picoseconds (ps) and characterizes the speed of the device. The energy required for switching is also plotted in femto-Joules. Fig. 1.1 demonstrates that spintronics-based devices at the time of the study were still far behind the operational speeds seen in some FET devices. The energy required for switching is also much larger.
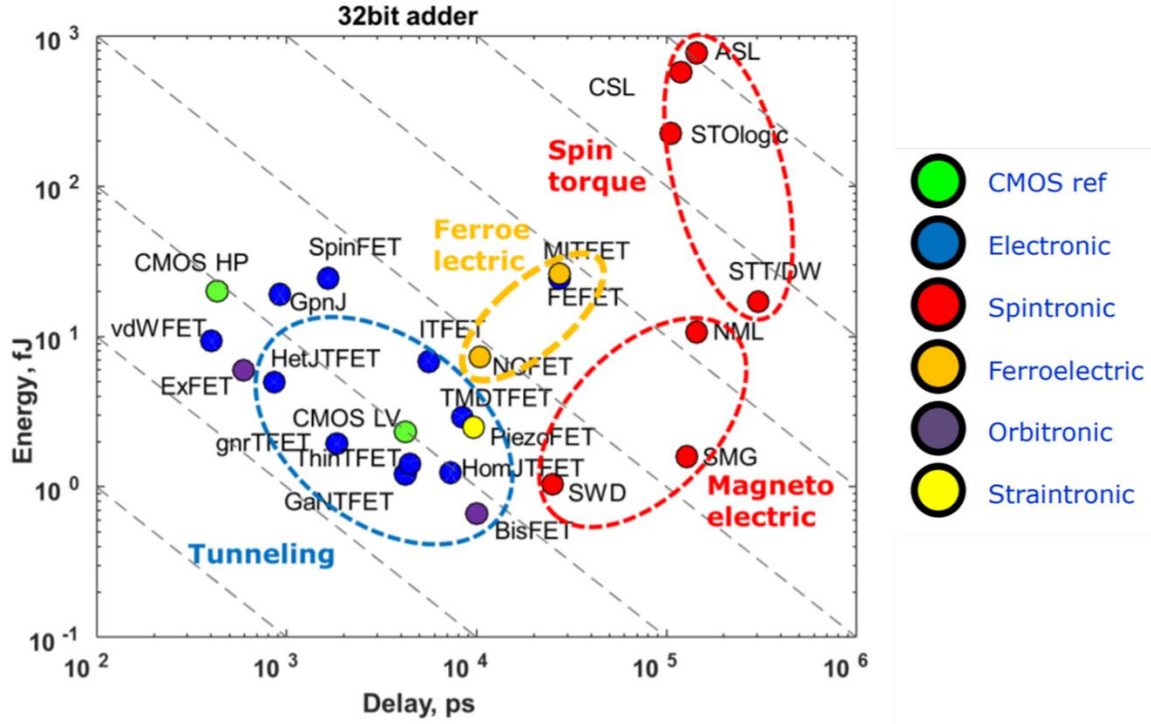
Figure 1.1 Comparison of switching energy (fJ) and delay (ps) for potential beyond-CMOS replacement devices incorporated into a 32-bit adder. Figure from [5] and reprinted with permission. © 2015 IEEE

It has been reported in ref. [6] that STT in MTJs causes precessional reversal of the magnetization and that the switching speed is comparable to magnetic field-driven switching processes. Increasing the driving force for switching by increasing the magnetic field to multi-Tesla regimes would be impossible in existing devices. Increasing spin current to overdrive limits are also impractical in MTJ devices since it can cause breakdown in the MgO tunnel barrier [7]. Therefore, while current spintronics devices are promising to meet the need for higher-capacity data storage, significant improvements in switching speeds need to be realized. A plot of processing speed versus time is shown in Fig. 1.2 and illustrates how nanophotonics and plasmonics can help sustain the rise of computational speed.

The dynamics of magnetization precessional motion is described by the Landau-Lifshitz-Gilbert (LLG) equation (Eq. 1.1) [8]. In this equation m, H_{eff}, α, and γ refer to the magnetization vector, the effective magnetic field vector, the Gilbert damping constant, and the gyromagnetic ratio, respectively. The Gilbert damping constant term is multiplied by cross product of the magnetization and its time derivative. This parameter determines the rate at which the

magnetization relaxes to equilibrium. In 1996, the LLG equation was expanded to account for STT induced by flowing current through the ferromagnet [2], forming the Landau-Lifshitz-Gilbert-Slonczewski (LLGS) equation. It has been demonstrated that the critical current density required for STT switching is proportional to the damping constant [2]. Specifically, the critical current density required for switching is given by Eq. 1.2 [1], where e is the electron charge, μ_B is the Bohr magnetron constant, g is a function that depends on the spin polarization of current and the angle between the magnetic layers of the MTJ [2], [9], γ is the gyromagnetic ratio, α is the damping constant, H_K is the anisotropy field, and V is the volume of the recording layer. The STT needs to overcome the thermal energy barrier, $E = \frac{M_S H_K V}{2}$, for magnetization reversal. The thermal stability of the magnetization state is characterized by the figure-of-merit, $E/k_B T$, where T is temperature and k_B is the Boltzmann constant. This ratio should be larger than 60 to ensure thermal stability > 10 years. There exists a dilemma between keeping the thermal stability constant high for long retention of the magnetization order while keeping it low enough to ensure low switching currents. Increasing the thermal stability by utilizing high M_S and H_K materials will also increase the critical switching current (Eq. 1.2).

$$\frac{dm}{dt} = -\gamma m \times H_{eff} + \alpha m \times \frac{dm}{dt} \qquad (1.1)$$

$$I_{C0} = \alpha \frac{\gamma e}{\mu_B g} M_S H_K V = 2\alpha \frac{\gamma e}{\mu_B g} E \qquad (1.2)$$

To reduce the switching times in MTJ devices, ferromagnetic electrodes such as CoFeB are typically used due to the small value of their damping parameter [1]. Efforts to decrease the switching time have also been successfully demonstrated by reducing the demagnetizing field for the free layer, which allows for easier canting of the magnetization vector, nucleating reversal in these areas [4]. However, the materials used for these solutions are still constrained to the use of the CoFeB/MgO MTJ structure. This work will focus on alternative methods and materials for achieving ultrafast magnetization switching in such devices.
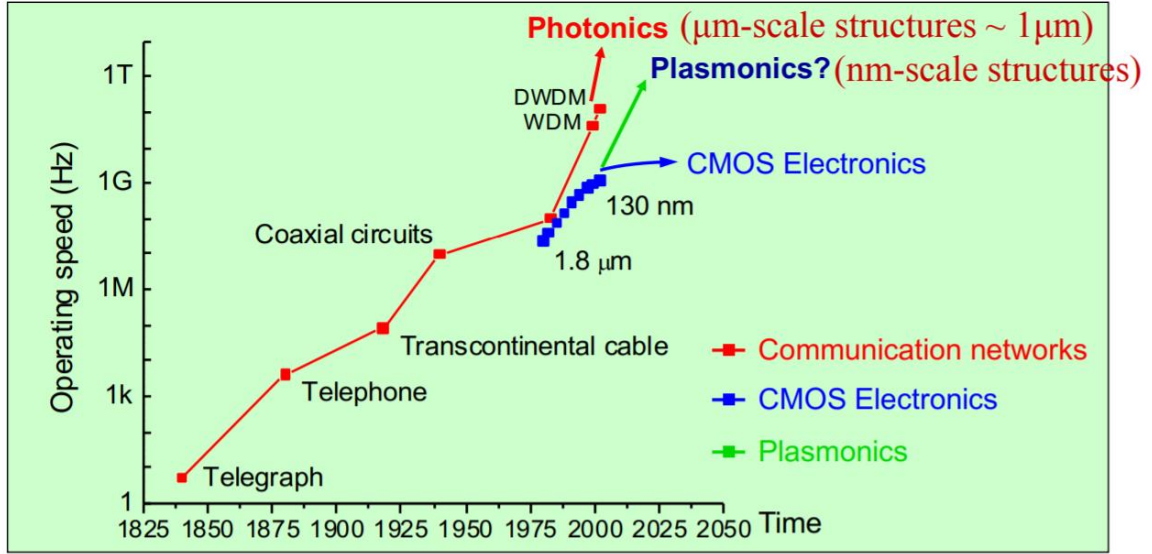
Figure 1.2 Operating speed of telecommunications devices over time. Chart courtesy of Professor V. Shalaev.

1.2 Optical Interaction with Magnetism

As of the year 2016, two decades have passed since the demonstration of all-optical demagnetization of a nickel film via 60 femtosecond (fs) laser pulses [10]. This demonstration sparked much interest and research into the physics of ultrafast magnetism and the interaction of light with the lattice. At such short interaction timescales, the magnetic material is in a nonequilibrium state where properties such as the magnetic anisotropy and the exchange interaction of the electron spins are time-dependent. An area of active research investigates how fast and between which thermodynamic reservoirs angular momentum can be exchanged (lattice, electrons, and spins) [11]. The timescales involved with interactions of the magnetization with applied magnetic fields vs. ultra-short laser pulses [11] are shown in Fig. 1.3. Femtosecond laser pulses are attractive since the time scale of the interaction could lead to switching that is shorter than half of the precessional limit (100-1000 ps).

22
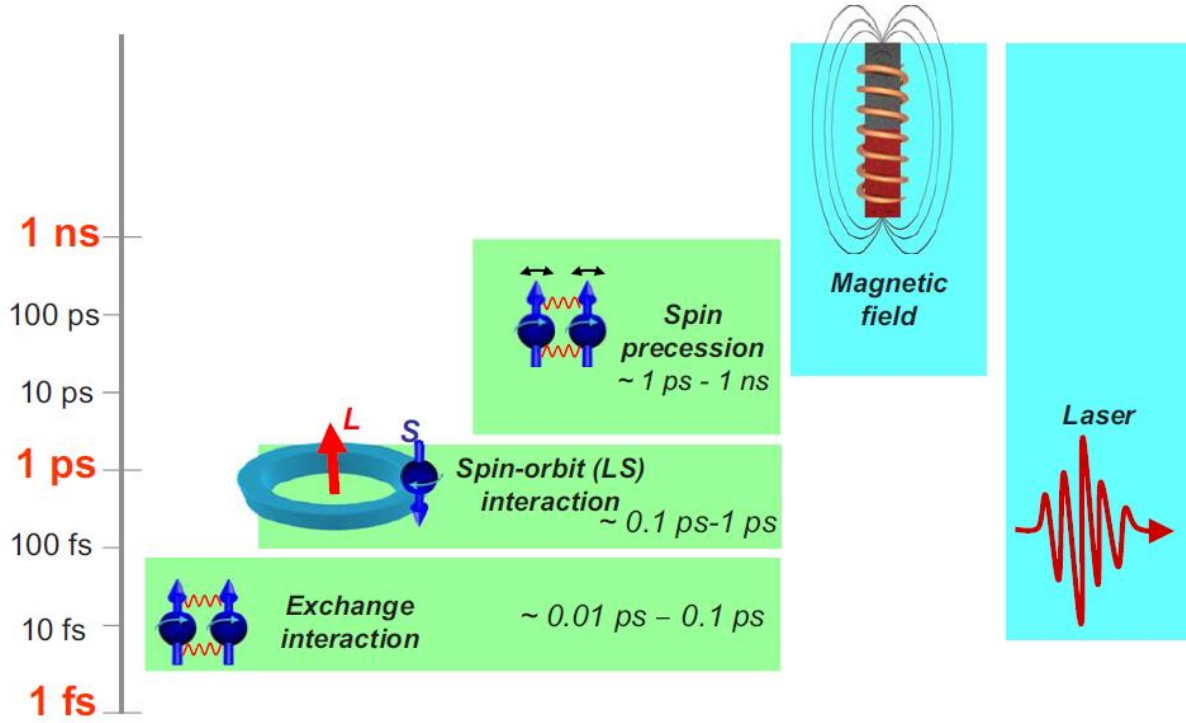
Figure 1.3 The time scales of phenomena in magnetism shown in green are compared to the switching mechanism (magnetic field vs. a laser pulse). Laser pulses can enable magnetic interactions to be used in the sub-picosecond regime. Figure from [11] and reprinted with permission, copyright American Physical Society.

In 2007 it was demonstrated that a single 40 fs circularly polarized laser pulse could switch the magnetization of GdFeCo thin films [12]. Depending on the helicity of the light (left or right circularly polarized), the magnetization was switched in a deterministic direction (Fig. 1.4). The mechanism by which the laser pulse switches the magnetization is through the inverse Faraday effect (IFE). This effect describes how circularly polarized light induces a magnetic moment ($M = \frac{\lambda V}{2\pi c}(I_R - I_L)$) in a magnetic material due to the angular momentum-flux caused by the light [13] where the I's are the intensities of the left/right circularly polarized light, V is the Verdet constant of the material, and λ is the wavelength of light. As reported by Beletelov et $al.$, $I_R - I_L \sim |Im(E\ x\ E^*)|$, which characterizes the dc magnetic field induced in the material. To increase M, one could find a material with large V. Another way would be to increase either the intensity of the electric field or have circularly polarized light (not elliptical); we will see later in this report that plasmonics can be used to achieve both.

The area whose magnetization was reversed by the laser pulse in ref. [12] corresponded to the spot size of the laser (~100 µm). The smallest areas that can be reversed using imaging lenses are limited by the physics of diffraction, thus, for 500 nm light, this is ~250 nm. This is over one order of magnitude larger than the bit size in current advanced magnetic recording devices. Therefore, and approach is needed to effect all-optical magnetization switching in the nanoscale in spintronic devices for THz computing and beyond. Nanoplasmonics enables the manipulation of light beyond the diffraction limit of light, and through the generation of surface plasmon resonances and associated large electric field intensity enhancements, the possibility of generating very large opto-magnetic fields in magnetic materials.
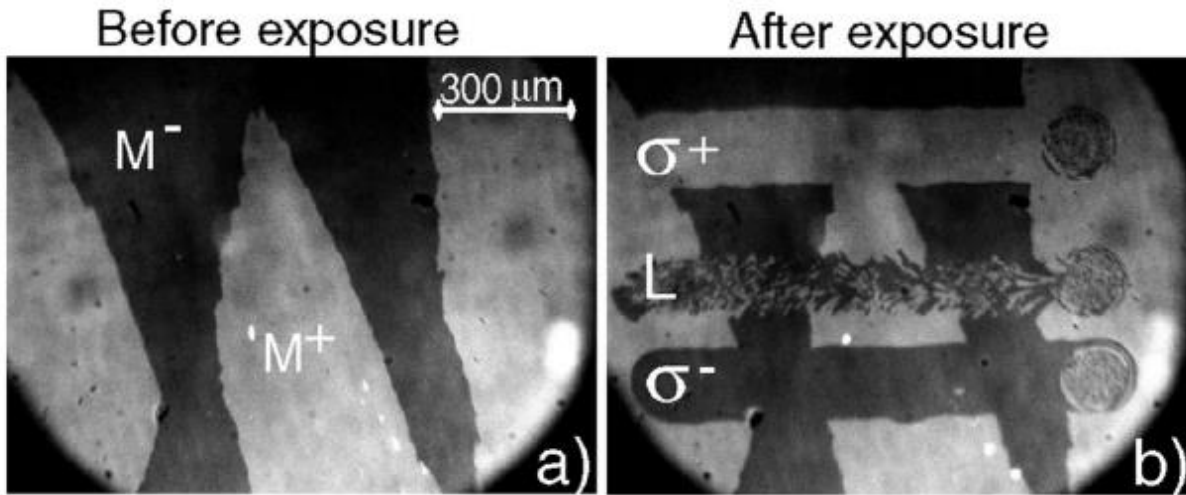
Figure 1.4 From Stanciu *et al*. [12] The effect of ultrashort polarized laser pulses on magnetic domains in $Gd_{22}Fe_{74.6}Co_{3.4}$. (a) Magneto-optical image of the initial magnetic state of the sample before laser exposure. White and black areas correspond to up (M^+) and down M^-) magnetic domains, respectively. (b) Domain pattern obtained by sweeping at low speed (~30 µm/s) linear (L), right-handed (σ^+), and left-handed (σ^-) circularly polarized beams across the surface of the sample, with a laser fluence of about 11.4 mJ/cm^2. The central area of the remaining spots at the end of each scan line consists of small magnetic domains, where the ratio of up to down magnetic domains is close to 1. Reprinted with permission, copyright 2007 American Physical Society.

1.3 Plasmonics and Spintronics

Belotelov *et al*. [13] reported 10-50x enhancement of the IFE by modelling structures that support surface plasmon polariton (SPP) propagation (Fig. 1.5). Figure 1.5a shows a perforated dielectric material on top of continuous metal and paramagnetic layers. Whereas, Fig. 1.5b shows

only the perforated metal layer on top of a continuous paramagnetic layer. Both structures are designed to support SPP propagation. SPP is localized at the interface between the metal and the paramagnetic material in both Fig. 1.5 (a) and (b). The results of the modelling can be seen in Fig. 1.6, which shows 10-50x enhancement of both the intensity of the electric field (**EE***) and the **Im(ExE*)**, corresponding to the electric field intensity and the dc magnetic field, respectively. The results in Fig. 1.6 are normalized to a single paramagnetic layer without the plasmonic upper layer. This enhancement has been confirmed by Hamidi *et al.* [14] where similar perforated structures were modelled with Fourier modal method and dc magnetic field enhancement of 10-70x was reported. The enhanced fields are also confined to areas around 100nm in this case and could be tailored to other sizes.
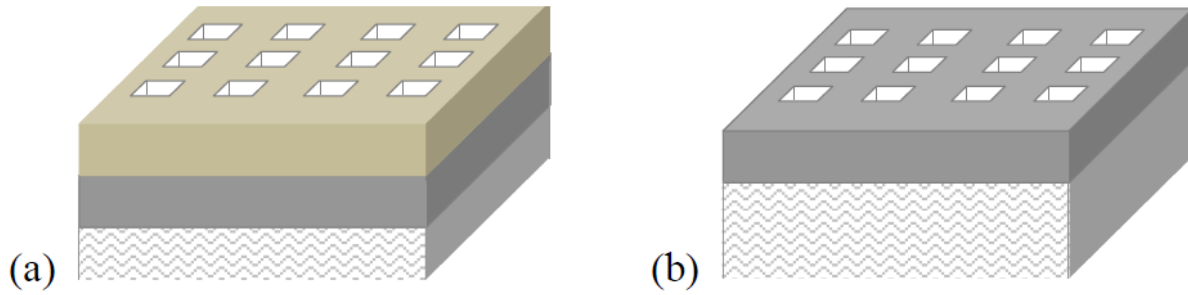
Figure 1.5 From Belotelov *et al.*[13] Schematic of the plasmonic heterostructures: (a) perforated dielectric/metal/paramagnetic; (b) perforated metal/paramagnetic.
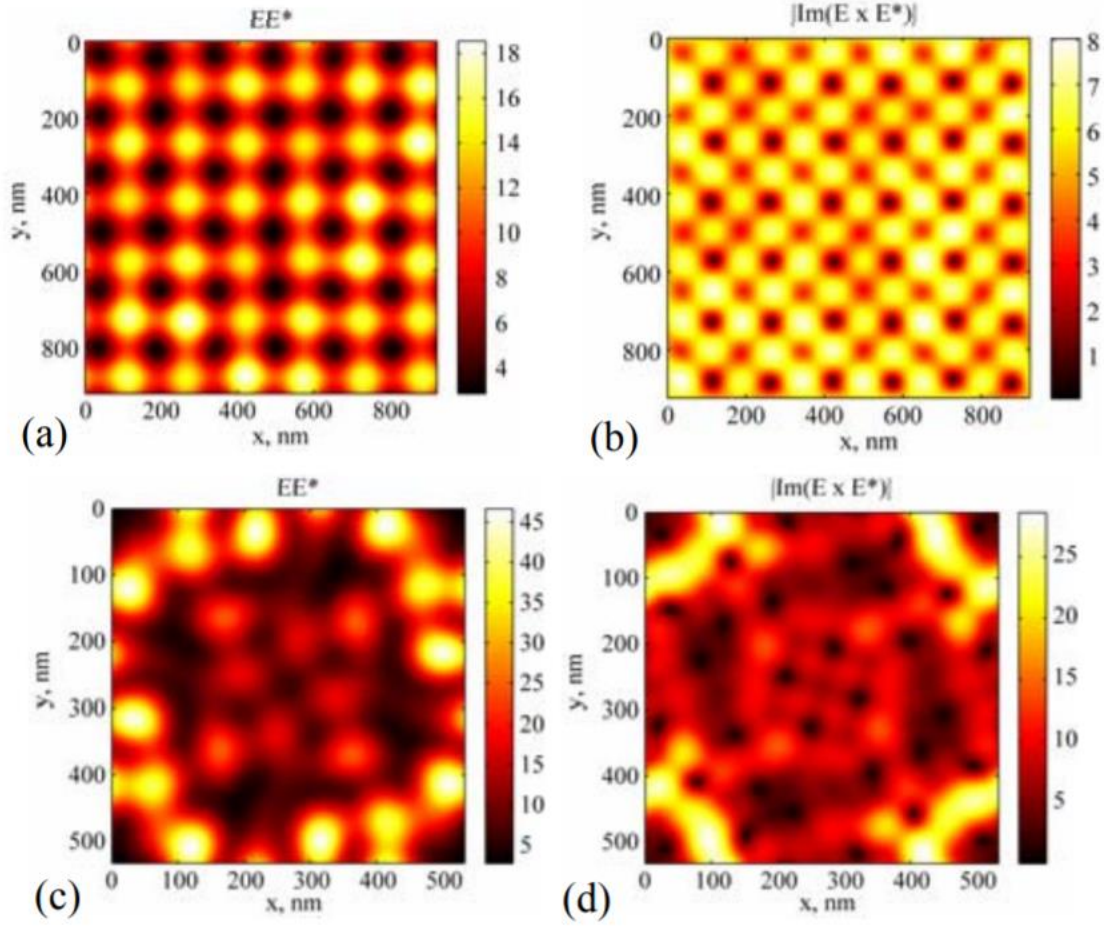
Figure 1.6 Contour plots for (a), (c) I and (b), (d) m at 10nm depth inside the paramagnetic across a unit lattice normalized on their values for a single paramagnetic film without plasmonic upper layer. (a) and (b) correspond to the structure shown in Fig. 1.5 (a); (c) and (d) correspond to the structure shown in Fig. 1.5 (b). Figure from [13].

Liu *et al*. [15] reported nanoscale confinement of fs laser irradiation by using pairs of Au plasmonic nano-antennas for AOS. In this case the pulses used were slightly longer than 500 fs. The magnetic material employed was ferrimagnetic terbium iron cobalt (TbFeCo), which has higher magnetic anisotropy than GdFeCo and can sustain smaller magnetic domain sizes on. Using x-ray magnetic circular dichroism (XMCD) they imaged the magnetization changes in their samples (Fig. 1.7). Remarkably, they excited the nano-antennas using linearly polarized light and still observed magnetic switching. It was mentioned that AOS was possible with linearly polarized light (which is a linear combination of left and right circularly polarized light) in this material due to circular dichroism, where one polarization of light (either left or right) is absorbed more by the material than the other polarization of light. Thus, in this case AOS switching via linearly polarized

26

light is fundamentally similar to switching with circularly polarized light [16]. Figure 1.7 also shows that while the size of the switched magnetization is small, the location of the switching is not perfect due to compositional inhomogeneities in their TbFeCo films. This provides a demonstration on the use of plasmonics to confine light and affect magnetization switching.

Recently the work of Dutta *et al.* [17] at Purdue reported using numerical simulations, plasmonic-assisted opto-magnetic field enhancements of 10x by integrating titanium nitride (TiN - a plasmonic material) into a magneto-plasmonic nanostructure with both dielectric and metallic magnetic materials. This geometry, shown in Fig. 1.8, is much simpler to fabricate and could readily be integrated with spintronic structures such as MTJs. The enhancement is due to the light coupling with the TiN layer and creating localized surface plasmon resonance (LSPR) at the photonic/magnetic material interface. The enhancement using a dielectric magnetic material (bismuth iron garnet) was significantly larger than for metallic GdFeCo which has inferior optical properties that result in significant light absorption. This reduces the attainable enhancement of the opto-magnetic field. Figure 1.9 shows the enhancement in opto-magnetic field estimated in bismuth iron garnet (BIG) (~10x) over the case without plasmonic TiN.
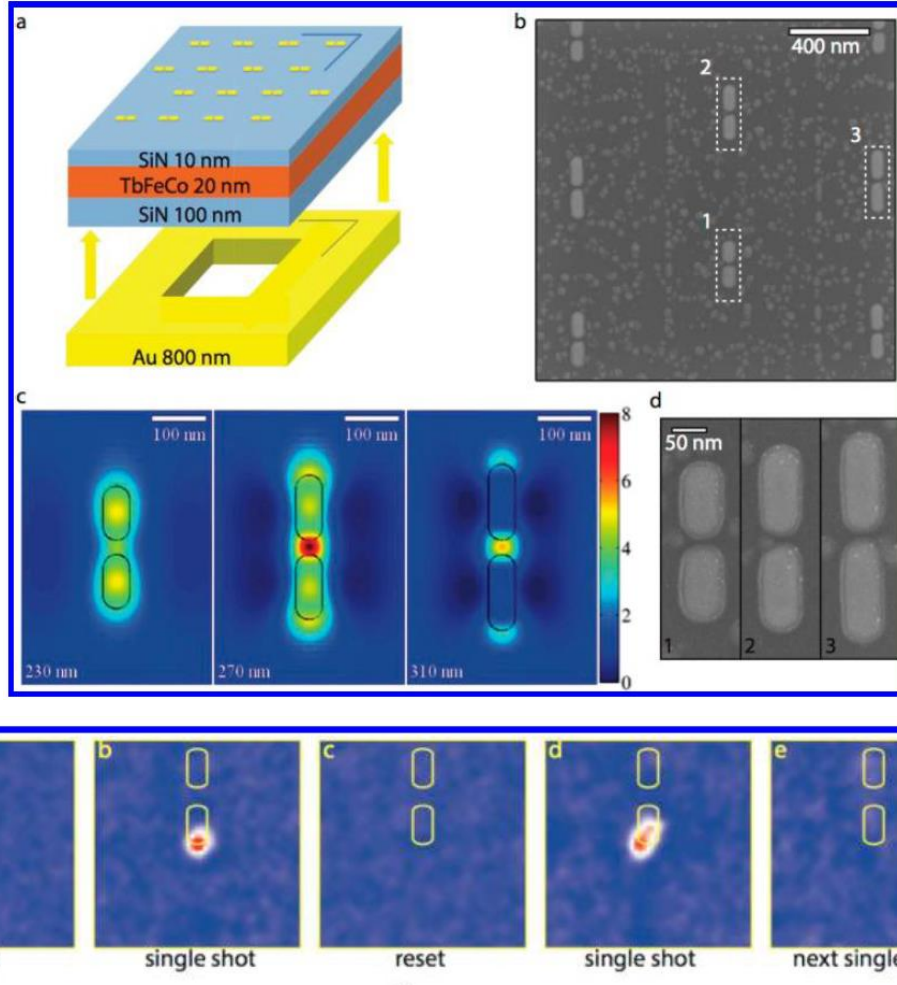
Figure 1.7 (Top) Layout of TbFeCo sample, plasmonic antennas, and holography mask. (Bottom) (a) Initial magnetic contrast around the selected antenna after being magnetic saturated in a field of 1.6T. The gold scale bar is 100 nm in length. (b) Magnetic contrast after first laser pulse of 3.7 mJ/cm^2. A small domain with a FWHM of 53.4 nm is switched. (c) The magnetization is reset again after using an external magnetic field. (d) Magnetic contrast after the first laser pulse of 4.0 mJ/cm^2 on the newly saturated sample. A domain of comparable size is shown in (b) is switched in the same region. (e) Magnetic contrast after a second laser pulse of 4.0 mJ/cm^2. The magnetization of the region switched in (d) is toggled back to its original state. Figure from [15]. Reprinted with permission, copyright 2015 American Chemical Society.
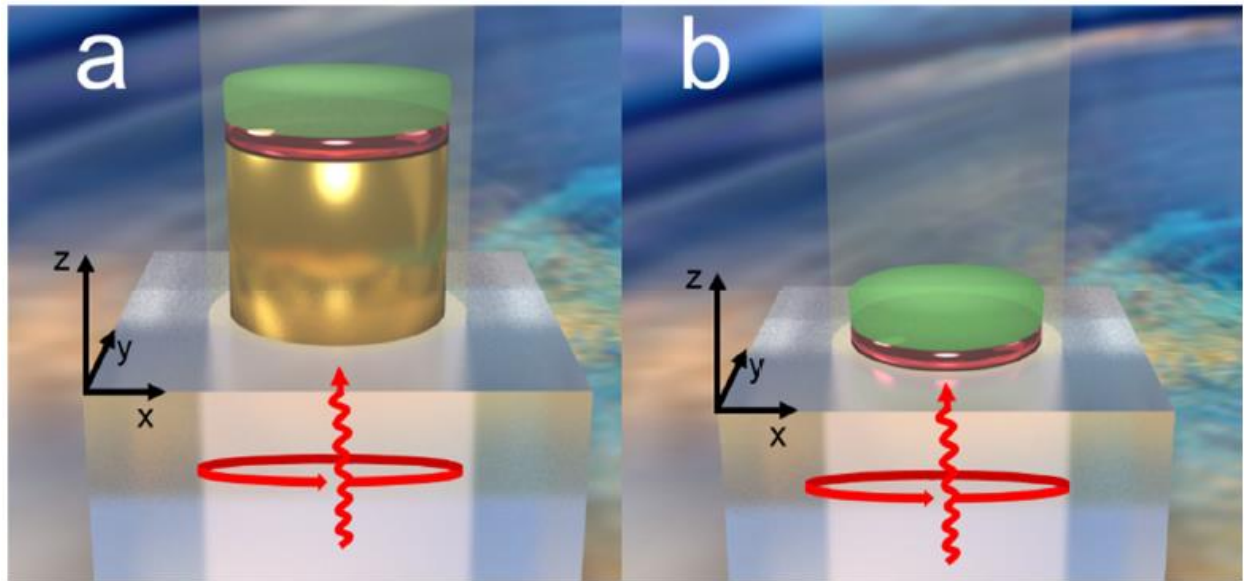
Figure 1.8 Magneto-plasmonic nanostructures: (a) MgO/TiN/BIG/Si_3N_4 (b) MgO/BIG/Si_3N_4. Circularly polarized light is incident through the MgO substrate. Figure from [17].
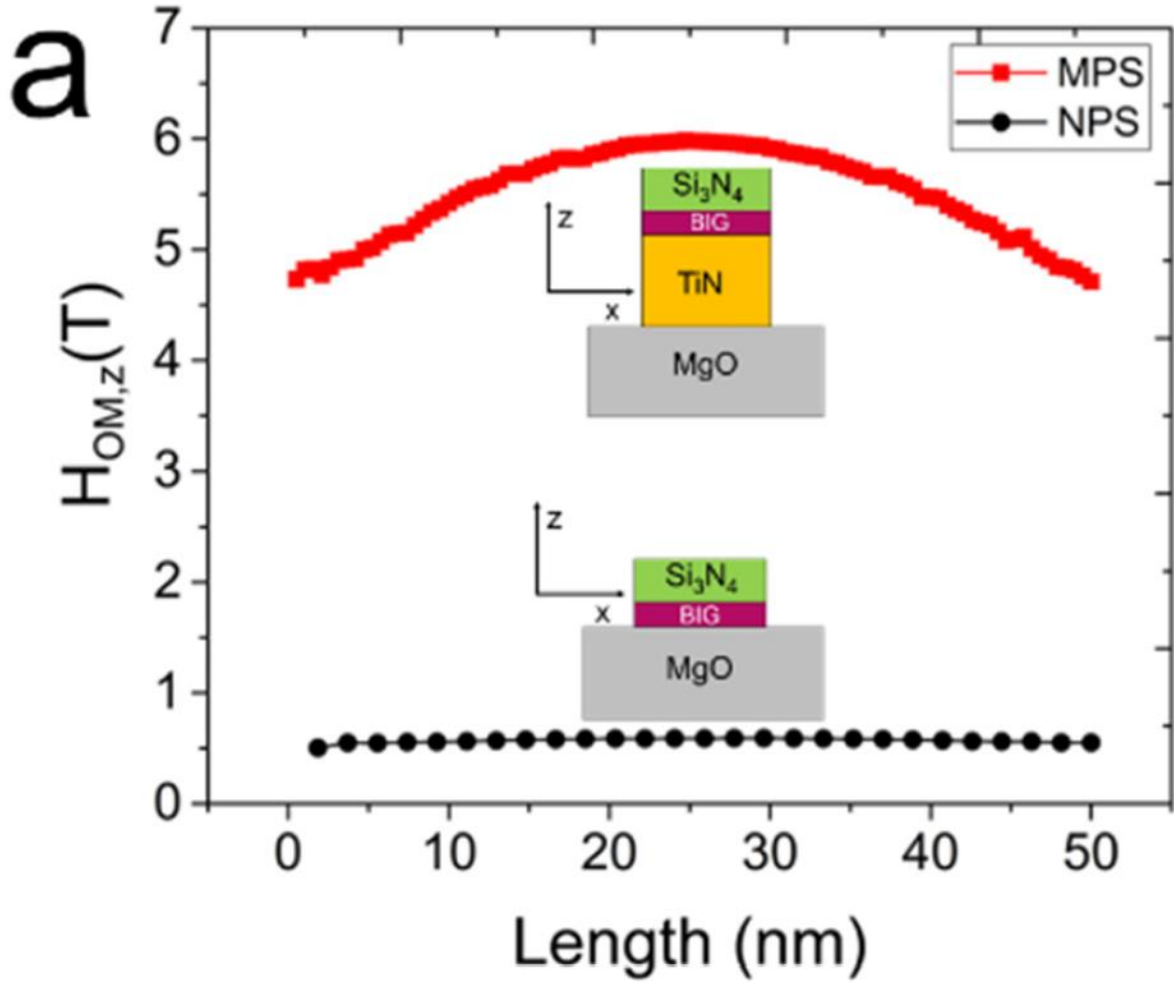
Figure 1.9 Comparison of the z-component of the opto-magnetic field intensity along the x-axis of BIG-TiN interface for a 10nm thick BIG layer in the MPS (nanomagnet with TiN resonator) and NPS (only nanomagnet) sample. Illumination is with circularly polarized light of intensity 1mJ/cm^2 at 710nm wavelength under normal incidence. Figure from [17].

1.4 Synthetic Ferrimagnet Based Spintronics

The switching speed of spintronic devices utilizing single ferromagnetic layers is typically limited to GHz frequencies. The energy required to switch such magnetic layers also becomes prohibitively large at thresholds above these limits [18], [19]. It has been observed that antiferromagnetic materials have magnetic resonances up to THz scales due to the dynamics of the two interacting sublattices; because of the strong exchange interaction, the dynamics of antiferromagnets are much faster than ferromagnetic dynamics [20]–[22]. These resonances enable ultrafast electrical writing speeds at lower required energy [22].

THz ferromagnetic resonance (FMR) has been predicted in synthetic antiferromagnetic trilayers that are controlled by STT [23]. In this study the magnetization dynamics of a spin-valve based STT oscillator with SFM free layer are simulated. Figure 1.10 shows the effect of the exchange coupling energy J_{EX}, and the thickness of the thinner magnetic layer that comprises the SFM (structure shown in Fig. 1.10c) influence the FMR as a function of input current. From this work it is evident that large J_{EX} allows for higher resonances to occur for a given spin current. Also, d_1 (the smaller component of the SFM) can be tuned to yield higher resonances. In this study the frequencies obtained were higher when the difference in thickness between the thick and thin ferromagnetic components of the SFM was increased.
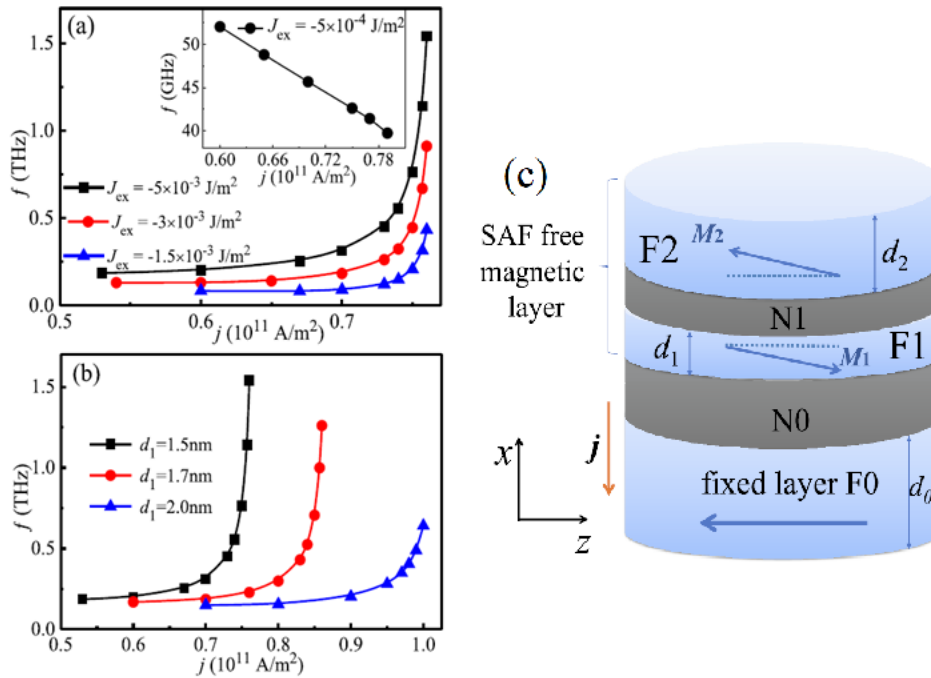
Figure 1.10 Dependence of the ferromagnetic resonance frequency of the thinner magnetic layer comprising the SFM (F1) on current density with respect to different (a) J_{ex} and (b) thickness of the thinner magnetic layer (d_1). (c) Structure of spin valve with SFM (F1/N1/F2) acting as the free magnetic layer. Figure from [23]. Reprinted with permission, copyright 2020 Elsevier.

1.5   Materials Challenges and Structure of Dissertation

Spintronics devices lag behind current complementary metal-oxide-semiconductor (CMOS) technology in terms of operation speed. This is due to the precession limit in single ferromagnets that are switched via applied magnetic fields and spin currents, which constrain the switching

speed to nanosecond timescales. Synthetic ferrimagnets with PMA offer a potential solution to this limit in speed, while maintaining the thermal stability necessary for high density recording devices.

This thesis will focus on two routes for the growth of magnetic materials and structures to overcome this hurdle in switching speed. One route involves incorporating SFM structures as the free layer in MTJ devices. The other route involves the growth and design of magneto-photonic devices which feature plasmon-enhanced opto-magnetic fields to achieve ultrafast switching speeds via AOS.

CoCrPt is an alloy with tunable magnetic properties and robust growth characteristics that can be utilized in such devices. The growth and characterization of CoCrPt thin films with hcp (0002) oriented growth parallel to the substrate plane will first be discussed. The utilization of this material in CoCrPt/Ru/CoCrPt SFMs will then be described, including the analysis of the exchange coupling energy and magnetic transitions in such structures.

The growth of CoCrPt on TiN films using ultrathin interlayers will allow these materials to be used in plasmon-enhanced magneto-photonic structures. The crystallographic and magnetic properties of these seed layers and how it affects CoCrPt growth will be discussed.

Finally, the optical and magneto-optical properties of CoCrPt films will be reported. The use of alternative materials will be discussed along with their advantages and disadvantages. Modelling of the optimized geometric arrays of such materials for magneto-photonic devices will be discussed using finite element analysis.

2. GROWTH AND MAGNETIC PROPERTIES OF CoCrPt AND CoCrPt/Ru/CoCrPt SYNTHETIC FERRIMAGNET TRILAYERS

2.1   Introduction

As mentioned in Chapter 1 antiferromagnet structures are promising materials candidates for ultrafast switching magnetic storage and logic devices. Until recently, antiferromagnetic materials were employed in MTJs mostly to provide an exchange bias to the reference layer (a single, magnetically hard layer) such that it is harder to reverse the magnetization via applied magnetic field or STT [24], [25]. Synthetic ferrimagnet (SFM) trilayers in recent years are being considered to replace the recording or reference layer ("free" or "fixed" layer, respectively) of the MTJ and similar devices [26], [27]. An uncompensated SFM structure is depicted in Fig. 2.1, where the net magnetization is non-zero due to the difference in the thickness of the constituent ferromagnetic layers. One advantage of SFMs as magnetic components in spintronic devices is that the net magnetization of the SFM is readily manipulated by adjusting the magnetic volume of the constituent layers. The point at which the opposing magnetizations cancel out is referred to as the compensation point. By reducing the net magnetization, the effects of the intrinsic demagnetizing energy are reduced. This leads to enhanced thermal stability as the demagnetizing energy opposes the magnetocrystalline anisotropy responsible for PMA and is especially important at high storage densities for MTJ devices [28]. Equation 2.1 describes the anisotropy (K) of a ferromagnet which is comprised of the bulk or magnetocrystalline anisotropy (K_b), the demagnetization energy M_S^2/μ_0, and the interface anisotropy K_i/t_F. The ferromagnet thickness is t_F, the saturation magnetization M_S, and μ_0 is the permeability of free space. Utilizing an SFM as the free layer in an MTJ also effectively reduces its magnetic volume requiring lower switching currents.

A basic magnetic tunnel junction consists of three layers: a magnetic fixed layer, a non-magnetic tunneling barrier, and a magnetic free layer (Fig. 2.2). The changes in magnetization state upon applying an external magnetic field are shown. The free layer requires a smaller coercive field to switch and is less stable than the so-called fixed layer. Depending on whether the magnetizations of the two magnetic layers are parallel or anti-parallel, the resistance will be low or high, respectively. The synthesis of free/fixed layers aims at rendering their magnetization orientation perpendicular to the substrate plane, a critical requirement for incrementing thermal

stability of magnetic nanostructures. An MTJ device's key figure-of-merit is the tunneling magnetoresistance ratio (TMR) which is the percent change of resistance change between the parallel and antiparallel magnetic orientations of the free and fixed layers. The TMR is defined as $TMR = \frac{R_{AP} - R_P}{P}$ where R_{AP} and R_P is the resistance of the MTJ in the anti-parallel and parallel state, respectively. Figure 2.2 depicts the resistance change in an MTJ as the field or current is swept [29], leading to smaller resistance in the parallel state and higher resistance in the anti-parallel state. Higher TMR makes it easier to read the magnetic state of the MTJ. As mentioned, today the free layer of MTJ's are switched using STT in the nanosecond regime. In this chapter film structures are grown for use in MTJ devices that could potentially overcome the precessional limit to magnetization switching.
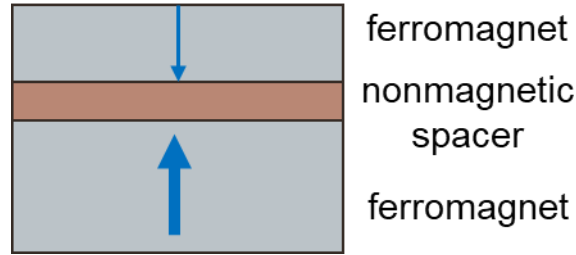
Figure 2.1 Cross-section of a synthetic ferrimagnet trilayers consisting of two ferromagnetic layers separated by a nonmagnetic spacer. The arrows indicate the magnetization orientation of each ferromagnet and the layers antiferromagnetically coupled.
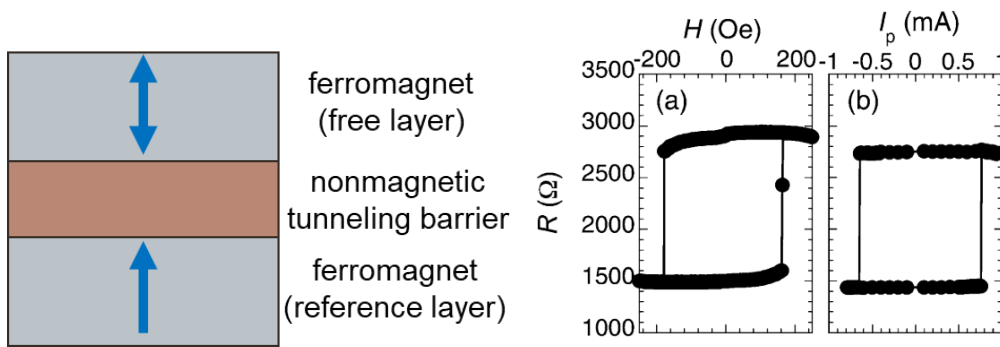
Figure 2.2 Left: Cross-section of typical MTJ structure consisting of two single FM materials separated by a nonmagnetic tunneling barrier (typically MgO). The FM material that is more (less) stable is considered the reference (free) layer. Right: Resistance vs field and resistance vs current for an MTJ structure showing a hysteretic change in resistance for parallel vs anti-parallel states of the MTJ. Figure from [29]. Reprinted with permission, copyright 2008, IEEE.

$$K = K_b - \frac{M_S^2}{\mu_0} + \frac{K_i}{t_F}$$

<div align="right">(2.1)</div>

Ferrimagnetic materials comprise atomic arrangements wherein the magnetic moment of the constituent atoms antiferromagnetically couple. One of the best-known examples in the area of memory devices are alloys of the rare-earth and the transitions metals (RE-TM) such as GdFeCo and TbFeCo. The magneto-optical properties of these alloys were the basis for optical storage information technology which gave birth to the re-writable CD. Altering the RE:TM ratio permits the engineering of important magnetic properties such as the net magnetization, the compensation point, the coercivity and the Curie point. Synthetic ferrimagnets also named synthetic antiferromagnets employ either identical or dissimilar magnetic layers that antiferromagnetically exchange couple via an intermediate metallic layer such as Ru. The exchange energy between the constituent layers can be manipulated by either changing the nature of the spacer layer (see Fig. 2.1) or the its thickness. It was first demonstrated by Parkin *et al.* in 1986 [30] that the exchange coupling strength changed in an oscillatory manner as the nonmagnetic interlayer thickness is varied in Fe/Cr superlattices. Later it was discovered that a similar phenomenon is also observed in Co/Ru, Co/Cr, and Fe/Cr superlattices [31] and that this oscillation in exchange strength also coincides with an oscillation in magnetoresistance. This effect was then observed as a general phenomenon for Fe, Co, Ni ferromagnetic layers coupled through 3d, 4d, and 5d transition metals [32]. The discovery of the giant magnetoresistance in these SFMs led to the award of the 2007 Nobel Prize for Physics to Albert Fert and Peter Grünberg and launched the era of spintronic devices.

Interlayer exchange coupling (IEC) arises from the Ruderman-Kittel-Kasuya-Yosida mechanism which is a coupling induced through the conduction electrons and was later applied to synthetic antiferromagnetic trilayers [33]. The IEC strength was found to oscillate as the nonmagnetic spacer thickness is increased (as is seen in Fig. 2.3), due to an induced spin polarization in the conduction electrons caused by the magnetic ions in the ferromagnet. This leads

to an indirect coupling in the magnetic layers which is a function of the spacer electron properties and the magnetic properties of the SFM.

The IEC strength between the constituent antiferromagnet layers is typically calculated by determining the external applied magnetic field (saturation field, H_S) at which the exchange coupling is surmounted, and the ferromagnetic layers become parallelly aligned. At this point in a hysteresis curve measurement, the maximum value of the thin film magnetization is observed. The simple model describing IEC assumes a fixed magnetic moment for each ferromagnetic layer, and the antiferromagnetic coupling energy between layers is written as $JM_1 \cdot M_2$ where J (**erg/cm²**) is the coupling constant per surface area unit and M is the magnetization vector for each corresponding ferromagnet layer. Assuming the anisotropy contributes little to H_S and a linear variation of the magnetization with applied field, the magnitude of the exchange coupling constant, J, can be expressed as a function of H_S using Eq 2.2 [32], [34]. Here J is the magnitude of the IEC (erg/cm²), H_S is the saturation field (Oe), M is the saturation magnetization (emu/cc), t_F is the ferromagnetic layer thickness (cm), and α is a constant. The α constant, not to be confused with the damping constant mentioned previously, varies from 1 in a simple trilayer structure to 2 for a superlattice where the number of magnetic layers become very large. Figure 2.3 shows the oscillation in H_S as a function of spacer layer thickness for various elements intercalated between Co ferromagnetic layers.

$$J = \frac{H_S M t_F}{2\alpha}$$

(2.2)
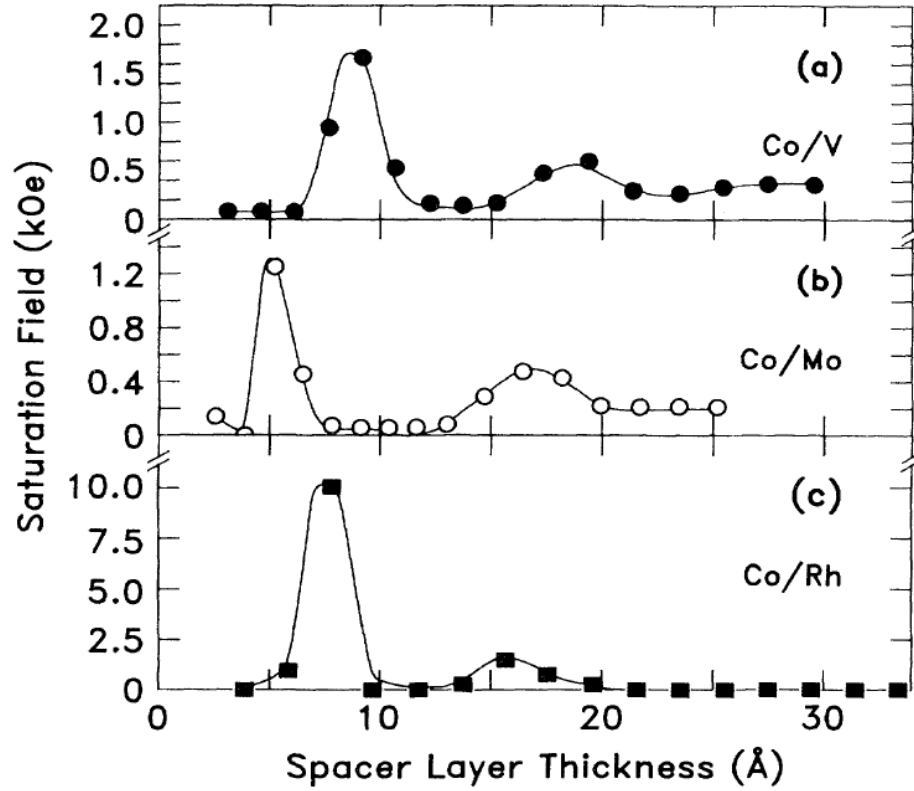
Figure 2.3 Dependence of saturation field on spacer-layer thickness for families of Co/V, Co/Mo, and Co/Rh multilayers. The saturation field is here defined as the external magnetic field necessary to achieve 80% of the saturation moment of the sample averaged over the four quadrants of the hysteresis loop. Figure from [32]. Reprinted with permission, copyright American Physical Society.

Figure 2.4 shows the exchange energy strength as a function of the number of d and sp electrons in the spacer layer for Fe/TM and Co/TM multilayers. Except for the case of Fe/Cr multilayers, it was found that the IEC strength increases systematically for the $5d$, $4d$, and $3d$ metal spacer elements and increases exponentially along each period. The highest exchange strength energies for Co-based multilayers are achieved for Ru and Rh spacer layers. It is noted that the trend of exchange coupling strength and oscillation period is not dependent on the crystal structures of the transition metals [32].
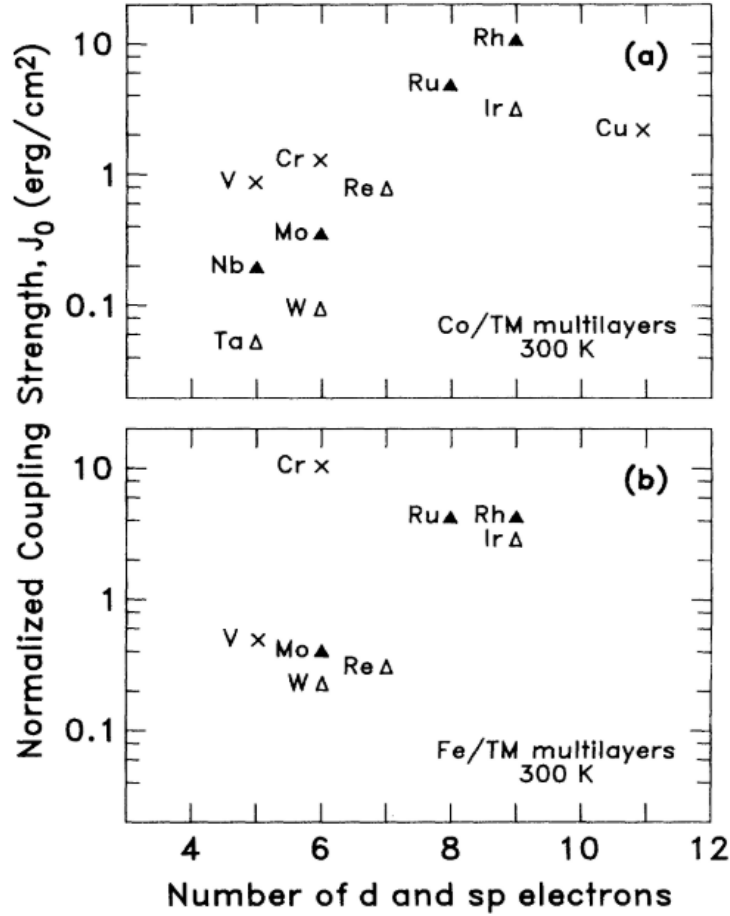
Figure 2.4 Dependence of the normalized exchange coupling constant of *3d*, *4d*, and *5d* transition metals in (a) Co/TM and (b) Fe/TM multilayers. Here TM refers to transition metal. Figure from [32]. Reprinted with permission, copyright American Physical Society.

For this work we focus on synthetic ferrimagnet (SFM) trilayers with Ru spacers intercalated between $Co_{70}Cr_{18}Pt_{12}$ electrodes. Ru is used as the spacer layer to tune and maximize the IEC strength as modeling work from our group indicates that large values of IEC are needed to obtain the highest magnetic switching speeds of these types of structures when incorporated in MTJ devices [35]. The added benefit of using Ru as the spacer layer in the SFM structure is that as discussed below, the same material can also be used to seed the necessary growth orientation in CoCrPt to exhibit perpendicular magnetic anisotropy, thereby reducing the complexity of the overall stack structure. CoCrPt is a ternary alloy that has a legacy in recording media with ultrahigh storage (1 Teradot/in^2) densities [36]. These alloys are known for their high magnetic perpendicular anisotropy, coercivity, and magnetization which can be finely tuned by adjusting

the composition of Cr and Pt, with the composition $CoCo_{13-18}Pt_{12-22}$ yielding the highest perpendicular coercivities [37]. Figure 2.5 illustrates how the compositional changes affect the magnetic anisotropy, $\textbf{\textit{K}}_\textbf{\textit{u}}$.
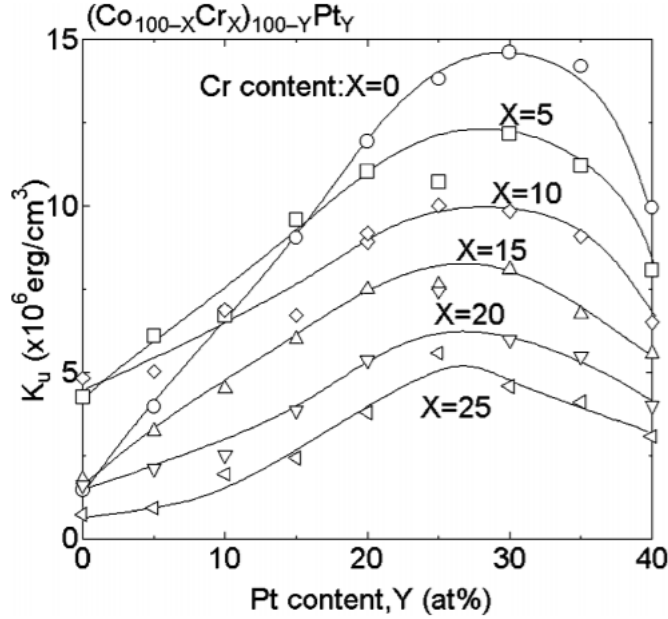
Figure 2.5 Pt content dependence of $\textbf{\textit{K}}_\textbf{\textit{u}}$ for $(Co_{100-X}CrX)_{100-Y}Pt_Y$ films. Figure from [38]. Reprinted with permission, copyright 2004 IEEE.

Figure 2.6 illustrates the hcp-Co unit cell identifying the c-axis direction and basal plane as well as the $(10\bar{1}0)$ plane. For PMA growth of CoCrPt the c-axis texture should point along the normal direction of the film plane. Figure 2.6 also depicts the heteroepitaxial relationship between hcp Co (0002) and Ru (0002) crystallographic planes. c-axis growth and thus PMA can be induced in CoCrPt due to the lattice matching between these two materials [39]. In this chapter the focus will be on seeding PMA growth in CoCrPt with Ru. The Ru growth with its (0002) basal plane parallel to the substrate plane is achieved by depositing it on Ta seed layers. For ideal c-axis texture in CoCrPt in the direction perpendicular to the film plane, the seed layer thickness and lattice parameter must be considered in addition to the surface energies of both layers.
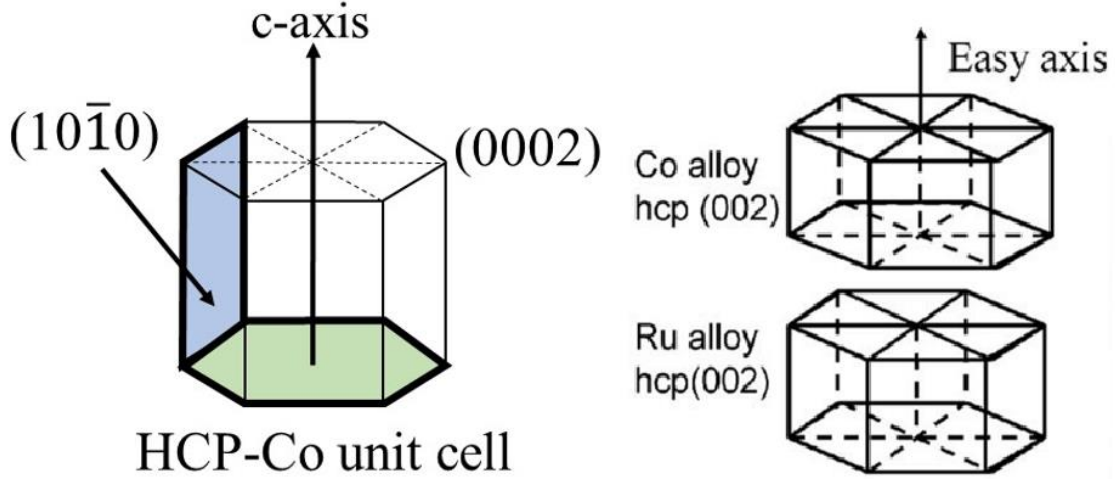
Figure 2.6 Left: Unit cell of hcp-Co with the crystallographic planes (0002) and (10$\bar{1}$0) identified. Right: Heteroepitaxial growth of hcp Co (002) on hcp Ru (002) seed layer with c-axis pointing out of plane, defining the easy axis of magnetization. Figure from [39]. Reprinted with permission, copyright AIP Publishing.

Numerical simulations based on coupled Landau-Liftshitz-Gilbert (LLG) equations by Camsari *et al*. [35] studied the interdependency between switching current, switching delay, exchange coupling strength and the degree of magnetic compensation in SFM structures. The results for SFM structures are compared to single ferromagnetic layers; all structures considered had the same thermal stability. As the dimensions of magnetic memory bits continue to decrease (reduction in magnetic volume, *V*), to maintain thermal stability as indicated in Eq. 2.3, which gives the time between spontaneous magnetization switching (τ), the magnetic anisotropy (K_U) needs to increment. Equation 2.3 is the Néel-Arrhenius law which shows that τ exponentially as the $K_U V$ is increased, with τ_0 as a characteristic length of time specific to the material. However, if K_U is increased to prevent thermal instability, this in turn increments the field or spin current necessary to reverse the magnetization as $K_U \sim H_c M_S/2$. Camsari *et al*. reported that for SFM structures, the switching delays for a given current density above the threshold are much shorter than for FM layers (Fig. 2.7). In this figure the inverse delay is plotted as a function of the injected spin-current which is normalized to the switching current threshold (I_{sc}) of a single $\Delta = 60\ kT$ ferromagnet. Here Δ refers to the thermal stability constant and refers to ratio of the stability of the magnet over the present thermal energy ($K_U V/kT$). K_U represents the anisotropy energy of the magnet, *V* is the volume, k_B is the Boltzmann constant, and *T* is temperature. A typical requirement

for magnetic recording is that at room temperature, $\Delta \geq 60$ which means the magnet is stable for at least 10 years according to the Néel-Arrhenius law. Figure 2.7 shows a family of plots for SFMs (labelled as Sy-AFM) with different volume ratios of the constituent FM layers. The largest inverse delay times (or fastest switching times) can be seen for SFMs that are nearly compensated (lower V_1/V_2 ratio) and for SFMs with high exchange coupling. In this work it was reported that delays down to 12.8 ps can be obtained using SFMs when the exchange coupling energy is high (-40 erg/cm^2) and the ratio between the two ferromagnetic layer thicknesses is low ($V_1/V_2 = 1.3$).

$$\tau = \tau_0 e^{\frac{K_U V}{k_B T}} \qquad\qquad (\,2.3\,)$$

The results of this work can be intuitively understood from a simple angular momentum conservation argument, where the current-delay product is constrained by the net number of spins ($N = M_S V / \mu_B$) needed to be reversed in the total magnetic volume (M_S is the saturation magnetization, V is volume, and μ_B is the Bohr magneton). The net number of spins that are contained within a single ferromagnet are equal to N. In an antiferromagnetically exchange-coupled system, the net number of spins that need to be switched is equal to N_1-N_2 where N_i corresponds to each magnetic layer M_i. Correspondingly, the inverse delay is proportional to this difference of spins which, can be tailored by controlling the thickness of each magnetic layer comprising the SFM structure. It should also be noted that another important result of this work is that the switching delays expected to occur in the overdrive current regime (where the injected spin current is much higher than the threshold current required to switch a single ferromagnet) do not depend on the damping constant (α) of the magnetic layers, which is typically a materials challenge that necessitates the careful selection of ferromagnetic material. An implementable MTJ device was proposed in Camsari *et al*. and is shown in Fig. 2.8, featuring an SFM free layer and two tunnel barriers as well as two reference layers. In this device the charge current flowing through the second polarizing or reference layer is re-polarized which induces an extra torque on the free layer. An important feature of this MTJ device is that a single FM material can be utilized throughout the entire film structure.
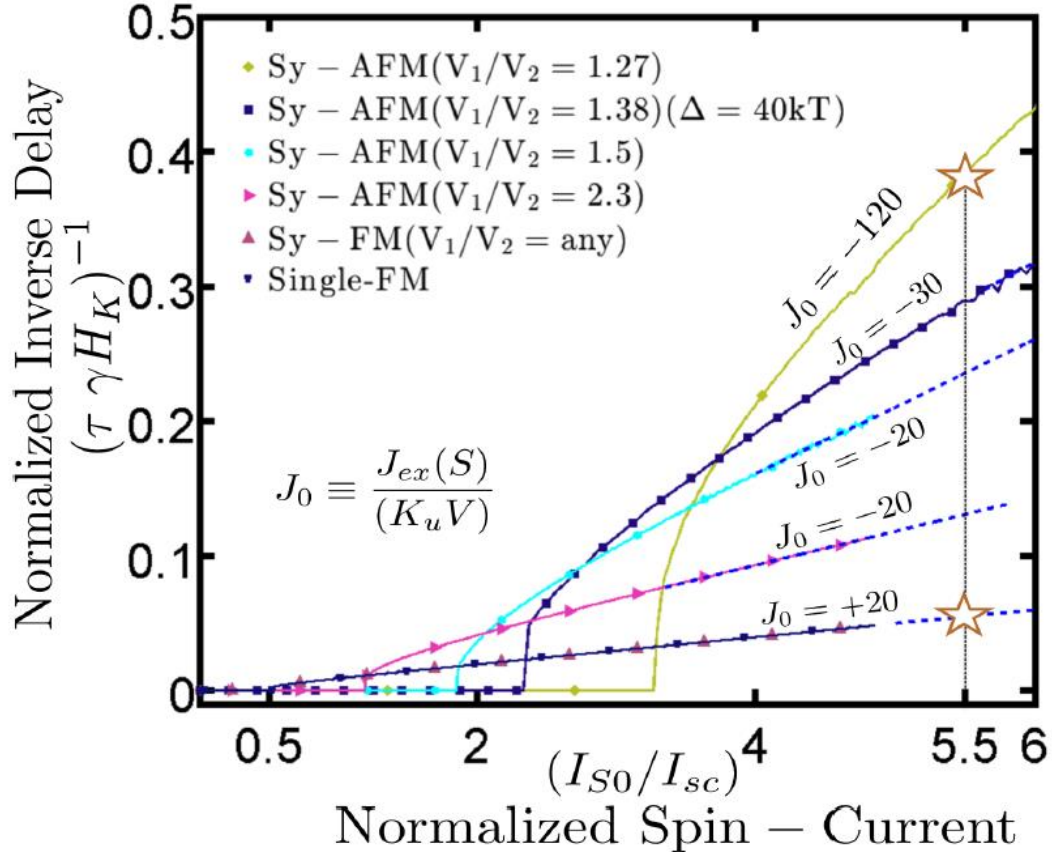
Figure 2.7 Numerical simulations based on the coupled LLG equations are shown. Normalized inverse delay is plotted as a function of normalized spin current. Normalized spin-current I_{S0} is applied to each layer separately and for the x-axis is normalized to the threshold switching current required to switch a single ferromagnet, I_{sc}. The slopes (dashed lines) in high overdrive are exactly given by: $s = \frac{(\tau H K \gamma)^{-1}}{\frac{I_{S0}}{I_{sc}}} = \alpha \left(N_1 + \frac{N_2}{N_{net}} \right)$ where $N_i = (M_S Vol.)/\mu_B$ and $N_{net} =$ $(N_1 - N_2)$ for the Sy-AFM and $N_{net} = N_1 + N_2$ for the Sy-FM and $N_{net} = N$ for the single FM. A normalized exchange interaction is defined, $J_0 = J_{ex}(S)/K_u V$ where $K_u V = 60$ kT. Parameters: $H_K^{eff} = 5000 \, Oe$, the PMA diameter Φ=36 nm, $M_S = 1000$ emu/cc and a damping coefficient α=0.01. I_{sc} is the switching threshold of the single FM, and ≈ 15.4 µA. $J_0 = \pm 20$ corresponds to the $J_{EX} = \pm 5 \, erg/cm^2$. For a Δ= 40 kT magnet with identical magnetic properties (achieved by $M_S = 1000 \rightarrow 650$ emu/cc) normalized exchange becomes $J_0 = -30 \, erg/cm^2$, which is below the experimentally measured coupling strength in Co/Rh/Co structures. Shorter delays are attainable when approaching $\frac{V_1}{V_2} = 1$, however a stronger exchange coupling is required.

Conversely, for moderate J_{EX} coupling less than 5 erg/cm^2 switching slows down following the trend shown. Dashed lines crossing the x-axis are the switching thresholds." Figure from [35]. Reprinted with permission, copyright 2016 IEEE.
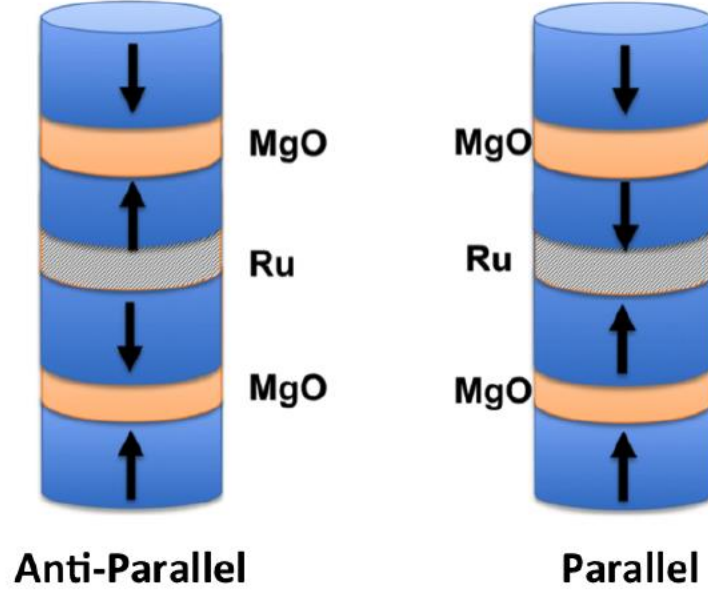
Figure 2.8 An MTJ-based magnetic architecture of the symmetrically current driven SFM structure. Double fixed layers with anti-parallel magnetizations provide independent spin currents to layer 1 and 2 for corresponding injected charge currents. Assuming that the Ru interlayer separates the spin-conductance between the top and bottom, the full structure becomes a series combination of the two Parallel or Anti-Parallel MTJs. Figure from [35]. Reprinted with permission, copyright 2016 IEEE.

This chapter describes the growth of hcp- CoCrPt with strong PMA, the basic building block for the ultrafast switching SFM-MTJ device described. A particular challenge faced in this work is the growth of the hcp-CoCrPt alloys with strong PMA on thin Ru and on MgO tunnel barrier. Carefully controlled c-axis texture perpendicular to the thin film plane and the maximization of exchange coupling strength between the FM layers of the SFM are required for the realization of the ultrafast devices proposed by Camsari *et al*. [35], which is the central motivation for the work described in this and the subsequent chapter.

2.2   Materials and Methods

All films were deposited without substrate heating or bias in a 4-target magnetron sputter system with a base pressure $< 10^{-7}$ Torr in pure Ar atmospheres. Typical growth conditions including sputter pressure, power, and deposition rate are summarized in Table 2.1. The films were grown on silicon (100) substrates with 300nm silicon oxide overlayers. Prior to deposition the substrates were sonicated for 5 min in toluene, acetone, and isopropyl alcohol sequentially and

then dried with N_2 gas before being inserted into the sputter chamber. The single ferromagnet structures fabricated consist of the following thin film layers: Ta(5nm)/Ru(10nm)/CoCrPt(x nm)/Ru(5nm). The SFM film structure comprises the following: Ta(5nm)/Ru(10nm)/CoCrPt(x)/Ru(y)/CoCrPt(z)/Ru(5nm), where x, y and z are also in nm. In both cases the function of the top Ru(5nm) layer is to protect the thin films from oxidation reactions with ambient air. The CoCrPt sputtering target has a nominal composition of $Co_{70}Cr_{18}Pt_{12}$. The Ta/Ru seed layer was used to promote CoCrPt growth with its basal (0002) plane parallel to the thin film plane (c-axis out of plane). Magnetic hysteresis loops were collected using a Quantum Design MPMS-3 superconducting quantum interference device (SQUID) magnetometer with 10^{-8} emu (magnetic moment) sensitivity in the vibrating sample magnetometry (VSM) mode.

X-ray diffraction (XRD) data was collected using a Panalytical X'Pert PRO Materials Research Diffractometer, using a Cu anode (K_α = 1.54056 Å), a PW308860/60 parabolic mirror with 1/32° slit for the incident beam optics, and a PW3098/27 Parallel Plate Collimator for diffracted beam optics. Lattice parameters and crystalline structure of the films are determined from ω-2θ peaks in the curves using the Bragg-Brentano geometry. The texture of the films is determined for a specific Bragg peak by centering the detector on the Bragg reflection and scanning ω with the detector fixed at 2θ, which will be referred to as the rocking curve.

Current-in-plane tunneling (CIPT) measurement were performed at Spintec, Grenoble, France using a CAPRES CIPT measurement system.

Table 2.1 Sputter deposition parameters employed. All films were DC sputtered except for MgO, which was RF sputtered.

Target	Power (W)	Ar_2 Pressure (mTorr)	Deposition rate (nm/min)
$Co_{70}Cr_{18}Pt_{12}$	10	3	1.40
MgO	50	1.8	0.49
Ru	5	1.8	0.53
Ta	5	1.8	0.67

2.3   Growth and Magnetic Properties of CoCrPt with Ta/Ru Seed Layers

Figure 2.9 demonstrates the effect of the Ta/Ru seed layer on the magnetic properties of CoCrPt. Direct growth of CoCrPt on oxidized silicon results in thin films with their magnetization oriented parallel to the thin film plane, most likely due to the growth of the thin film with its $(10\bar{1}0)$ plane parallel to the substrate plane. This is evidenced by the ratio of IP to OP magnetic remanence in the hysteresis curve. The ratio of IP to OP is inverted when CoCrPt is grown on Ta(5nm)/Ru(10nm) layers as shown in Fig. 2.9. The Ta layer is amorphous (as discussed later by Fig. 4.4), which promotes the preferential growth of Ru and the subsequent growth of the CoCrPt alloy with their (0002) basal planes parallel to the substrate plane. This results in the c-axis and the magnetic orientation perpendicular to the substrate plane.
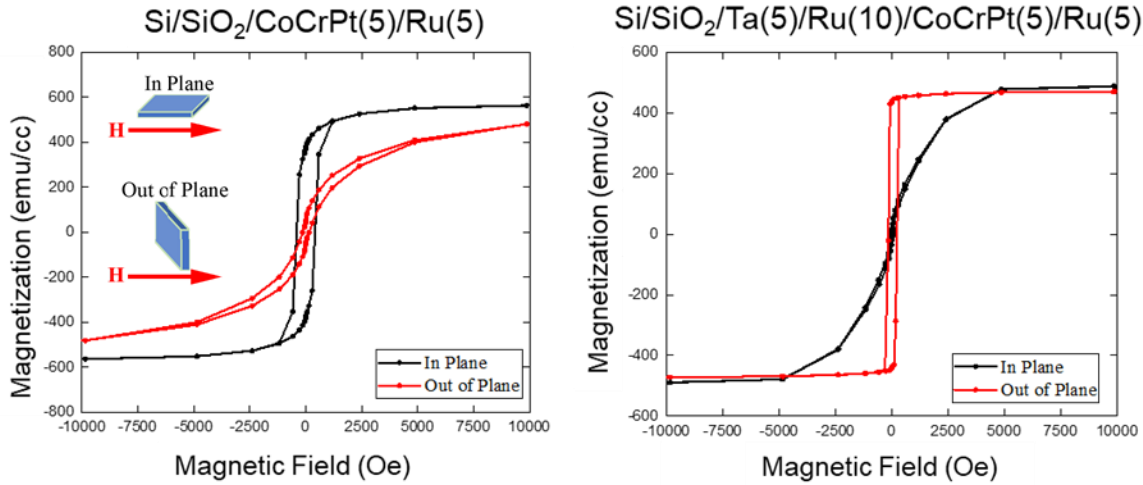
Figure 2.9 Left: Hysteresis curves of CoCrPt (5nm) directly grown on oxidized silicon (100) in the IP (easy axis) and OP (hard axis) directions. Right: Hysteresis curves of CoCrPt grown on Ta(5nm)/Ru(10nm) seed layer in the IP (hard axis) and OP (easy axis) directions.

Figure 2.10   shows magnetic hysteresis loops for a thin film series of Si/SiO$_2$/Ta(5nm)/Ru(10nm)/CoCrPt(x)/Ru(5nm) with varying CoCrPt thicknesses (x = 5, 10, 15, and 25nm). Each of these structures exhibits PMA, with the IP remanence increasing as the CoCrPt film thickness is increased. This increased IP component of magnetization is most likely due to the CoCrPt $(10\bar{1}0)$ phase being present as the film gets thicker and is less constrained to the underlying Ru (0002) film, which is discussed in a later section. All films show similar saturation magnetization values of ~500 emu/cc.

45
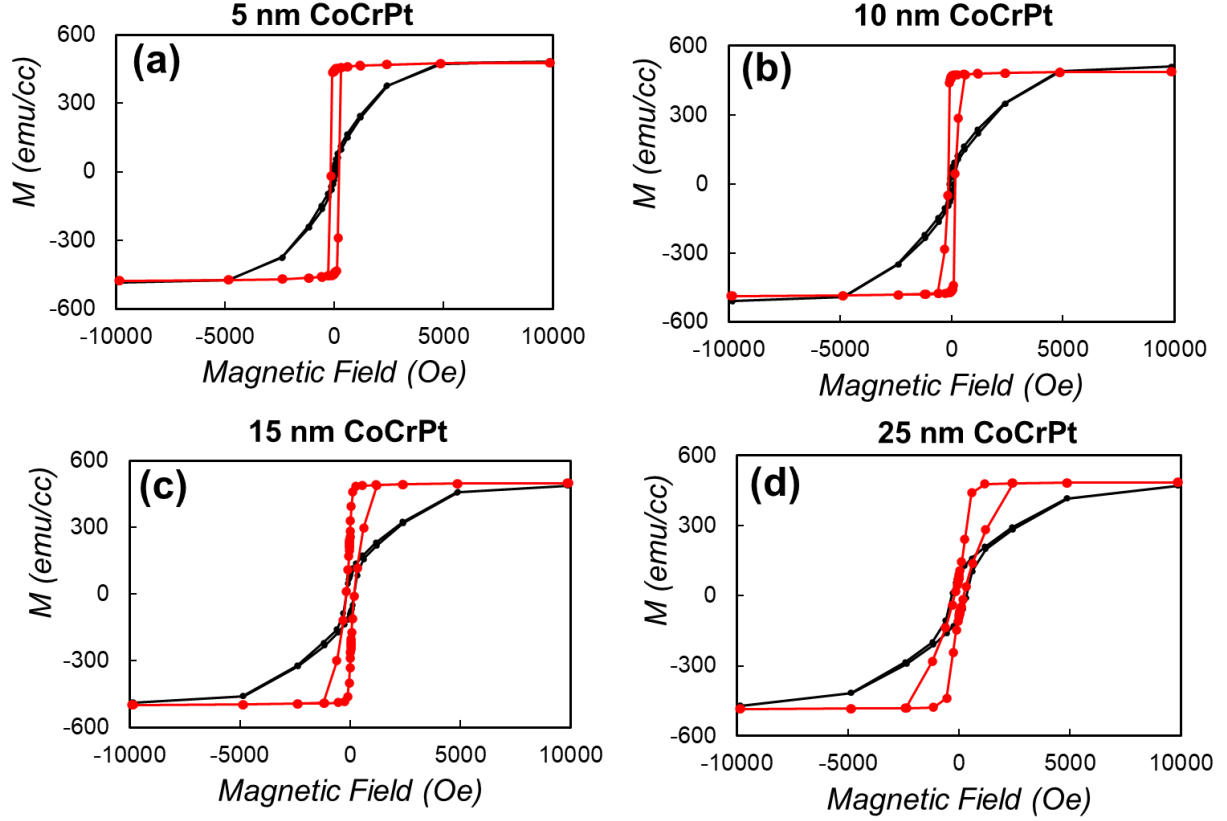
Figure 2.10 Hysteresis curves in the IP and OP directions for Si/SiO$_2$/Ta(5nm)/Ru (10nm)/CoCrPt(x)/Ru(5nm) where x is (a) 5nm, (b) 10nm, (c) 15nm, and (d) 25nm.

The effective anisotropy of the CoCrPt system is expressed by Eq. 2.1. The interfacial energy is the only term that is dependent on the ferromagnetic layer thickness. If t_{CoCrPt} is multiplied across Eq. 2.1, it can be re-written as $Kt = (K_b - M_S^2/2\mu_0)t + K_i$. A plot of $K \cdot t$ vs t yields a linear relationship whose slope represents the term $K_b - M_S^2/2\mu_0$ and the intercept with the y-axis corresponds to the value of the interfacial anisotropy constant. If the magnetocrystalline anisotropy term is negligible, the slope of the line should be negative, as is seen for CoFeB which exhibits PMA mostly due to interfacial anisotropy [1]. Figure 2.11 shows the anisotropy constant and thickness product, $K \cdot t$, as a function of CoCrPt thickness derived from the hysteresis curves shown in Fig. 2.10 K is estimated by $K = \frac{H_K M_S}{2}$, where H_K is the measured saturation field in the hard axis (IP) direction. The slope of the curve in Fig. 2.11 is positive indicating the bulk anisotropy energy is larger than the demagnetization energy. The demagnetization energy is

46

calculated as $M_S^2/2\mu_0 = 1.45 \times 10^6$ erg/cc, which is then added to the measured slope in Fig. 2.11 to yield a value of $K_b = 2.99 \times 10^6$ erg/cc. The interfacial anisotropy term, which is a weak effect in these films, is determined to be $K_i = -0.45$ erg/cm^2 from the y-intercept of Fig. 2.11. The negative value of K_i indicates the preference for in-plane anisotropy, since this term reduces the total anisotropy, K. However, bulk anisotropy dominates the total anisotropy equation for most thicknesses above 1 nm, as evident from the positive total anisotropy values observed in Fig. 2.11.
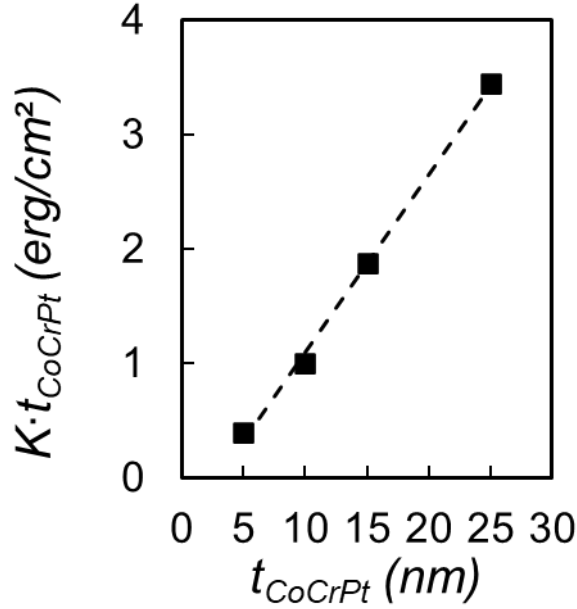
Figure 2.11 $K \cdot t$ product versus t for Si/SiO$_2$/Ta(5nm)/Ru(10nm)/CoCrPt(t)/Ru(5nm) for t = 5, 10, 15, and 25 nm for samples shown in Fig. 2.10 .

Figure 2.12a shows the θ-2θ XRD scan of the 25nm CoCrPt sample discussed in Fig 2.10 d. The reflections from the Ru(0002) and CoCrPt(0002) at 42.18° and 43.76°, respectively are shown. Powder diffraction file (PDF) values for these two reflections are reported to occur at 42.33° and 44.13° for Ru(0002) and CoCrPt(0002), respectively [40]. The rocking curve measurement corresponding to the CoCrPt(0002) Bragg reflection is plotted in Fig. 2.12b. It is confirmed from the rocking curve full width at half maximum (FWHM) measurement that the growth of CoCrPt on Ta/Ru seed layers induces the highly textured c-axis growth of CoCrPt pointing perpendicular to the film plane. The CoCrPt(0002) rocking curve FWHM is measured to be 4.13°, similar to literature values of CoCrPt (0002) grown on Ta/Ru [41].
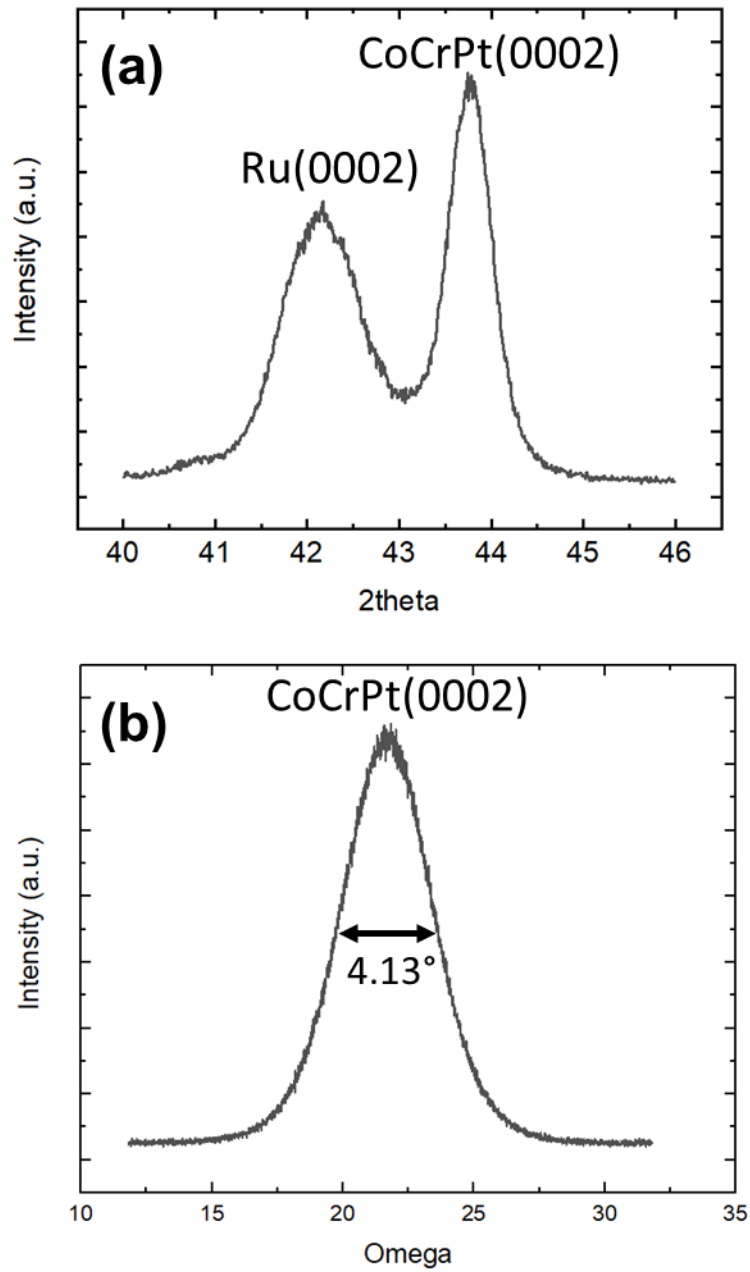
Figure 2.12 (a) θ-2θ XRD scan for Si/SiO$_2$/Ta(5nm)/Ru(10nm)/CoCrPt(25nm)/Ru(5nm) (b) The rocking curve measurement for the CoCrPt (0002) reflection shown in (a).

2.4   Growth of CoCrPt Synthetic Ferrimagnet Films for Magnetic Tunnel Junction Devices

As mentioned in the introduction, the IEC strength of SFM trilayer films are highly sensitive to the spacer thickness. This chapter focuses on the growth and magnetic characterization of thin films stack structures: $Si/SiO_2/Ta(5nm)/Ru(10nm)/ CoCrPt(x)/Ru(y)/CoCrPt(z)/Ru(5nm)$, with x, y and z also in nm. Figure 2.13 shows plots of magnetic hysteresis loops of CoCrPt(1.3nm)/Ru(x)/CoCrPt(1.3nm) for various thicknesses of the Ru interlayer (x = 0.4, 0.5, 0.6, and 0.8 nm). It is evident that with decreasing Ru spacer thickness, the saturation field, H_S (required to break the AF exchange coupling) increases. Below 0.4nm layer thickness, the hysteresis loop becomes a single curve, indicating a transition to ferromagnetic coupling, which is likely due to pinholes or discontinuities in the Ru spacer layer resulting in bridging between the FM layers.

Figure 2.14 plots the magnitude of the interlayer exchange coupling energy vs. Ru spacer thickness, calculated from the hysteresis loops shown in Fig. 2.13 and using Eq. 2.2. It is expected that the IEC energy depends on the Ru layer thickness in an oscillatory fashion, with the first peak being the largest (Fig. 2.3), which is illustrated in the Fig. 2.14 using a curved line. An oscillation period of the exchange constant cannot be calculated from this plot since more data points would be needed past 0.8nm Ru spacer thickness to observe a second peak in IEC energy. However, it is evident that a peak in IEC strength is seen for small spacer thicknesses. Below 0.4nm thick Ru spacer layers, the SFM demonstrates ferromagnetic coupling due possible discontinuities in the spacer layer film. Thus, the highest IEC energies from the SFM shown in Fig. 2.14 are found for 0.4-0.5nm Ru spacer layers.

Si/SiO2/Ta(5)/Ru(10)/CoCrPt(1.3)/Ru(X)/CoCrPt(1.3)/Ru(5)
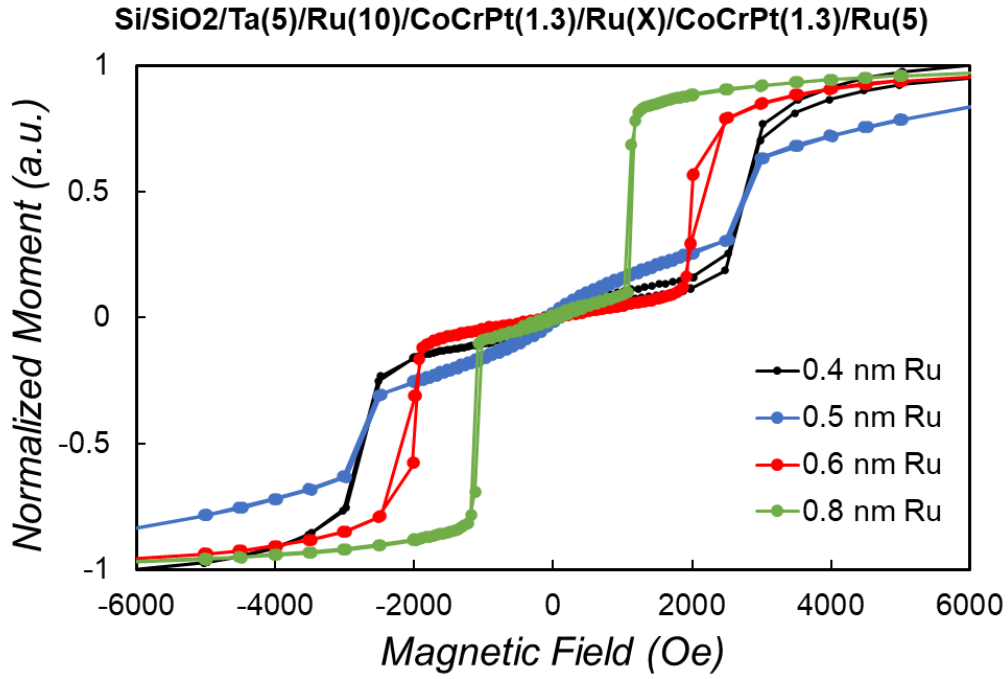
Figure 2.13 Hysteresis loops in the OP orientation for CoCrPt SFM seeded with Ta/Ru. Hysteresis loops are shown for various Ru spacer layer thickness: 0.4, 0.5, 0.6, 0.8nm.
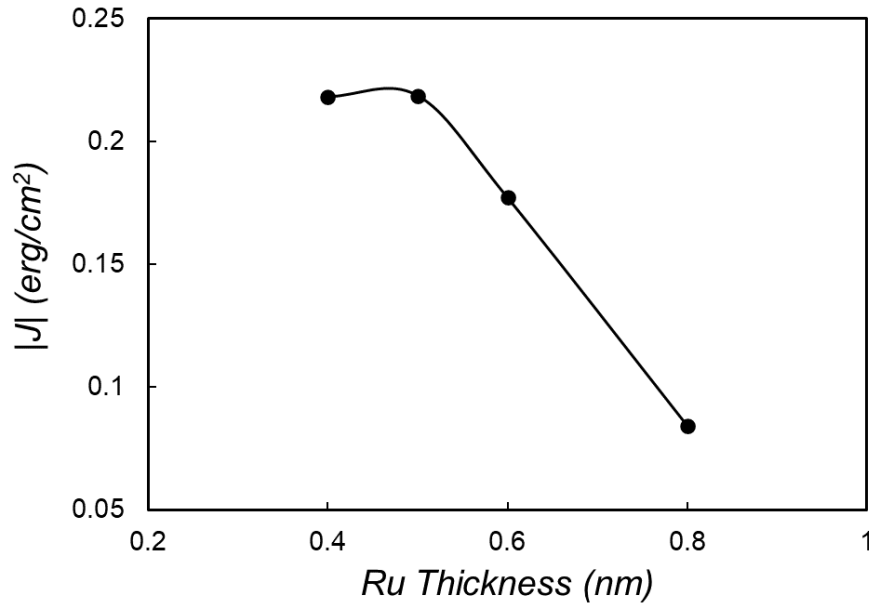
Figure 2.14 Magnitude of **J** as a function of Ru spacer layer thickness in Si/SiO$_2$/Ta(5nm)/Ru(10nm)/CoCrPt(1.3nm)/Ru(x)/CoCrPt(1.3nm)/Ru(5nm) SFM structures.

As indicated in the results of Fig. 2.7, the SFM switching speed strongly depends on the magnitude of the exchange coupling energy and the highest switching speeds are predicted for the highest values such as those measured in SFM employing Rh interfacial layers [35]. Also evident from [35] is that the speed of operation of the SFM structure is increased when the SFM is closer to compensation (i.e. the two magnetic layers are closer in thickness, providing less net moment). The ratio of volumes of the two magnetic layers studied that show a maximum inverse delay in Camsari *et al*. is 1.27. This motivated the selection of the thicknesses of the CoCrPt fabricated in this work to be 1.3nm and 1.7nm. To implement the SFM as a free layer into an MTJ, it is required that said SFM be grown on ultrathin MgO tunnel barrier layers that separate the SFM free layer and a synthetic antiferromagnet reference layer as shown in Fig 2.8. The reference layer should be a strongly coupled compensated synthetic antiferromagnet (spacer thickness 0.4nm Ru to provide strong IEC), and it will provide the generation of spin polarized charges as current is flown which will tunnel across the tunnel barrier to influence the free layer. The free layer would also be an exchange coupled SFM which will be designed with weaker IEC and thinner magnets such that it will be more immune to switching than the reference layer. Here we choose the spacer layer as Ru = 0.8nm to separate the saturation fields of each SFM to identify their magnetic transitions from hysteresis loop measurements.

The growth of out-of-plane c-axis oriented hcp-CoCrPt on MgO tunnel barriers is challenged by the fact that MgO has cubic crystalline structure and its lattice parameters are different from that of the (0002) plane of CoCrPt, as has been discussed in the literature when CoCrPt is incorporated into MgO-based MTJs [42]. In [42], to solve this problem, CoCrPt layers are antiferromagnetically coupled to CoFe which is adjacent to the MgO tunnel barrier. An ideal free layer SFM grown on MgO should exhibit a magnetic hysteresis loop similar to those shown in Fig. 2.15 and corresponding to the growth of the SFM free layer on a 5nm Ru spacer. In Fig. 2.15 three hysteresis loops are shown. The "full stack" (gold trace) represents the hysteresis curve of the full structure depicted in Fig. 2.15. The other two curves represent the "reference" compensated synthetic antiferromagnet (gray trace) and the "free" uncompensated SFM (blue trace). The thin film stack for the reference layer SFM is $Si/SiO_2/Ta(5)/Ru(10)/CoCrPt(2)/Ru(0.4)/CoCrPt(2)/Ru(5)$, whereas that corresponding to the free layer SFM is $Si/SiO_2/Ta(5)/Ru(10)/CoCrPt(1.7)/Ru(0.8)/CoCrPt(1.3)/Ru(5)$, respectively (all thicknesses are given in nm). This illustrates the versatility of the MTJ thin film SFM architectures

here proposed in which a single composition FM (CoCrPt) and interlayer material (Ru) is employed to build the critical components of the SFM (reference and free layers). For this example, all layers are observed to grow with their c-axis oriented out of plane and therefore the full stack hysteresis curve is a linear combination of the free and reference hysteresis curve as is seen for Fig. 2.15. However, when the SFM free layer is grown on MgO, which is required for tunneling magnetoresistance, the quality of the SFM free layer growth is inferior to that obtained when grown on Ru spacers.
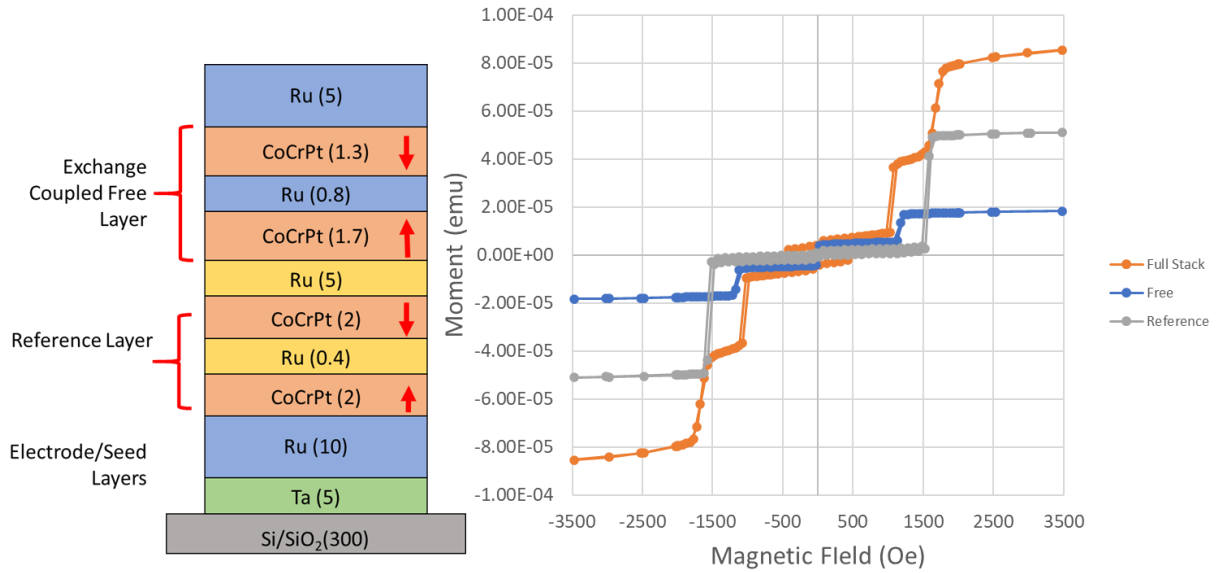
Figure 2.15 Hysteresis loop (gold trace) of a "full stack" whose structure is schematically represented on the left portion of the figure is compared to those of the "free" layer only (blue trace), Si/SiO$_2$/Ta(5nm)/Ru(10nm)/CoCrPt(1.7nm)/Ru(0.8nm)/CoCrPt(1.3nm)/Ru(5nm), and the "reference" layer (grey trace), Si/SiO$_2$/Ta(5nm)/Ru(10nm)/CoCrPt(2nm)/Ru(0.4nm)/CoCrPt(2nm)/Ru(5nm).

The magnetic hysteresis loops for full stacks wherein the SFM free layers are grown on Ru (black trace) vs. MgO (gold trace) are provided in Fig. 2.16. The MgO thickness in this example is 0.5nm. Both sets of curves show the break of the AF exchange coupling for the reference layers, CoCrPt(2nm)/Ru(0.4nm)/CoCrPt(2nm) at ~1500 Oe. However, for the case of the SFM free layer CoCrPt(1.7nm)/Ru(0.8nm)/CoCrPt(1.3nm) grown on MgO, the exchange break observed at 1100 Oe for the structure grown on Ru, is not observed. A plausible reason for this behavior is the

inferior crystalline growth of CoCrPt on thin MgO and/or the existence of pinholes in the MgO resulting in FM coupling between the reference and the free layers.
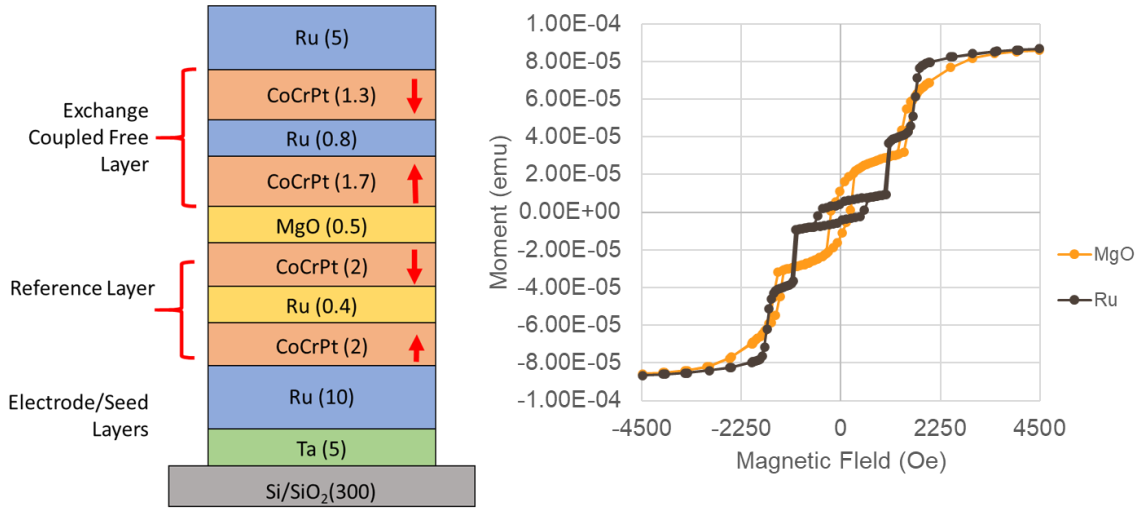
Figure 2.16 Hysteresis curves of the MgO-based MTJ which consists of the films depicted in the cross-section diagram. The Ru curve is based on the same structure but with 5nm Ru replacing the 0.5nm MgO barrier. No evidence for the AF coupling of the free layer is observed.

Thus, further work was conducted to improve the growth quality of CoCrPt on MgO by employing intermediate seed layers of (CoCrPt)Ta between MgO and CoCrPt. They were deposited by co-sputtering the CoCrPt and Ta targets to generate thin films with nominal compositions of $(Co_{70}Pt_{12}Cr_{18})_{60}Ta_{40}$. This composition was chosen due to its ability to induce growth of CoCrPt with its c-axis out of plane. As further discussed in Chapter 4, this quaternary alloy is also able to seed the desired growth orientation of CoCrPt even when very thin layers are employed. Furthermore, the CoCrPtTa alloy is weakly ferromagnetic so that it can readily FM couple with the adjacent CoCrPt layer. Figure 2.17 provides the hysteresis curves of the MTJ full structures with inserted (CoCrPt)Ta seed layers (gold trace). Here the outer transition around 1500 Oe is still visible and corresponds to the CoCrPt(2nm)/Ru(0.4nm)/CoCrPt(2nm) reference layer. The magnetic transition of the CoCrPt(1.7nm)/Ru(0.8nm)/CoCrPt(1.3nm) free layer for growth on MgO/CoCrPtTa does not show a magnetic transition that corresponds to that observed when grown on a Ru spacer. However, observation of the hysteresis loops at applied magnetic fields close to zero, seem to indicate the presence of a weakly exchange coupled SFM free layer, similar to hysteresis loops of SFM media reported in ref. [43]. The weakening of the exchange coupling

could be due to poorly textured growth of the CoCrPt. Another potential cause for this is that the MgO could be a discontinuously grown film when grown at a nominal 0.5nm thickness.
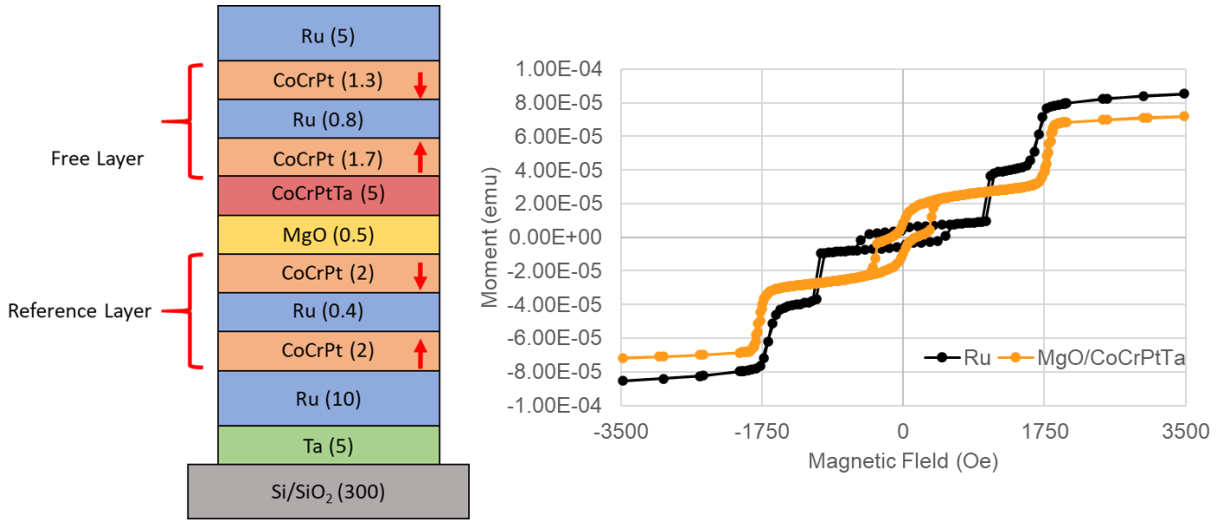
Figure 2.17 Hysteresis curves of the MgO-based MTJ which consists of the films depicted in the cross section diagram. The Ru curve is based on the same structure but with 5nm Ru replacing the 0.5nm MgO barrier and (CoCrPt)Ta for benchmarking purposes.

It is possible to measure the TMR of MTJ structures without patterning the full device with bottom and top electrodes using the current-in-plane tunneling (CIPT) technique [44]. This technique measures the resistance of the thin film stack at the surface at various probe distances. From these measurements the sheet resistance of the layers above and below the tunnel barrier, the magnetoresistance, and resistance-area product can be derived from fits to the resistance measured vs. probe spacing. To get the proper signal from this type of measurement it is necessary to have proper tunneling current beneath the MgO tunnel barrier. This can be achieved by reducing the resistance below the tunnel barrier. Thus, for the sample that was initially characterized by CIPT (shown in Fig. 2.18), the Ru seed layer has been increased to 70nm thickness. The capping layer has also been increased to 7nm thickness and the MgO layer to 1nm. These thicknesses are chosen assuming a resistance-area product of around 10 $\Omega\mu m^2$ for a ~1nm MgO thick seed layer. The hysteresis curve shown in Fig. 2.18 provides evidence that there is exchange coupling present in both the reference synthetic antiferromagnet and the free SFM layer. The initial measurements at Spintec, Grenoble, France on the sample depicted in Fig. 2.18 revealed that the resistance-area product for the MgO layer was closer to 1 $\Omega\mu m^2$, and the dependence of the resistance of the stack

versus probe thickness was flat. Potential reasons for this result was that the barrier is either too discontinuous or too conductive. The former could be due to the increased roughness from the thick 70nm Ru underlayer, causing pinholes in the MgO tunnel barrier. The latter could be due to poor growth of MgO, meaning there is not strong crystalline MgO(100) texture in the film. It should be noted that typically MgO tunnel barriers are annealed [1] to improve the crystallinity of the MgO and resulting TMR. However, the films shown in Fig. 2.18 were measured before and after annealing at 250 °C but there were no improvements in the CIPT measurement.

Future work will involve decreasing the Ru underlayer thickness and increasing the MgO tunnel barrier thickness for the stack depicted in Fig. 2.18. This will be done to both decrease the potential surface roughness of the Ru underlayer as well as increase the resistance-area product for the MgO tunnel barrier. Samples to be fabricated will include the same stack shown in Fig. 2.18 but with combinations of 15nm Ru and 40nm Ru along with 1.5nm MgO and 2.0nm MgO. The crystalline structure, continuity, and thickness of MgO will be investigated using TEM measurements. The purpose of these measurements will be to confirm that the MgO layer is both continuous and has the cubic (100) crystalline structure necessary for high TMR values.
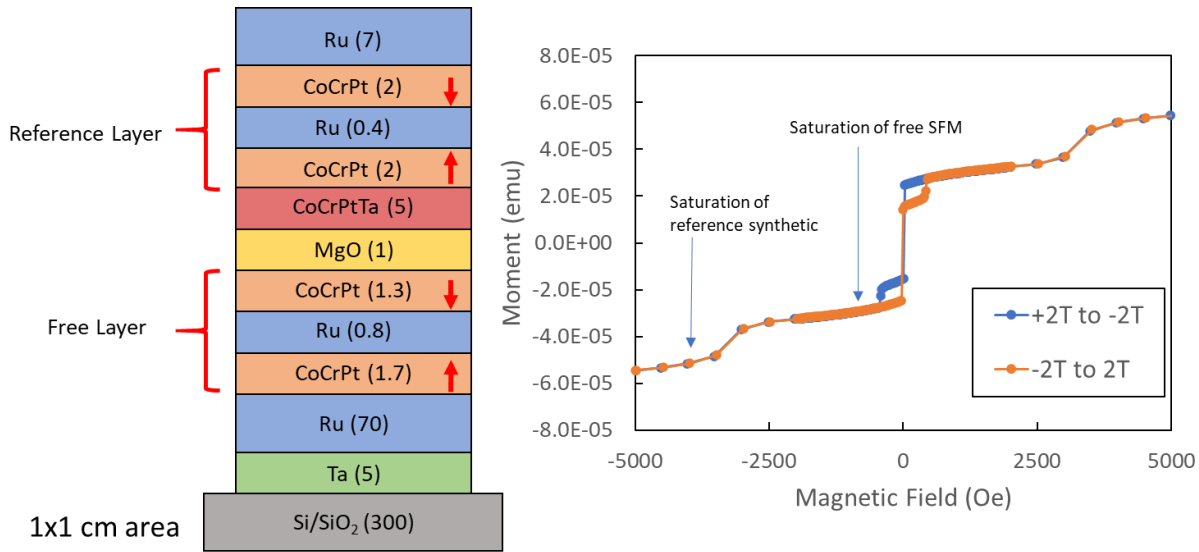
Figure 2.18 Hysteresis curves in the OP direction for the film stack depicted in the schematic drawing. The blue (orange) curve represents the data points taken as the magnetic field is decreasing (increasing). Magnetic transitions are observed and indicated by arrows that demonstrate exchange coupling is present in both the reference and free exchange coupled layers.

2.5   Conclusions

The advantages of utilizing SFM structures in MTJ devices include reduced demagnetizing fields, reduced net magnetization, lower switching currents, and faster switching speeds. CoCrPt FM layers have been grown for fabricating these structures and they exhibit PMA, high magnetic anisotropy, and modest saturation magnetization which makes them attractive for incorporating SFMs into ultrafast STT-MTJ devices. PMA in CoCrPt is achieved by promoting c-axis texture perpendicular to the substrate plane by growth on Ta/Ru underlayers. CoCrPt/Ru/CoCrPt SFMs with various Ru spacer layer thicknesses were grown that exhibited IEC strengths of up to ~0.2 erg/cm^2 for Ru = 0.4-0.5nm thick layers. Below 0.4nm Ru thickness, the SFM structure exhibited ferromagnetic coupling between the two CoCrPt magnetic layers. In an actual MTJ, to derive large TMR, the free layer SFM needs to be grown on a bcc-MgO tunnel barrier. Efforts to grow hcp-CoCrPt SFMs on 0.5nm thick MgO did not exhibit the expected magnetic behavior. Growth on MgO in combination with seed layers of quaternary, weakly magnetic CoCrPtTa alloys led to improvements but not sufficient for device implementation. This is likely due to issues related to the quality of the 0.5nm MgO layers employed (roughness, pinholes, crystalline quality) that precludes high quality growth of the hcp-CoCrPt SFM free layer thereupon. It was found that depositing the free SFM containing thinner CoCrPt FM layers on the bottom of the MTJ structure improved the magnetic properties of the films. This demonstrates the challenge of growing highly textured c-axis CoCrPt in these structures. Future work will include improving this growth by increasing the thickness of the MgO layer since it may be discontinuous and minimizing the thickness of the seed layer which may affect TMR. In the literature thicker MgO layers are employed and, subsequent to the deposition of the MTJ thin films containing MgO, annealing at temperatures in excess of 250 °C is performed to improve the crystallinity of the MgO layer [1]. Future work will also include annealing the MTJ structures to promote higher TMR values.

An unpatterned film was measured using CIPT to determine the magnetoresistance of the MTJ stack. The reference layer is a compensated SFM with zero net moment, while the free layer is an SFM with weaker exchange coupling and a net moment. Initial CIPT measurements indicate the MgO barrier is either discontinuous or does not demonstrate good crystalline growth. Future work involves decreasing the Ru underlayer thickness to decrease the surface roughness of the film as well as to increase the MgO tunnel barrier thickness. MTJ thin film stacks containing CoCrPt/Ru/CoCrPt SFMs separated by MgO layer and (CoCrPt)Ta seed layers exhibit PMA

growth and interlayer exchange coupling in the SFM layers. This paves the way to realizing MgO-based MTJs containing CoCrPt-based SFM free and fixed layers.

3. TEMPERATURE-DEPENDENT MAGNETIC TRANSITIONS OF CoCrPt/Ru/CoCrPt SYNTHETIC FERRIMAGNET TRILAYERS

3.1 Introduction

Synthetic ferrimagnet (SFM) trilayers consist of two antiferromagnetically coupled ferromagnetic (FM) films separated by a thin non-ferromagnetic metallic interlayer. For the case of identical FM layers, if the films are dissimilar in thickness, the SFM structure will exhibit a net magnetic moment (uncompensated ferrimagnet). The exchange coupling of the SFM varies with the interlayer thickness in an oscillatory fashion [31] and it has been attributed to various physical processes that include dipolar magnetostatic interactions and Ruderman-Kittel-Kasuya-Yosida (RKKY) coupling. First observed by Grünberg *et al*. [30], films exhibiting antiferromagnetic coupling were utilized shortly thereafter in magnetic sensor devices based on the giant magnetoresistance (GMR) observed in Fe/Cr antiferromagnet structures [45][46]. More recently, synthetic ferrimagnets and antiferromagnets have been utilized in magnetic tunnel junctions (MTJs) to provide exchange bias to the recording layer (free layer) or as the recording layer itself. When utilized in MTJ devices the strength of interlayer exchange coupling and the magnetic volume determines the functionality of the SFM as a reference or free layer. The coupling strength is derived from measuring the magnetic field required for overcoming the exchange coupling energy which renders the magnetization orientation of the individual layers to be parallel. SFM structures that act to replace single FM recording layers in MTJs have demonstrated low critical switching currents without dramatically affecting thermal stability [29][47]. Additionally, we have proposed that SFM free layers can exhibit ultrafast switching speeds down to the picosecond time regime [35].

Most MTJ devices utilize CoFeB as the FM electrode due to its low magnetic damping constant and its PMA resulting from interfacial anisotropy when grown on MgO. Furthermore, this material combination yields high tunneling magnetoresistance [48]. However, the maximum thickness of CoFeB layers exhibiting PMA is limited to around 1.5nm [1]. The magnetization of CoFeB is also relatively high, requiring high values of charges current needed for spin-transfer torque switching. CoCrPt is a material of interest for MTJ applications due to its low magnetization and its large anisotropy [42], resulting in lower switching currents, improved thermal stability, and the use of thicker FM layers with concomitant process control improvements. In addition, the SFM

configuration circumvents the materials-restrictive low magnetic damping requirement for selection of the FM thin film for MTJ devices [35].

It is essential to tailor the exchange energy and switching properties of the SFM structure for use in memory devices. However, the magnetic properties of the SFM are temperature dependent, and memory devices could be expected to operate under extreme conditions within the range of 200K to 370K. In this section the exchange coupling of CoCrPt-Ru-CoCrPt trilayer structures has been investigated from 2K to 300K. It has been observed by Koplak *et al*. [49] that with decreasing temperature, the hysteresis loops of SFMs vary dramatically, and these authors developed a formalism to describe the observed changes in the hysteresis loop as a function of temperature in a CoFeB-Ta-CoFeB SFM. They employ an energy balance approach that includes the Zeeman energy, the exchange coupling energy, and energy barriers for switching arising from the effective magnetic anisotropy energy. It was found that the two main parameters controlling the switching behavior with decreasing temperature is the ratio of the magnetic moments of the two constituent ferromagnetic layers as well as the energy barrier for switching of each film, which is temperature dependent. In this section the energy diagram technique introduced by Koplak *et al*. is used to describe the magnetic transitions measured in a CoCrPt-Ru-CoCrPt SFM as a function of temperature. This is compared with the results on the CoFeB-Ta-CoFeB SFM structure. Predictions are also made for the magnetic transitions of the CoCrPt-Ru-CoCrPt SFM at 200K to 370K to exemplify the practical use of the energy diagram technique for assessing the robustness of a potential sensor device employing an SFM free layer. This section includes work that has been submitted for a peer-review publication [50].

3.2   Materials and methods

All films were deposited without substrate heating or bias in a magnetron sputter system with a base pressure $< 10^{-7}$ Torr. The films were grown on oxidized silicon (100) substrates. The thin film structure consisted of the following: Ta(5nm)/Ru(10nm)/CoCrPt(x)/Ru(y)/CoCrPt(z)/Ru(5nm), where x, y and z are also in nm. The CoCrPt sputtering target has a nominal composition of $Co_{70}Cr_{18}Pt_{12}$. The Ta/Ru seed layer was used to promote CoCrPt growth with its basal (0002) plane parallel to the thin film plane (c-axis out of plane). Magnetic hysteresis loops were collected using a Quantum Design MPMS-3

superconducting quantum interference device (SQUID) magnetometer with 10^{-8} emu sensitivity in the vibrating sample magnetometry (VSM) mode.

3.3   Magnetic Transitions of a CoCrPt-Ru-CoCrPt Synthetic Ferrimagnet

As shown in Fig. 3.1, the exchange energy of the CoCrPt-Ru-CoCrPt SFM can be tailored by varying the Ru interlayer thickness. The exchange energy per unit area of an SFM with dissimilar FM layers was estimated by Koplak *et al*. using the expression: $J_{EX} = -H_B m_2/S$. Here H_B is the bias field which indicates the center of the outer loop. In Fig. 3.2a-b, H_B is labeled and measured by finding the center of the outer loops at which point the SFM becomes saturated. At 2K (Fig. 3.2c), there is no outer loop unlike in Fig. 3.2a-b. In this case a minor loop must be taken to locate the H_B field, which is shown by the red curve in Fig. 3.2c. In the equation for J_{EX} , m_2 is the magnetic moment of the thinner magnetic layer (m_1 being the moment from the thicker layer), and S is the surface area of the film. In Fig. 3.1, the exchange energy is calculated to be -0.070 erg/cm^2 and -0.0305 erg/cm^2 for SFMs with 0.5 and 0.8nm Ru interlayers, respectively. The exchange energy is highly sensitive to the Ru thickness. Generally, higher exchange coupling strength is desirable for memory applications, including novel devices such as a double MTJ containing two SFM reference layers and a SFM free layer discussed in [35] which is predicted to switch in ps time scales.
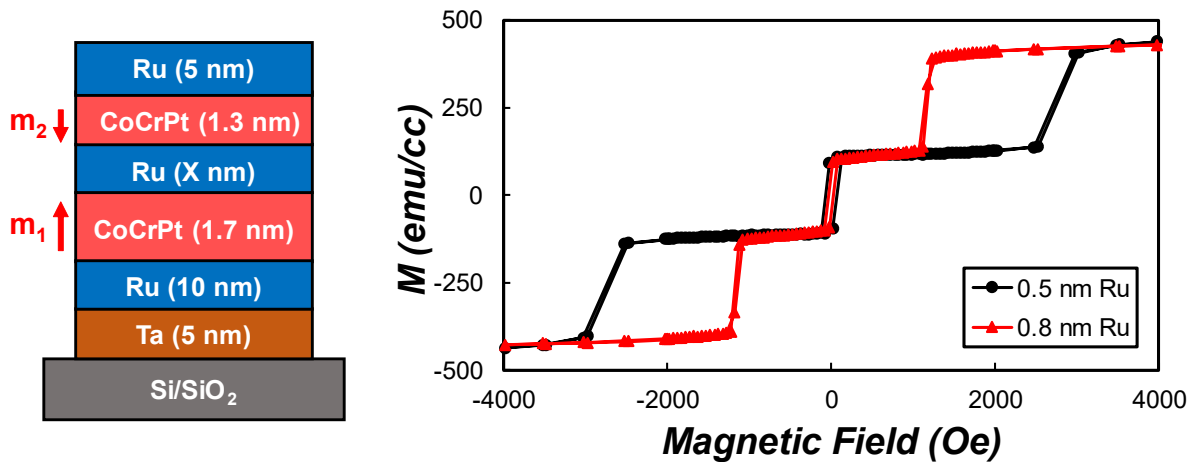
Figure 3.1 Left: Schematic representation of the film stack cross-section: red arrows indicate the direction of magnetization of the constituent FM layers at remanence. Right: Hysteresis curves of the SFM structures with two different Ru interlayer thicknesses measured at 300K.
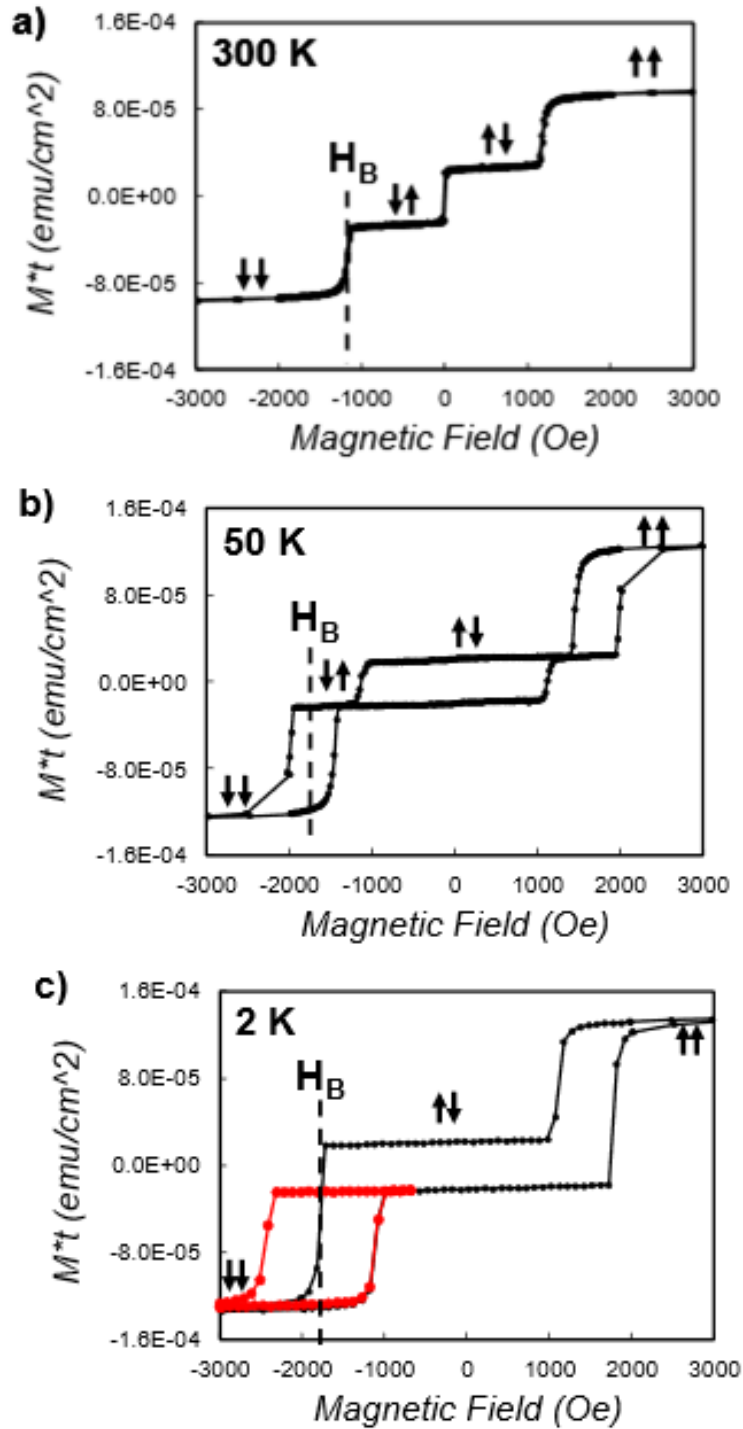
Figure 3.2 Hysteresis curves of CoCrPt(1.7nm)/Ru(0.8nm)/CoCrPt(1.3nm) SFM at a) 300K, b) 50K, and c) 2K. The switching behavior from 50K-300K includes three magnetic transitions while two transitions are observed at 2K. In a) and b), the center of the outer loops is indicated by H_B. In c), the H_B indicates the center of the minor loop (red curve) associated with the switching of the thinner magnetic layer.

A SFM has four possible magnetic configurations (↑↑, ↑↓, ↓↑, ↓↓), where the left and right arrows indicate the bottom (thicker) and top (thinner) FM layers, respectively as shown in Fig. 3.2. The number of transitions found in the hysteresis loop at a given temperature depend on the exchange-coupling energy, the Zeeman energy, and the energy barrier for magnetic reversal. From the literature, it is also evident that the magnetic field sweeping rate influences the magnetic switching behavior [51]. However, in this work each data point of the hysteresis curve is collected once the applied field has stabilized. Also, each hysteresis curve is collected once the sample temperature has fully stabilized.

Koplak *et al*. found for the CoFeB-Ta-CoFeB SFM three types of hysteresis loops over the temperature range studied. In the 180K-300K range, three magnetic transitions were observed for Type I hysteresis (↑↑-↑↓, ↑↓-↓↑, ↓↑-↓↓). Two transitions are present between 120K-170K for Type II hysteresis (↑↑-↑↓, ↑↓-↓↓) and 2K-110K (↑↑-↓↑, ↓↑-↓↓) for Type III hysteresis. These transitions are observed when the applied magnetic field is swept from positive to negative. The reverse transitions are encountered when the field is swept from negative to positive. In the case of the CoCrPt-Ru-CoCrPt system, we observe three transitions (↑↑-↑↓, ↑↓-↓↑, ↓↑-↓↓) in the 300K to 50K range (Fig. 3.2a-b). Whereas the number of magnetic transitions reduces to two when the sample is cooled down to 2K (Fig. 3.2c), (↑↑-↑↓, ↑↓-↓↓) similar to the hysteresis loop measured in the 120K-170K range in the CoFeB-Ta-CoFeB system. The third set of magnetic transitions (↑↑-↓↑, ↓↑-↓↓) that are reported for the CoFeB-Ta-CoFeB SFM (Type III hysteresis) are not observed for the CoCrPt-Ru-CoCrPt SFM. Table 3.1 summarizes the types of hysteresis curves observed in both the CoCrPt-Ru-CoCrPt and the CoFeB-Ta-CoFeB SFMs as a function of temperature.

Table 3.1 Comparison of the hysteresis types and the associated magnetic transitions observed in the CoCrPt-Ru-CoCrPt and the CoFeB-Ta-CoFeB SFM by Koplak *et al.* [49]. The indicated magnetic transitions occur when the magnetic field is swept from positive saturation to negative saturation. The bold arrows represent the magnetic moment, m_1, of the thicker magnetic layer. The temperature range where each type of hysteresis curve is observed are provided under the heading of the different SFM structures.

Hysteresis Type and Magnetic Transitions	CoCrPt-Ru-CoCrPt SFM	CoFeB-Ta-CoFeB SFM
Type I Hysteresis ↑↑-↑↓, ↑↓-↓↑, ↓↑-↓↓	50 - 300 K	180 - 300 K
Type II Hysteresis ↑↑-↑↓, ↑↓-↓↓	2 - 40 K	120 - 170 K
Type III Hysteresis ↑↑-↓↑, ↓↑-↓↓	-	2 - 110 K

Here we analyze the magnetic transitions exhibited by the SFM with a 0.8nm Ru spacer (Fig. 3.1) using the energy diagram technique. This technique relies on a simple energy balance (Eq. 3.1) which contains the exchange energy (E_{EX}), Zeeman energy (E_Z), and the potential barriers E_{eff1} and E_{eff2} (corresponding to the 1.7nm and 1.3nm CoCrPt, respectively).

$$E_{Total} = E_{EX} + E_Z + E_{eff1} + E_{eff2} \qquad (3.1)$$

The exchange energy, E_{EX}, is proportional to the surface area of the sample and can be estimated from $|E_{EX}| = H_B \cdot m_2$. Here H_B represents the bias field, which is measured by locating the center of the minor loop of the softer magnet as previously described. In the case of the first type of switching shown in Figs. 3.3a and 3.3b, there are three loops: the center field of the outer loops is H_B and indicates the strength of exchange coupling. The potential energy barriers arise due to the effective magnetic anisotropy energy of each magnetic layer. Notably the hysteresis curves are measured along the easy-axis, therefore, E_{eff1} and E_{eff2} are not equal to the anisotropy energy determined from the hard axis hysteresis. In a hysteresis loop with three transitions (Figs. 3.3a and 3.3b), E_{eff1} can be estimated from the coercive field of the outer loops as $H_{C-outer} = \frac{E_{eff1}}{2 \cdot m_1}$. Then E_{eff2} can be calculated from the coercive field of the inner loop expressed by

$H_{C-inner} = \frac{E_{eff1}+E_{eff2}}{2(m_1-m_2)}$. These estimates arise from the equations derived by Koplak *et al.* describing the possible magnetic transitions. The Zeeman energy, E_Z, is proportional to the applied magnetic field and can be expressed as $E_Z = -(m_1 + m_2) \cdot H$.

The second type of hysteresis curve shown in Fig. 3.3c has no outer loops, which are needed to estimate E_{EX}. However, one can still calculate H_B and thus E_{EX} by measuring the minor loop as shown in Fig. 3.2c. This is obtained by switching the softer, thinner m_2 magnetic layer after the SFM has been saturated [27]. H_B, labeled in Fig. 3.2c, was determined to be -1798 Oe. The minor loop in Fig. 3.2c is measured by saturating the SFM to the ↓↓ orientation, sweeping the magnetic field to just beyond the ↓↓-↓↑ magnetic transition, and then saturating the SFM back to the ↓↓ orientation. This indicates an exchange coupling strength of -0.11 erg/cm^2 for the SFM at 2K. After E_{EX} is obtained, E_{eff1} and E_{eff2} can be calculated using equations $H_{\uparrow\uparrow-\uparrow\downarrow} = \frac{2|E_{EX}|-E_{eff2}}{2m_2}$ and $H_{\uparrow\downarrow-\downarrow\downarrow} = -\frac{2|E_{EX}|+E_{eff1}}{2m_1}$, respectively. The resulting energy diagram (Fig. 3.3c) is consistent with the transition fields of the minor loop and the saturated hysteresis loop. E_{eff1} and E_{eff2} are plotted at each temperature in Fig. 3.5a. Notably, E_{eff1} is larger than E_{eff2} until the temperature is lowered to 2 K. Similar behavior was observed in Koplak *et al.*
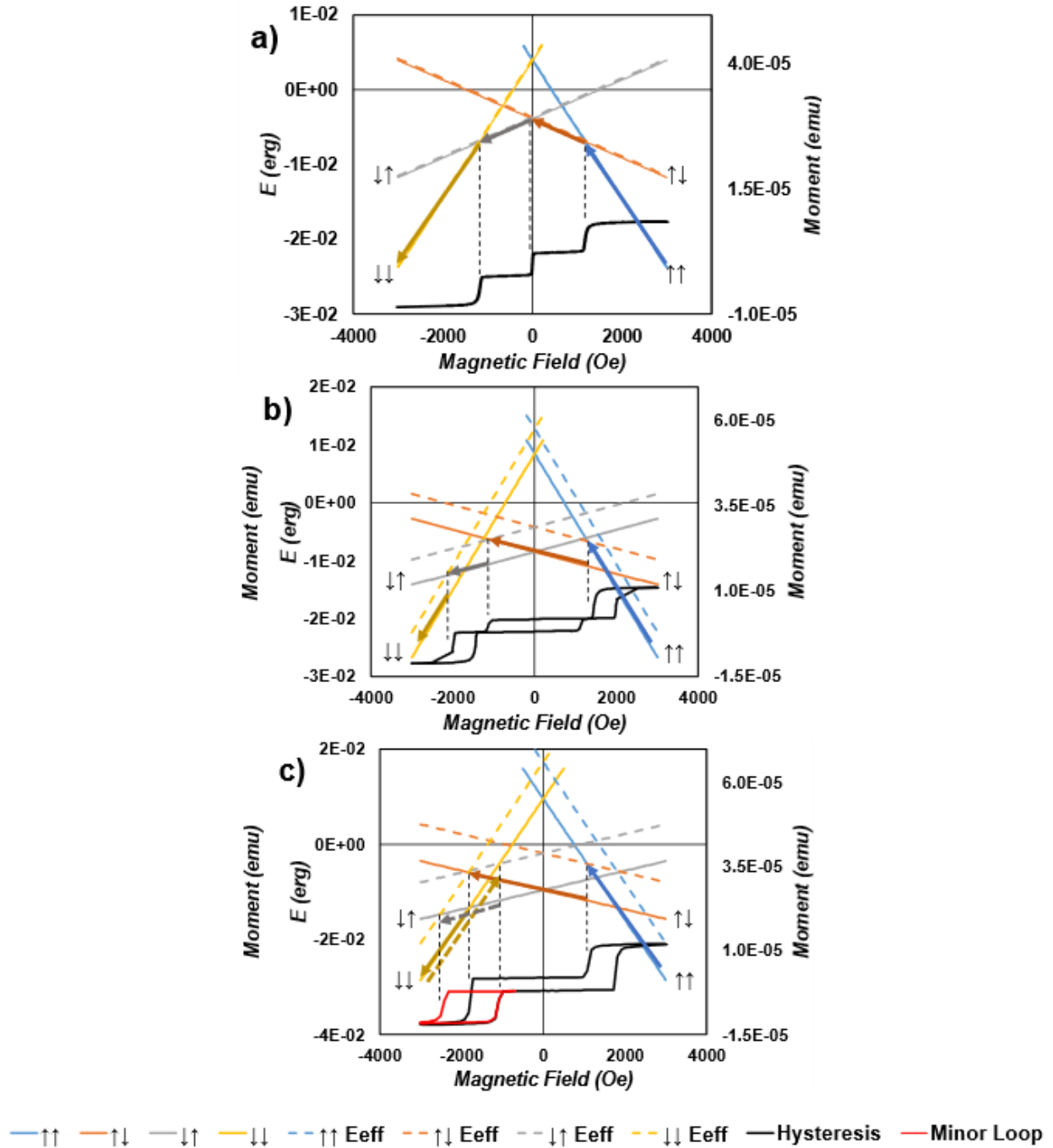
Figure 3.3 Energy diagrams of the CoCrPt(1.7nm)/Ru(0.8nm)/CoCrPt(1.3nm) SFM at a) 300K, b) 50K, and c) 2K. The solid lines indicate the total energy, excluding the energy barriers, while the dashed lines include the temperature-dependent energy barriers. The hysteresis curves are shown in each pane with corresponding magnetic moments on the secondary axis. The red hysteresis loop in c) displays the minor loop measured to determine H_B. Dashed arrows indicate the energies associated with the minor loop and the corresponding transitions.

The energy diagrams shown in Fig. 3.3 describe the magnetic transitions occurring for each temperature. Solid lines indicate the energy of the SFM system with zero E_{eff}, i.e. when there are no energy barriers to overcome. The solid lines are thus, the addition of the Zeeman energy and the Exchange energy, with a y-intercept equal to the exchange energy. The dashed lines represent the total energy of the system after the E_{eff1} and E_{eff2} are included, as described by Eq. 3.1. As the magnetic field is swept, the magnetic orientation present is the one with the lowest energy. Shown in Fig. 3.3a), the blue solid line represents the ↑↑ orientation as the field is lowered from +2 T. If the energy barrier for reversal of each layer is zero, the ↑↑-↑↓ will occur at the intersection of the blue solid line and the orange solid line representing the total energy of the ↑↓ orientation. At 300K, the E_{eff} energies for m_1 and m_2 are negligibly low such that the magnetic transitions occur approximately at the solid line intersections.

The potential barriers become larger as temperature is decreased down to 2K (Fig. 3.5a). Since the E_{eff} terms are not field-dependent, they shift the dashed lines up along the y-axis. For a magnetic transition to occur, the magnetic field must be changed such that the energy barrier between the solid and dashed line is crossed. As seen in Fig. 3.3b, the ↑↑-↑↓ transition no longer occurs at the intersection of the solid blue and orange lines, but at the point where the potential barrier of another orientation energy is crossed. As the potential barriers increase with lower temperature, certain transitions are prohibited from occurring due to the existence of lower energy states from other magnetic orientations. At 2K (Fig. 3.3c), the ↑↓-↓↑ transition does not occur as it does at 300K and 50K (Fig. 3.3a-b) since the potential barrier of the ↓↓ state is lower in energy than the ↓↑ state.

The third set of magnetic transitions (↑↑-↓↑, ↓↑-↓↓), or Type III hysteresis, occurs when the condition $E_{eff1} < E_{eff2} \cdot \frac{m_1}{m_2} - 2|E_{EX}| \cdot \frac{m_1-m_2}{m_2}$ is satisfied [49]. The CoCrPt-Ru-CoCrPt SFM studied does not meet this requirement and does not show this set of transitions even down to 2K. Compared to the CoFeB-Ta-CoFeB SFM reported by Koplak et al. [49], which has an exchange energy at 300K of E_{EX}/S = -0.01 erg/cm^2, the CoCrPt-Ru-CoCrPt SFM has an exchange energy at 300K of E_{EX}/S = -0.04 erg/cm^2. The CoFeB-Ta-CoFeB SFM and the CoCrPt-Ru-CoCrPt SFM have m_1/m_2 ratios of 1.38 and 1.79, respectively. At 300K the effective anisotropy energy barriers for both systems are: E_{eff1}/S = 4.0x10^{-3} erg/cm^2 and E_{eff2}/S = 2.5x10^{-3} erg/cm^2 for CoFeB-Ta-CoFeB, E_{eff1}/S = 1.7x10^{-3} erg/cm^2 and E_{eff2}/S = 0.73x10^{-3} erg/cm^2 for the CoCrPt-Ru-CoCrPt. The energy barriers for the CoCrPt-Ru-CoCrPt are lower for E_{eff1} and E_{eff2} by a factor of 2.3 and 3.4,

respectively. This disparity in E_{eff} causes the right side of the inequation to be lower, which explains why the third set of magnetic transitions are absent in the CoCrPt-Ru-CoCrPt SFM.

Figure 3.4 illustrates the dependence of the left and right sides of the inequality $E_{eff1} < E_{eff2} \cdot \frac{m_1}{m_2} - 2|E_{EX}| \cdot \frac{m_1 - m_2}{m_2}$ on the exchange coupling energy for both the CoCrPt and CoFeB SFM systems. The plot shows the energies calculated at 100K, since CoFeB-Ta-CoFeB shows the third set of magnetic transitions at this temperature. At a given exchange energy, the third set of magnetic transitions should be observed when the right side of the equation is larger than E_{eff1}. When plotted as a function of E_{EX}, the right side of the inequality is a line whose slope is determined by the m_1/m_2 ratio and the intercept by the product of E_{eff2} and m_1/m_2. The dependence of the right side of the inequality on m_1/m_2 is also illustrated in Fig. 3.4a-b. As m_1/m_2 approaches 1, the slope and the y-axis intercept of the right side of the inequality is lowered. Since it has been shown that fast spin transfer torque switching can be achieved with a low m_1/m_2 ratio [35], this analysis is important in understanding the type of hysteresis curves that will be present in the SFM when tailoring the ratio of magnetic moments. It is evident from Fig. 3.4a that the magnetic switching behavior of the CoCrPt-Ru-CoCrPt SFM will not exhibit the third type of magnetic switching for either stronger or weaker exchange energy as the intercept of the right side of the inequality is lower than E_{eff1}.

As mentioned earlier, the SFM can be used as a replacement for a single FM layer in a memory device. Such devices are expected to operate successfully over a wide range of temperatures. Therefore, it is important to predict the behavior of the SFM at any temperature. The energy diagram technique can be used to predict the transition fields of the SFM if the temperature dependence of E_{eff}, E_{EX}, and the magnetization, m, are known. Figure 3.5a-c shows the temperature dependence of E_{eff}, E_{EX}, and m, respectively. E_{eff}, E_{eff1}, and E_{eff2} are proportional to $m^{\frac{n(n+1)}{2}}$ at lower temperatures (<150K), while at higher temperatures the potential energy barriers are proportional to m^n similar to the temperature dependence of the magnetic anisotropy observed for other materials [14, 15]. Here, m is the magnetic moment and n is the exponent of the magnetic anisotropy function (n=2 is typical for uniaxial anisotropy). Fig. 3.5a shows the fit for E_{eff2} based on the $m^{\frac{n(n+1)}{2}}$ proportionality. Good agreement is seen with the fit until around 150K, at higher temperatures, E_{eff2} is proportional to m^n. The parameters E_{EX} and m change linearly in this temperature range. Fitting the trends seen in Fig. 3.5 allows one to predict the behavior at 200K

and 370K, the temperature extrema that a spintronic sensor could potentially expected to operate reliably. The energy diagrams for the CoCrPt(1.7nm)/Ru(0.8nm)/CoCrPt(1.3nm) SFM at these two temperatures are shown in Fig. 3.6. These energy diagrams are constructed using the fitted parameters from Fig. 3.5. Both energy diagrams in Fig. 3.6a) and 3.6b) show magnetic transitions corresponding to the type I regime [49]. The transition field for ↑↑-↑↓ (where m_1 reversal occurs) is predicted to be 1400 Oe and 950 Oe at 200 K and 370 K, respectively. In Fig. 3.6a the hysteresis diagram measured at 200K is shown and agrees with the predicted transitions from the energy diagram.

The CoCrPt-Ru-CoCrPt SFM system can provide potential advantages over CoFeB-Ta-CoFeB due to its low magnetization and its large magnetic anisotropy [42]. The anisotropy in CoCrPt is largely determined by magnetocrystalline anisotropy as opposed to interface anisotropy for the case of CoFeB. Therefore, CoPtCr films exhibit PMA for film thicknesses up to 15 nm. Thus, the m_1/m_2 ratio in the films can be controlled more precisely, allowing for more tunability of the SFM properties. This is of particular interest for the implementation of ps magnetic switching employing SFM structures as proposed by Camsari *et al*. [35].
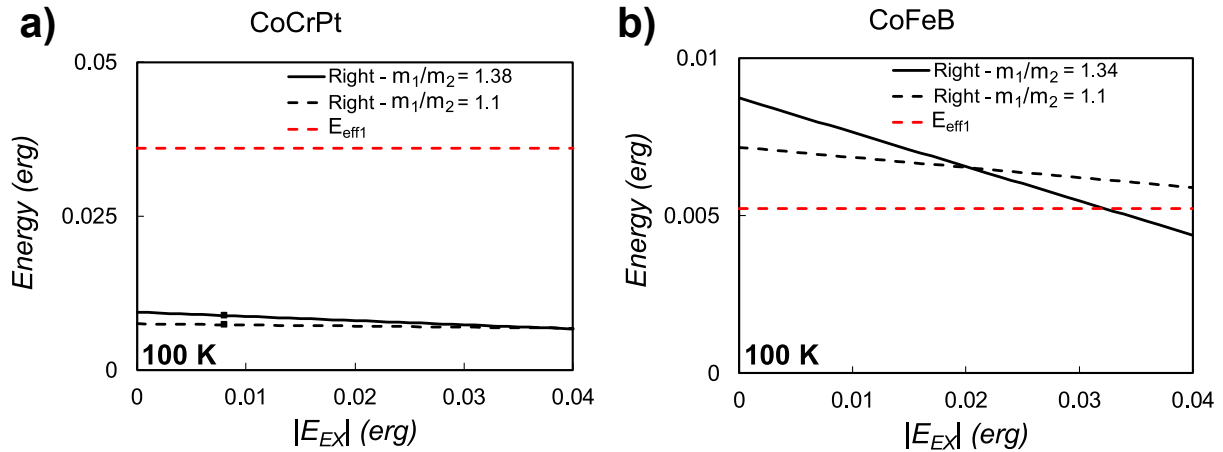
Figure 3.4 The left and right sides of the inequality $E_{eff1} < E_{eff2}*m_1/m_2 - 2|E_{EX}|*(m_1-m_2)/m_2$ plotted as a function of E_{EX} for the a) CoCrPt-Ru-CoCrPt and b) CoFeB-Ta-CoFeB SFM. The black solid and dashed lines labeled "Right – m_1/m_2" represents the right side of the inequality at different magnetic ratios. The left side of the inequality is represented by the red curve and is labeled E_{eff1}. The black squares shown in a) represent the observed exchange energy of the CoCrPt-Ru-CoCrPt SFM at 100K.
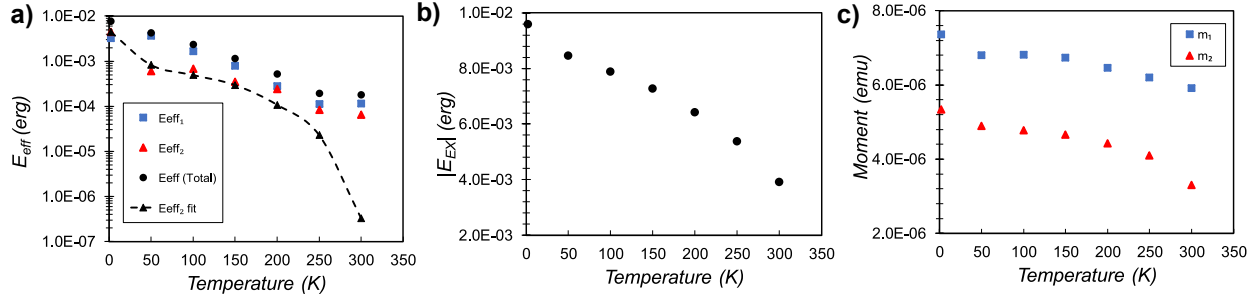
Figure 3.5 a) E_{eff1}, E_{eff2}, and E_{eff} (Total) plotted versus temperature. b) $|E_{EX}|$ plotted versus temperature. c) The magnetic moments, m_1 and m_2 of the 1.7nm and 1.3nm thick CoCrPt layers, respectively, plotted versus temperature.
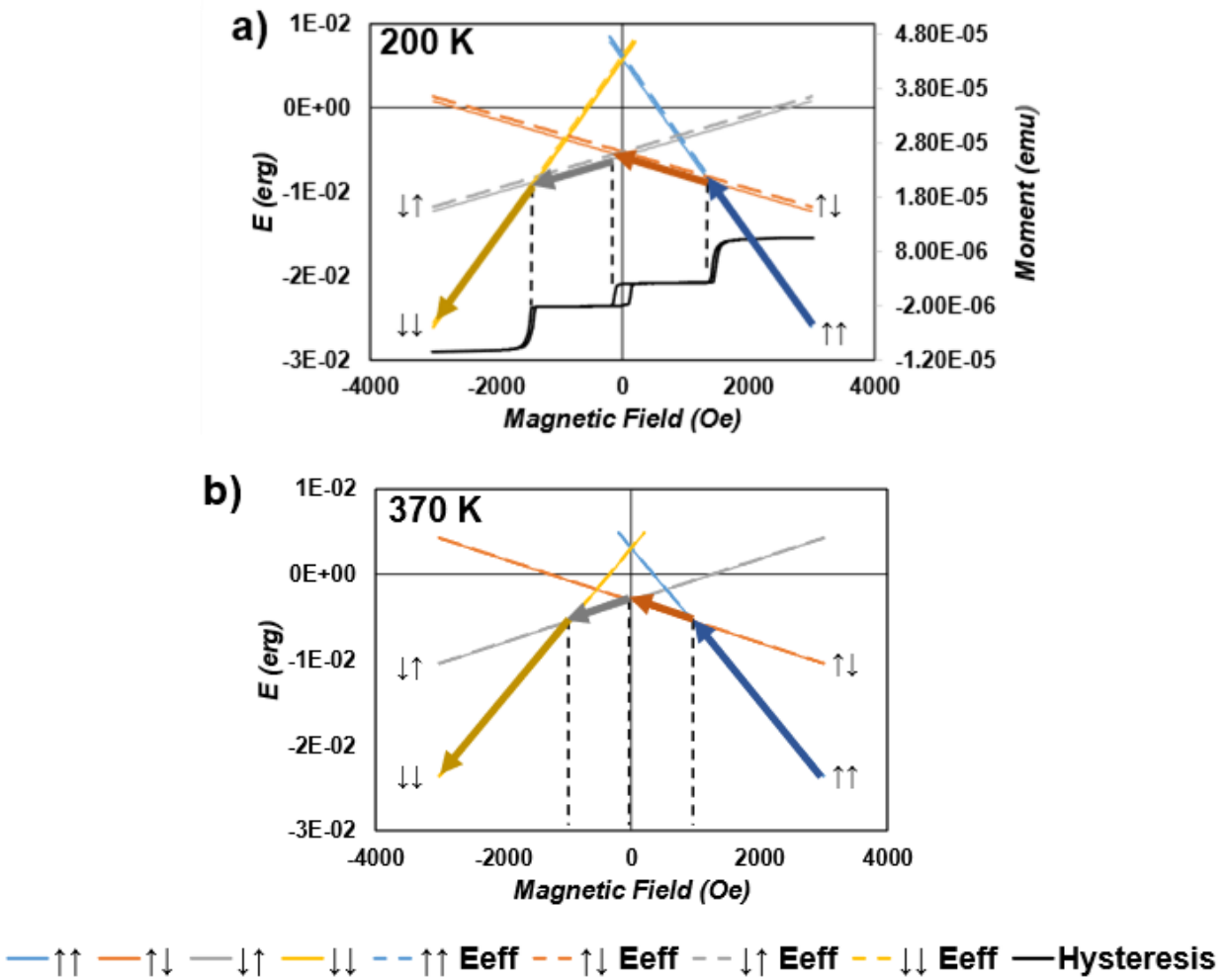
Figure 3.6 The energy diagram for the CoCrPt(1.7nm)/Ru(0.8nm)/CoCrPt(1.3nm) SFM at 200K and 370K, calculated from fitted parameters in Fig 3.5. The transition fields are indicated by the vertical dashed lines. The hysteresis curve measured at 200K is shown in a).

3.4 Conclusions

The magnetic properties of SFM trilayers are temperature dependent, and memory devices incorporating such structures can be expected to reliably operate under extreme conditions within the temperature range of 200K to 370K. To tailor the IEC energy and switching properties of the SFM structure for use in memory devices, it is necessary to understand the energies associated with their magnetization switching. In this section the IEC properties of CoCrPt-Ru-CoCrPt trilayer structures have been investigated from 2K to 300K. Building on previous work by Koplak *et al*. this work further elucidates the temperature-dependence of the potential barrier for magnetization reversal. We also show how H_B is calculated in the absence of a hysteresis curve featuring three subloops, which is necessary to calculate the IEC energy. The energy diagram technique has been applied to describe the magnetic transitions of CoCrPt-Ru-CoCrPt SFM as a function of temperature. Two types of hysteresis curves are observed, one above 50K with three subloops and the other at 2K with two magnetic transitions. Type III hysteresis is not seen in this SFM system due to the large E_{eff1} seen in the CoCrPt SFM which prevents the $E_{eff1} < E_{eff2} \cdot \frac{m_1}{m_2} - 2|E_{EX}| \cdot \frac{m_1 - m_2}{m_2}$ inequality from being satisfied. This is large E_{eff1} constant corresponds to the energy barrier between magnetization directions present in the CoCrPt film. The calculation of the potential barriers of the SFM at 2K was possible by measuring the minor loop associated with the switching of the thinner m_2 layer. Utilizing this diagram technique for CoCrPt-Ru-CoCrPt allows for the assessment and prediction of the different magnetic orientations present in the SFM system at any given temperature. Future work will include verifying this technique for CoCrPt/Ru/CoCrPt SFM structure with varying IEC energy as well as measuring the hysteresis loop properties at temperatures above 300K to confirm the predicted magnetic transitions. This technique can also be further applied to compensated AF coupled trilayers which could be of interest for ultrafast magnetic switching. The MTJs in the previous section could also benefit from this analysis since it could aid in the tuning of the IEC strength in the free and fixed SFM layers as temperature varies. Multi-level storage systems could also be realized where the free layer can be engineered to be switchable by spin currents using minor loops in the SFM hysteresis curve to engineer more than two resistance states.

4. DEVELOPMENT OF ULTRATHIN SEED LAYERS FOR HYBRID MAGNETO-PHOTONIC DEVICES

4.1 Introduction

All-optical switching (AOS) of magnetic thin films has been intensely investigated since the discovery of ultrafast demagnetization in nickel films upon irradiation with 60 fs laser pulses [10]. In this work, Beaurepaire *et al.* studied the spin dynamics of 22nm thick Ni films using a pump and probe time-resolved magneto-optical Kerr effect (TR-MOKE) apparatus. The magneto-optic Kerr rotation was recorded at every 2.3 ps time delay between the pump and probe pulses. Beaurepaire *et al.* investigated the spin and electron temperatures of the system at shorter timescales than previously studied. It was found that the magnetization of the Ni film is demagnetized rapidly in the first few ps after exposure to the fs laser pulse, which indicated a rapid increase in the spin temperature of the system (reported to reach ~575 K within 2 ps). A model that describes the interactions between the electron, spin, and phonon energy reservoirs was also formulated as a result of this work. Their publication provided an example of thermally-induced non-deterministic magnetization switching.

Later it was demonstrated in GdFeCo, that deterministic AOS is possible with the use of circularly polarized laser pulses, wherein the magnetization orientation of the film could be controlled by the helicity of light. As shown in Fig. 1.4, GdFeCo films were exposed to 40 fs laser pulses which switched the magnetic orientation within the laser irradiated spot size. Another important result of this paper is that the reversal of the GdFeCo was achieved with a single laser pulse as indicated in Fig. 4.1. In this figure, the magnetization of the film is observed with a polarizing microscope and the black and white regions correspond to magnetic domains in the GdFeCo films with opposite magnetic orientations. The output of the laser operating at 1 kHz is scanned across the film fast enough so that only a single laser pulse interacts with different regions of the thin film. Changing the helicity of the light (right and left circular polarized light are represented by σ^+ and σ^-, respectively) produces a change in the direction of magnetization in one domain but keeps the film saturated in the opposite domain. This ability to deterministically reverse the magnetization orientation in ultrafast time scales has led to a large volume of research in recent years for potential applications in electronics and computing applications.
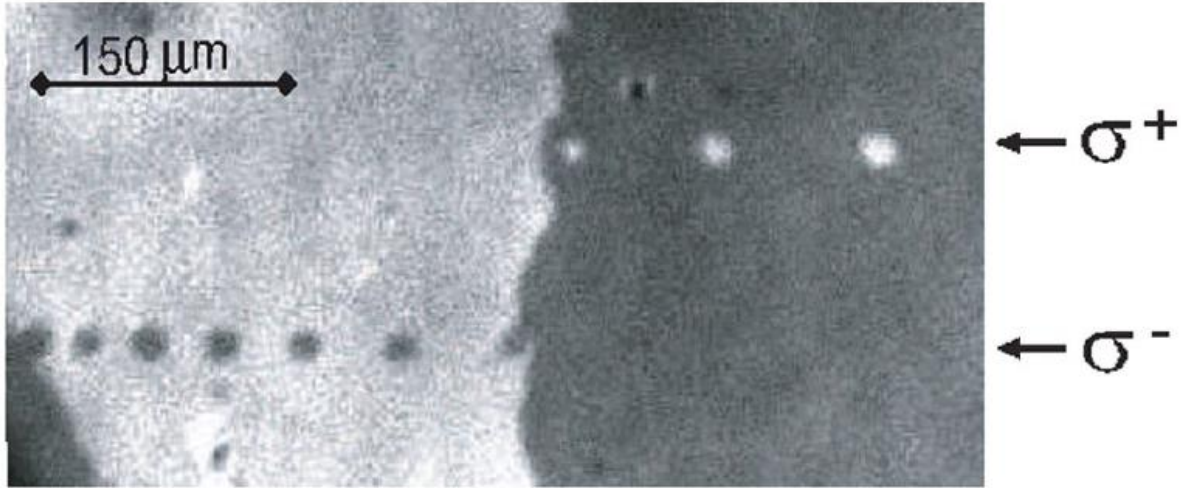
Figure 4.1 The effect of single 40-fs circular polarized laser pulses on the magnetic domains of Gd$_{22}$Fe$_{74.6}$Co$_{3.4}$. The domain pattern was obtained by sweeping at high-speed (~50 mm/s) circularly polarized beams across the surface so that every single laser pulse landed at a different spot. The laser fluence was about 2.9 mJ/cm^2. Figure from [12]. Figure used with permission from the American Physical Society.

It has been determined that magnetic switching observed in antiferromagnets can be interpreted based on inertial dynamics [54], where the equations of motion for the system contain kinetic energy and demonstrates inertia-like motion. This inertial-like motion implies that the driving force for switching does not have to be applied during the whole switching process and shorter currents and/or fields can be used for switching. This sets antiferromagnets apart from ferromagnetic materials, where the equation of motion, the Landau- Lifshitz-Gilbert equation, does not include inertial terms. In either case the reversal process can be illustrated by an energy diagram where the magnet must overcome an energy barrier for reversal to occur (Fig. 4.2). In a regular ferromagnet the driving force for reversal (a magnetic field or a spin current) must continuously drive the magnetization from one metastable state to another over the potential barrier. In the case of an antiferromagnet, the driving force does not have to act on the magnet throughout the whole process but can generate enough momentum for the magnet to overcome the potential barrier. The result is that shorter magnetic-field pulses or spin current can be used to achieve magnetic reversal in antiferromagnets. This also applies to SFM structures where the magnetic properties such as exchange coupling can be tuned. Thus, transition metal ferromagnetic materials

that do not normally demonstrate inertial-like motion could take advantage of inertia-driven dynamics when incorporated into an SFM structure.
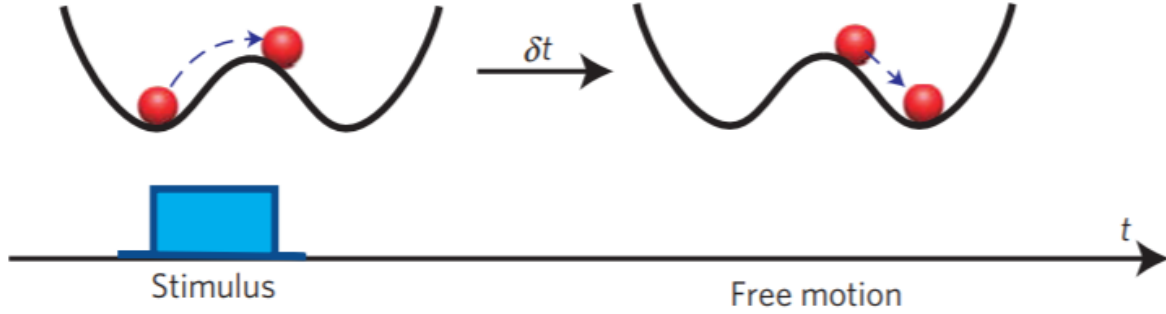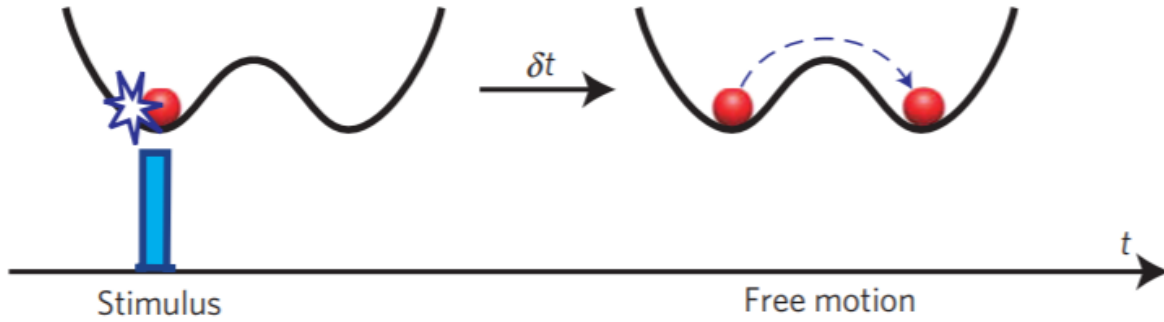
Figure 4.2 The non-inertial mechanism requires a continuous driving force that pulls the mass over the potential barrier. A similar scenario is realized in magnetization reversal through precessional motion in ferromagnets. In contrast, in the inertial mechanism, during the action of the driving force the coordinate of the particle is hardly changed, but the particle acquires enough momentum to overcome the barrier afterwards. Figure from [54]. Reprinted with permission, copyright 2009, Springer Nature.

In either case for optical magnetic switching of ferromagnets or antiferromagnets, the driving force of the magnetization switching is the magnetic field produced by the IFE, an effect whereby circularly polarized light induces an opto-magnetic field, H_{OM}, in the magnetic material throughout the duration of the light pulse. In Dutta *et al.* [17] finite element analysis (FEA) modelling was performed to study the enhancement of H_{OM} in nanopillars where the magnetic layer is adjacent to a plasmonic resonator. The H_{OM} field produced within the magnetic medium can be expressed

as shown in Eq. 4.1 where σ is helicity of the light (±1), β the magneto-optical susceptibility, E is the electric field vector, and E^* is the complex conjugate of the E-field. H_{OM} is proportional to the square of the electric field concentrated in the magnetic structure as well as to the magneto-optical susceptibility, β, defined by Eq. 4.2. The magneto-optical susceptibility describes the relationship between the Faraday rotation (θ_F) and the incident light wavelength (λ), the real refractive index (n), the thickness of magnetic film (d), and the saturation magnetization of the film (M_S).

$$H_{OM} = \sigma\beta|E \times E^*| \qquad (4.1)$$

$$\beta = \frac{\theta_F \lambda n}{\pi d M_S} \qquad (4.2)$$

To achieve the highest possible H_{OM} within the material, potential strategies could include searching for materials with high magneto-optical susceptibility or increasing the electric field strength within the magnetic film. This work is focused on increasing the electric field strength within the film by exciting localized surface plasmon resonances (LSPR) in the plasmonic film adjacent to the magnet, as shown in Fig. 1.8 from Dutta *et al.* [17]. In this work, in addition to utilizing magneto-plasmonic nano-structures for H_{OM} enhancement, we take advantage of the ability of plasmonic excitations to confine light to the nanoscale [55], [56] to enable AOS of memory and logic devices well beyond the diffraction limit of light. In this work we focus on using the refractory plasmonic material TiN to excite LSPR at the interface of magneto-plasmonic structures. TiN exhibits comparable optical properties to Au but also provides superior mechanical and thermal properties [57]–[62]. In terms of device fabrication, TiN is also CMOS-compatible allowing it to be utilized with existing memory and logic device fabrication techniques.

Regarding the choice of magnetic materials for magneto-photonic structures, enhancement of the opto-magnetic field is higher for dielectric materials, but there is still considerable enhancements of up to 4x with metallic magnets as reported for GdFeCo [17]. Experimental work for this thesis is focused on metallic magnetic films and multilayers with strong PMA, which have enabled ultra-high density magnetic recording [1]. Furthermore, with the incident light being normal to the film plane in Eq. 4.1, materials with PMA are necessary since the H_{OM} vector direction is predominantly perpendicular to the thin film plane. In particular the focus is on

hexagonal Co-based alloys such as $Co_{70}Cr_{18}Pt_{12}$ due to its high magnetocrystalline anisotropy and tunable magnetic properties. Storage densities of over 1 Tb/in^2 have been demonstrated using bit-patterned 20 nm CoCrPt islands [63]. Co/Pd multilayer stacks have also been investigating due to their high PMA and the tunability of their magnetic properties [64].

To achieve PMA in these Co-based magnetic films, it is necessary to control their crystalline structure so that the c-axis of the hexagonal lattice aligns perpendicular to the thin film plane. Most substrates such as silicon, MgO, or glass do not promote out-of-plane c-axis orientation in hcp Co-alloy thin films nor does growth on TiN. However, c-axis orientation can be achieved on a variety of substrates by utilizing seed layers whose lattice parameters closely match the crystallographic planes of hcp-Co alloys required to control the c-axis orientation in or out of plane. Seed layers that are often used are metals such as Ta, Ru, Ti, and CoCrPt(Ta) [41]. Since these seed layers are often optically lossy (meaning their absorption coefficients are relatively large), it is desirable to minimize their thickness to achieve strong spin-phonon coupling. It should also be noted that TiN cannot be grown on top of these Co-based alloys since plasmonic TiN requires growth temperatures ~600-800°C [62], [65] on lattice-matched substrates such as MgO. Thus, in this work, we seek the growth of CoPtCr with PMA on plasmonic TiN while minimizing the seed layer thickness to promote strong H_{OM} fields in the hybrid magneto-photonic structures proposed by Dutta *et al*. [17].

4.2   Materials and methods

TiN films were grown in a sputtering chamber (PVD Products, Inc.) with a base pressure of < 10-7 Torr. A Ti target was reactively sputtered in argon and nitrogen atmospheres onto MgO (100) and c-sapphire substrates which were held at 800 °C during growth [62]. The TiN growth was performed in a dedicated nitride chamber, after solvent cleaning of the substrates. The nitride and magnetic materials growth chambers are two separate deposition tools and the transfer of samples between chambers implies their exposure to air. Therefore, prior to depositing the magnetic layers on TiN, the samples were chemically cleaned. After the deposition of the TiN, the samples were taken out of the chamber and brought into an ISO Class 4 cleanroom. They were then sonicated with toluene, acetone, and isopropyl alcohol (in that order) for 5 minutes each. This procedure insured that the films were free of dust and particles before the deposition of the magnetic materials on top of the TiN.

The magnetic films including all underlayers and capping layers ($Co_{70}Cr_{18}Pt_{12}$, CoCrPtTa, Ta, Ru) were grown in a 4-target sputtering chamber (PVD Products, Inc.) with a base pressure of $< 10^{-7}$ Torr. In this chamber all films were grown without substrate heating or bias. The CoCrPt sputtering target has a nominal composition of $Co_{70}Cr_{18}Pt_{12}$. The deposition rates of these films were calibrated using atomic force microscopy (AFM). For this, the thickness of the deposited film was measured by creating a sharp step via a liftoff technique where the film is grown on a sacrificial layer that is later dissolved by acetone. CoCrPt, CoCrPtTa, Ta, and Ru were all typically deposited using a sputter power of 5-15 W and a sputter pressure of 1.8-3 mTorr. The $(CoCrPt)_xTa_y$ seed layer was grown by co-sputtering the $Co_{70}Cr_{18}Pt_{12}$ and Ta targets. Here, x and y refer to the composition of the film which is determined nominally by comparing the deposition rates of $Co_{70}Cr_{18}Pt_{12}$ and Ta. The composition is then controlled by adjusting the ratio of the sputter power of the two targets.

Magnetic hysteresis loops were collected using a Quantum Design MPMS-3 superconducting quantum interference device (SQUID) magnetometer with 10^{-8} emu sensitivity in the vibrating sample magnetometry (VSM) mode. All magnetic hysteresis loops presented in this chapter were performed at room temperature unless stated otherwise.

X-ray diffraction (XRD) data was collected using a Panalytical X'Pert PRO Materials Research Diffractometer, using a Cu anode ($K_\alpha = 1.54056$ Å), a PW308860/60 parabolic mirror with $1/32°$ slit for the incident beam optics, and a PW3098/27 Parallel Plate Collimator for diffracted beam optics. Lattice parameters and phases of the films are determined from ω-2θ peaks in the curves using the Bragg-Brentano geometry. The texture of the films is determined for a specific Bragg peak by centering the detector on the Bragg reflection and scanning ω with the detector fixed at 2θ.

4.3   Development of PMA CoCrPt grown on TiN with ultra-thin seed layers

$Co_{70}Cr_{18}Pt_{12}$ is a material of interest in memory and logic devices due to its large perpendicular magnetic anisotropy, high squareness, and a modest magnetization value. These magnetic properties are desirable for not only improving the thermal stability of memory devices, but also decreasing the current needed for switching the magnet via STT in MTJs [38], [66]. Another advantage of employing CoCrPt in such a device is that its anisotropy is dominated by magnetocrystalline, or bulk, anisotropy meaning the control of the crystalline growth of the

magnetic layer determines the magnetization orientation. One of the most common PMA magnetic film used in current memory devices, CoFeB, exhibits PMA due to interfacial anisotropy which is a thickness dependent term. Beyond 1-2nm thick CoFeB films will typically fail to retain PMA [1]. CoCrPt films demonstrate PMA for thicknesses much larger than this since the bulk anisotropy term is not thickness dependent and thus is more robust as a PMA material for logic and memory devices.

As mentioned earlier, to control the crystalline growth of CoCrPt with the c-axis pointing out of the plane of the film it is necessary to utilize lattice-matching seed layers deposited on substrates such as silicon or MgO as is the case for this work. A Ta/Ru bilayer, which was described in the Chapter 2, has been employed for seeding PMA in CoCrPt. However, the combined thickness of this bilayer is typically 15nm or more [41]. Reducing the thickness of this bilayer below 8nm produces a predominant in-plane anisotropy.

For an effective hybrid magneto-photonic structure, it is imperative to decrease the seed layer thickness, which is typically an optically lossy metal, while maintaining strong PMA properties of the magnetic film. It has been shown in the literature that co-sputtered $(CoCrPt)_x Ta_y$ seed layers can be employed to grow CoCrPt with PMA with higher crystallographic texture (or lower grain misorientation) than other common seed layers such as Ta/Hf, Ta/Ru, and Ta/Ti [41]. Utilizing $(CoCrPt)_x Ta_y$ as a seed layer is also advantageous in that the elemental composition of the seed layer and its magnetic properties can readily be varied.

The $(Co_{70}Cr_{18}Pt_{12})_x Ta_y$ co-sputtered seed layer is a versatile materials platform for controlling the growth of subsequent magnetic layer since Ta-doping can induce structural transformations of the seed. Due to its larger atomic radius, Ta incorporation into the hcp lattice of CoCrPt increases the unit cell parameter of CoCrPt. The atomic radii of each element are as follows: Ta = 0.147nm, Pt = 0.138nm, Cr = 0.128nm, and Co = 0.125nm. Beyond ~10% Ta-doping in $(CoCrPt)_x Ta_y$, it has been reported that the film becomes amorphous. In similar work, it has been reported that a structural transformation from hcp to fcc occurs with increased doping of Pt in a CoPrCrB film [67]. Both structural and magnetic property changes occur with Ta-doping of CoCrPt. The saturation magnetization decreases with increased Ta doping as follows: $M_S = 477$, 66, 5, and 1 emu/cc for y = 0, 20, 40, and 50%, respectively.

Figure 4.3 demonstrates the dramatic effect of seeded CoCrPt growth using a 1nm $(CoCrPt)_{60}Ta_{40}$ seed layer on top of MgO/TiN(30 nm). Figure 4.3a shows the hysteresis curve of

CoCrPt directly on the TiN plasmonic layer. It is evident that this film mostly exhibits in-plane anisotropy when not seeded with $(CoCrPt)_xTa_y$. Figure 4.3b shows the IP and OP hysteresis curves for seeded growth, where all other films and processes are kept the same. Strong PMA is exhibited by this sample and is the primary result of this section.
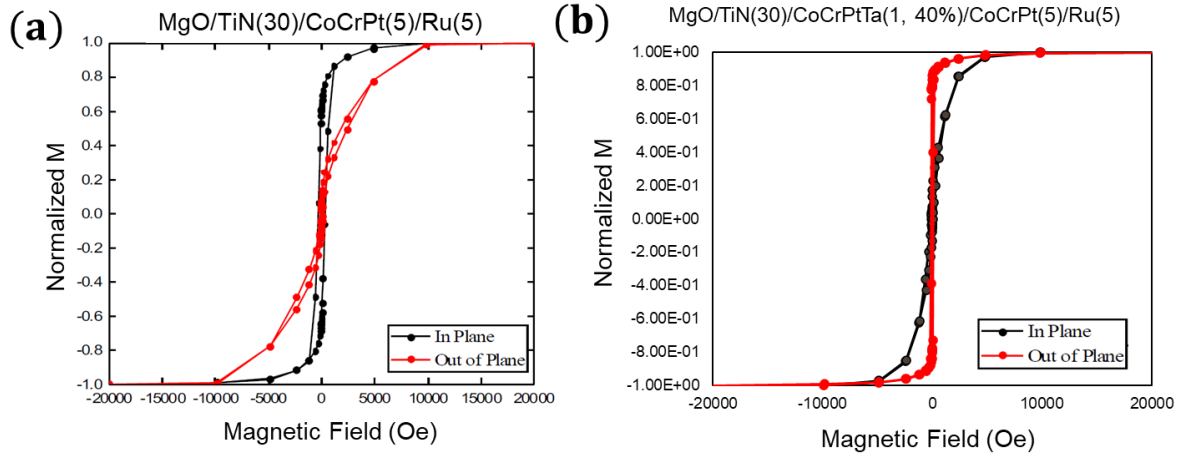
Figure 4.3 Hysteresis curves for a) CoCrPt grown on MgO/TiN without a seed layer and b) on MgO/TiN with a $(CoCrPt)_{60}Ta_{40}$ 1nm seed layer. CoCrPt grown on MgO/TiN without seed layers exhibits in-plane anisotropy.

Table 4.1 shows a comparison of the OP magnetic hysteresis curve properties between Ta/Ru and $(CoCrPt)_{60}Ta_{40}$ seeded growth of CoCrPt on MgO/TiN(30nm). The figures-of-merit (FOM) used to characterize the magnetic properties of the films include S^*, or squareness, and M_R^{OP}/M_R^{IP}, the ratio of the magnetic remanence of the IP and OP films. S^* is calculated by dividing the magnetization of the saturated film by the magnetization of the film after it is brought to zero field. M_R^{OP}/M_R^{IP} is calculated by dividing the magnetization at remanence of the film in the IP and OP direction after the field has been swept down from saturation (typically 2 T). While the magnetization is reduced for the $(CoCrPt)_{60}Ta_{40}$-seeded growth, the squareness (S^*) and the ratio of OP to IP magnetization remanence is increased substantially compared to Ta/Ru seed layer growth. This increase is indicative of a lower IP component of the magnetization, most likely due to increased c-axis alignment of the CoCrPt layer normal to the plane of the film.

78

Table 4.1 Comparison of magnetic properties for $Co_{70}Cr_{18}Pt_{12}$ grown on Ta(5nm)/Ru(10nm) vs. growth on $(Co_{70}Cr_{18}Pt_{12})_{60}Ta_{40}$(1nm) seed layers.

Substrate	Stack	M_S (emu/cc)	$S^* = M_R^{OP}/M_S^{OP}$	H_c (Oe)	M_R^{OP}/M_R^{IP}
MgO/TiN(30)	Ta(5)/Ru(10)/$Co_{70}Cr_{18}Pt_{12}$(5)/Ru(5)	547	0.878	169	7.46
MgO/TiN(30)	$(Co_{70}Cr_{18}Pt_{12})_{60}Ta_{40}$(1)/$Co_{70}Cr_{18}Pt_{12}$(5)/Ru(5)	474	0.82	81	9.41

Table 4.2 summarizes the magnetic FOM for 5nm of $Co_{70}Cr_{18}Pt_{12}$ grown on Si/SiO₂ and MgO/TiN(30nm) substrates and underlayers with various seed layers including: no seed layer, 1nm $(CoCrPt)_xTa_y$ with y = 20, 30, 40, 50% Ta, and the Ta(5nm)/Ru(10nm) bilayer. An increase of the FOM is evident with an increase of Ta content for growth on the Si/SiO₂ substrate. The maximum FOM for the MgO/TiN(30nm) is observed to occur for 40% Ta-doping of the (CoCrPt)Ta seed layer, whose magnetic hysteresis and magnetic properties are presented in Fig. 4.3b and Table 4.1, respectively. Overall a higher M_R^{OP}/M_R^{IP} is observed for the Si/SiO₂ substrate, which we ascribe to the difference in surface energy between the SiO₂ and TiN and its resulting effect on the structural evolution of the seed layers as the Ta composition varied. However, for a feasible magneto-photonic device in the visible wavelengths, it is necessary to have a transparent substrate such as MgO. It is evident from Table 4.2 that the 1nm $(CoCrPt)_{60}Ta_{40}$ seed layer is more effective than the 15nm thick Ta/Ru seed at promoting PMA in CoCrPt when grown on MgO/TiN(30nm). PMA CoCrPt growth is achieved with (CoCrPt)Ta seed layers at drastically reduced seed layer thickness and thus, this structure is amenable for designing plasmon-enhanced nanopillar arrays.

Table 4.2 Magnetic properties for CoCrPt grown on 1nm thick $(CoCrPt)_xTa_y$ seed layers with Ta-doping ranging between 20-50%, no seed layer, and Ta/Ru seed layers with the substrate being either Si/SiO_2 or MgO/TiN(30nm).

Seed layer	Si/SiO₂		MgO/TiN(30nm)	
	M_R^{OP}/M_R^{IP}	$S^*= M_R^{OP}/M_S^{OP}$	M_R^{OP}/M_R^{IP}	$S^* = M_R^{OP}/M_S^{OP}$
No seed	0.16	0.130	0.11	0.095
$(Co_{70}Cr_{18}Pt_{12})_{80}Ta_{20}$(1nm)	4.56	0.891	2.76	0.728
$(Co_{70}Cr_{18}Pt_{12})_{70}Ta_{30}$(1nm)	7.16	0.838	3.91	0.763
$(Co_{70}Cr_{18}Pt_{12})_{60}Ta_{40}$(1nm)	10.51	0.895	9.41	0.817
$(Co_{70}Cr_{18}Pt_{12})_{50}Ta_{50}$(1nm)	18.64	0.869	7.9	0.748
Ta(5nm)/Ru(10m)	19.10	0.933	7.46	0.878

To further understand the evolution of PMA in CoCrPt grown on (CoCrPt)Ta with various Ta content, the microstructural properties of the seed layer have been measured via XRD. The strong overlap of the cubic MgO (002) peak and the hcp Co (0002) peak has precluded conventional XRD analysis of the films grown onto MgO/TiN(30nm) samples. Therefore, the investigation of the seed layers focuses on films grown onto Si/SiO_2 so that the θ-2θ peaks can be resolved. It should also be noted that the 1nm (CoCrPt)Ta seed layer did not provide enough signal to be measured via XRD. Thus, a series of thicker 10nm thick $(CoCrPt)_xTa_y$ seed layers were grown with Ta composition y = 20, 30, 40, 50% onto oxidized Si(100) with 300nm oxidation layer. In this series of films, a 10nm Ta capping layer is used instead of Ru to eliminate the Ru (0002) peak which closely coincides with the Co (0002) peak.

Figure 4.4 summarizes the XRD θ-2θ data collected for $(CoCrPt)_xTa_y$ with y = 20, 30, 40, and 50% that are deposited as part of the following structure: $Si/SiO_2/(CoCrPt)_xTa_y$(10nm)/Ta(10nm). Curves are shifted along the y-axis (arbitrary units) for clarity. Figure 4.4 also includes Si/SiO_2/Ta(5nm)/Ru(10nm)/CoCrPt(5nm)/Ru(5nm) and Si/SiO_2/CoCrPt(5nm)/Ta(10nm) for comparison. The CoCrPt sample grown on Ta/Ru dual seed layers exhibits two peaks for the CoCrPt film including the Co (0002) peak and the Co ($10\bar{1}0$) peak, which are associated with PMA and IMA, respectively. The Co (0002) peak has a higher intensity for this sample, which confirms PMA in the sample is due to the c-axis orientation of the film. Other peaks that are present include Ru (0002) and Ru ($10\bar{1}1$) which are associated with the

seed and capping layer. It is evident from this spectrum that better analysis of the Co peaks can be facilitated by choosing another capping layer that does not have an overlapping peak. Thus, Ta is chosen as a capping layer for analyzing the (CoCrPt)Ta seed layer films. It should be noted that for this materials system, where anisotropy is dominated by magnetocrystalline anisotropy, the capping layer should not heavily influence the magnetic properties of the film below the capping layer (as is seen for CoFeB films capped with MgO [1]). The diffraction peaks for direct growth of CoCrPt on Si/SiO$_2$ (for the Si/SiO$_2$/CoCrPt(5nm)/Ta(10nm) sample) include weak reflections for the Co (0002) and Co (10$\bar{1}$0) planes, with the latter reflection having higher intensity. This explains the IP anisotropy of this film as also seen for direct growth on MgO/TiN(30nm). The α-Ta(110) and β-Ta(312) reflections are observed to be the strongest peaks for this spectrum.

The most salient observations from Fig. 4.4 pertain to the (CoCrPt)$_x$Ta$_y$ XRD reflections. It is seen that the 20% Ta-doped film exhibits very weak Co (0002) and Co (10$\bar{1}$0) reflections, indicating the film has poor crystalline structure. Reflections from the Ta cap are also not observed, which suggests the Ta is amorphous due to growth on top of the mostly amorphous (CoCrPt)$_{80}$Ta$_{20}$ seed layer. Above 20% Ta-doping, the Co peaks of the (CoCrPt)Ta become increasingly prominent as the Ta content is increased. This change in the structural properties appears to be consistent with similar work from Lee *et al*. [68], where an increase in Ta content leads to a decrease in grain size and increase of the magnetic anisotropy. It is worth noting that the Ta content used for optimal magnetic properties in literature is typically around 4%, and above 10% the (CoCrPt)Ta film is observed to be amorphous [41], [68]. This discrepancy with the work shown could be due to the way in which Ta content is defined. Here the Ta content is nominal and is based on the relative sputter deposition rates of each target during co-sputtering. The actual composition of the (CoCrPt)Ta film could be differ from the nominal composition and is left for future work to experimentally confirm if there is a significant difference.

As mentioned, starting at 30% Ta-doping the Co (0002) and Co (10$\bar{1}$0) peaks begin to increase. Additional reflections are observed from the Ta capping layer and correspond to the α-Ta and β-Ta, which are body-centered cubic and tetragonal polymorphs of Ta, respectively. The α-Ta phase is not present when Ta content of the seed layer is above 30%, which could be due to the increased crystalline structure of the (CoCrPt)Ta seed layer with increasing Ta content.

Figure 4.4 also shows a significant shift of the Co (0002) peak for Co peak associated with the CoCrPt grown on Ta/Ru seed layers (42.42°) as opposed to Co peaks associated with

(CoCrPt)Ta (~43.1°). This significant difference in peak position is associated with the lattice spacing which is dependent on the underlayers. The CoCrPt is pseudo-epitaxially grown on Ru (0002) and thus has a comparable lattice constant to Ru (with peak position 42°). The (CoCrPt)Ta seed layer with >30% Ta-doping adopts a spacing that minimized the lattice strain energy and is not constrained to the lattice underneath since it is grown on amorphous SiO_2.
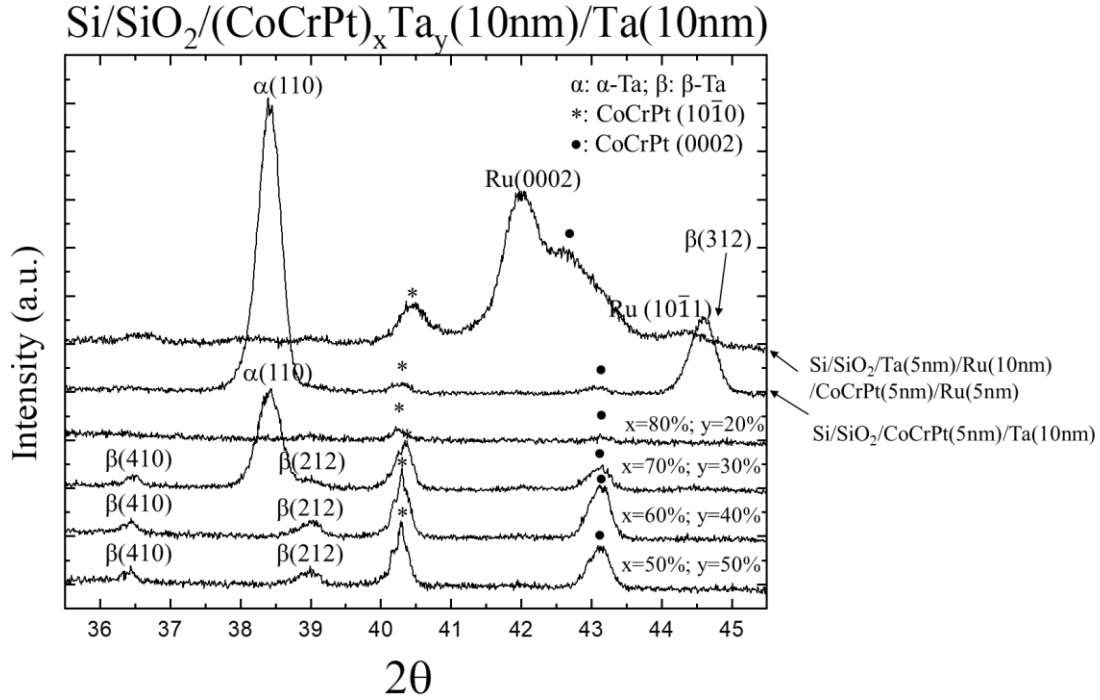
Figure 4.4 θ-2θ curves for Si/SiO₂/(CoCrPt)$_x$Ta$_y$(10nm)/Ta(10nm) with y = 20, 30, 40, and 50%. Reference samples Si/SiO₂/Ta(5nm)/Ru(10nm) and Si/SiO₂/CoCrPt(5nm)/Ta(10nm) are also included and are indicated in the plot.

Table 4.3 shows the integrated intensity of the Co (0002) and (10$\bar{1}$0) peaks associated with (CoCrPt)$_x$Ta$_y$ with y =30-50%. The ratio of these integrated intensities indicates a maximum for the Co (0002) peak at around 40%, and a minimum for 30% Ta. In our analysis the assumption is made that the structural changes observed in 10nm thick (CoCrPt)Ta seed layers also apply to 1nm thick films. While there may be additional factors affecting the structural properties at this ultrathin regime (enhanced lattice strain, structural defects, etc.) the magnetic observations of the corresponding CoCrPt layers for both 1nm and 10nm thick seed layers are consistent. The increase in PMA in CoCrPt when grown on (CoCrPt)Ta seed layers corresponds to increasing Ta content

and is evidenced by increasing Co (0002) peak intensities as well as the enhanced magnetic FOMs. Since CoCrPt thin films have predominantly magnetocrystalline anisotropy, the *S** FOM indicates the degree of texture of the film which is at a maximum for 40% Ta when grown on MgO/TiN. This also appears to be consistent with Table 4.3 where the ratio of integrated intensities for Co $(0002)/ (10\bar{1}0)$ is at a maximum for this Ta concentration.

Table 4.3 Integrated intensity of θ-2θ peaks shown in Fig. 4.4 and the ratio of the correspond integrated intensities for Co(0002) and Co($10\bar{1}0$)

Seed Layer	Integrated Intensity (a.u.) Curves of CoCrPtTa($10\bar{1}0$)	Integrated Intensity (a.u.) Curves of CoCrPtTa(0002)	Co(0002)/Co($10\bar{1}0$)
$(Co_{70}Cr_{18}Pt_{12})_{70}Ta_{30}$(1nm)	1440.524	894.449	0.621
$(Co_{70}Cr_{18}Pt_{12})_{60}Ta_{40}$(1nm)	1528.94	1920.28	1.256
$(Co_{70}Cr_{18}Pt_{12})_{50}Ta_{50}$(1nm)	1465.78	1544.27	1.054

4.4   Conclusions

A magneto-plasmonic hybrid material structure has been developed for potential use in plasmon-enhanced AOS to achieve ultrafast switching speeds in the fs time scale. Quaternary CoCrPtTa alloy seed layers deposited on TiN have been employed to control the growth orientation of CoCrPt thin films subsequently deposited, resulting in strong PMA growth with seed layers only 1nm thick. This has been achieved atop a TiN refractory plasmonic material, a candidate to replace conventional gold and silver plasmonic materials.

In this work the crystallographic properties and resulting magnetic properties of (CoCrPt)Ta seed layers were tuned by varying the Ta content during co-sputtered growth of $Co_{70}Cr_{18}Pt_{12}$ and Ta targets. The crystallographic properties of the $(CoCrPt)_xTa_y$ interlayers were controlled by changing the Ta content. Increasing Ta-doping of CoCrPt resulted initially in a crystalline to amorphous phase transformations, and the subsequent development of an hcp-crystalline structure characterized by the coexistence of ($10\bar{1}0$) and (0002) crystalline orientations. The desired (0002) orientation for PMA development was found to depend on the Ta-content. It was observed that increasing the Ta composition increased the presence of the Co (0002) and Co ($10\bar{1}0$) XRD reflections and subsequently increased the PMA of the CoCrPt.

This study was limited to normal incidence XRD measurements done on thicker 10nm seed layers grown on Si/SiO$_2$ substrates. Future work will include further investigation into the structural properties of 1nm (CoCrPt)Ta seed layers. Higher resolution, ultra-sensitive measurements can be achieved by using synchrotron x-ray sources. The study with conventional XRD can also be enhanced by utilizing grazing incidence XRD measurements to increase the sensitivity of the measurement to ultrathin films. Extended x-ray absorption fine structure (EXAFS) and x-ray absorption spectroscopy (XAS) can also be used to obtain an atomic description of the local environment. Transmission electron microscopy (TEM) will also be considered to investigate the local microstructure and continuity of the ultrathin films. The objectives of future work will be to further suppress the Co ($10\bar{1}0$) reflection peak and increase the PMA of the CoCrPt film.

Future work entails determining the optimal geometry (diameter and period) for nanopillar arrays containing the studied films. These arrays will be designed using finite element modelling such that opto-magnetic field (OMF) enhancements are observed in the nanostructures for a given wavelength. To determine this geometry the optical properties (n and k) will also have to be measured via ellipsometry in order to study them using finite element modelling.

5. MAGNETO-OPTICAL PROPERTIES AND GROWTH OF ALTERNATIVE MATERIALS FOR PLASMON-ENHANCED ALL-OPTICAL SWITCHING

5.1 Introduction

This chapter focuses on materials for plasmon-enhanced AOS and their corresponding strengths and weaknesses. Materials with large Kerr or Faraday rotation, fast magnetization dynamics, large PMA, low optical loss, and versatile materials growth are the strongest candidates for use in hybrid magneto-photonics devices.

CoCrPt, as discussed, is a material with large PMA and can be grown on a variety of substrates with a selection of seed layers to obtain c-axis growth perpendicular to the film plane. However, as here discussed, achieving Kerr contrast in this material for pump-probe AOS measurements is challenging as the Kerr rotation is not large. Also, since it is a metallic material, significant optical losses are predicted to occur that will diminish the H_{OM} enhancement.

Bismuth iron garnet (BIG) is another material of great interest for magneto-optic recording due to its large Faraday rotation and PMA, especially in the blue region of the visible spectrum [17], [69], [70]. A major advantage for BIG is that it is also a dielectric material, with low optical losses. Large enhancements in OMF have been numerically predicted for this material, as discussed in Chapter 1. Drawbacks to this material is that special substrates such as gadolinium gallium garnet (GGG) are needed to achieve the required garnet crystalline growth and magnetic properties. BIG also requires high in-situ growth temperatures and typically post-deposition annealing as well [70].

One potential alternative material is Co/Pd multilayered films. Multilayered films with large PMA, such as Co/Pd and Co/Pt have been investigated due to their tunable damping constant and their high precession frequencies of up to several tens of gigahertz [71]–[73]. Co/Pd multilayers have been shown to exhibit helicity-dependent AOS using 100 fs duration, 800 nm laser pulses [74]. Due to the tunability of the magnetic properties and potential application in plasmon-enhanced AOS structures, Co/Pd growth on TiN is investigated in this chapter.

Cobalt ferrite ($CoFe_2O_4$) is another material of interest due to its large Faraday rotation, similar to BIG [75]. This material is readily grown on quartz substrates by sputter deposition and exhibits PMA when grown in the cubic spinel (311) structure [75]. While not quite as low-loss as

BIG, cobalt ferrite films have relatively low absorption in the visible spectrum [76] and therefore off advantages over CoCrPt or Co/Pd multilayers. Another attractive feature of this material is that it can exhibit PMA for a large range of thicknesses from the nm to the μm scale.

5.2 Materials and methods

Refer to Section 4 for film growth details of CoCrPt as well as TiN. Bismuth iron garnet (BIG) films were deposited on GGG substrates via pulsed laser deposition (PLD). GGG(111) is chosen as the substrate because its lattice constants match well those of BIG, allowing BIG(111) films to grow with out-of-plane magnetic anisotropy [70]. The PLD used for deposition is a PVD Products, Inc. system with base pressure $< 8\mathrm{x}10^{-8}$ Torr equipped with a Lambda Physik 305i KrF excimer laser source (5 Hz, 248 nm wavelength). Heating during film growth is achieved with infrared lamps. The BIG target used for growth is stoichiometric BIG ($Bi_3Fe_5O_{12}$), the same stoichiometry desired in the resulting thin film. Following deposition the films are annealed using a Jipelec Rapid Thermal Annealing (RTA) system at 650 °C for 2 minutes in a nitrogen atmosphere with a temperature ramp-up rate of 50 °C/s. A Quanta 650 FESEM equipped with energy dispersive x-ray spectroscopy detector (EDS) is used to determine the composition of the BIG films. Co/Pd multilayers were grown at Tohoku University using DC sputtering.

Efforts to demonstrate AOS at Purdue employed a Ti-sapphire laser producing 800 nm, 100 fs duration pulses at 1 kHz repetition rate. A Quantum Design Physical Property Measurement System (PPMS) was used to set the initial magnetization of the films and measure the remanence before and after exposure to laser pulses (sensitivity: $\sim 10^{-6}$ emu). The PPMS was used for this purpose rather than the MPMS, even though the MPMS has better sensitivity. This is because the PPMS can be used in conjunction with a magnetic shield around the sample upon loading. This magnetic shield is made from a material with high magnetic permeability, allowing the sample to be unperturbed by internal magnetic fields from the motor of the VSM. In this way, influence of the environment is minimized when transporting the sample from the laser to the PPMS for measurements.

Magneto-optic Kerr effect (MOKE) measurements were collected in the polar MOKE geometry where the magnetization and incident light is parallel to the normal direction of the sample plane. MOKE hysteresis curves and Kerr microscopy images of CoCrPt films were

obtained at Radboud University. The Kerr rotation and ellipticity of CoCrPt films were measured at the Universidad Técnica Federico Santa María, Chile.

5.3 Growth of Bismuth Iron Garnet

Dielectric nanophotonic structures have been well studied in the literature over the past few years. Silicon, which is lossless at near infrared wavelengths, was one of the earliest materials studied for nanophotonics that does not involve metallic materials. Subsequently many other materials like GaAs, TiO_2, HfO_2 etc. have been used for lossless nanophotonics. The key principle is that a material with a high index of refraction would allow one to trap light into nanoscale dimensions, albeit diffraction limited. This principle together with advances in nano-fabrication capabilities has been leveraged to demonstrate nanophotonic applications such as low-loss metasurface lenses and polarizers, enhanced optical nonlinearities, etc. Our objective was to expand the material database for dielectric nanophotonics to include magnetic garnets. These materials such as Bismuth Iron Garnet ($Bi_3Fe_5O_{12}$-BIG) have an index of refraction around 2.4-2.7 in the near infrared wavelengths while having negligible losses. This makes them ideal candidates for nanophotonic metasurfaces with magneto-optical capabilities enabling design of ultrathin Faraday rotators for optical isolation.

Growth of BIG was done via PLD on GGG (111) substrates to promote epitaxial growth of BIG (111). Growth temperatures of this material were varied from 500-600 °C, and the oxygen pressure from 0-40 mTorr. Typically BIG is grown at temperatures of 450-600 °C and at 10-50 mTorr and after annealing the BIG films exhibit large polar Faraday rotation [70]. However, in our growth we found no evidence of magnetic remanence when the oxygen pressure was above 0 mTorr. One reason for this could be that the target-substrate distance in the PLD chamber used for growth is much larger (15cm) than the target-substrate distances reported in literature (typically under 7cm). Figure 5.1 displays the hysteresis curves of BIG grown with no oxygen flow at ~500-600 °C, 2.5 hour deposition time, and rapid thermal annealed (see methods section). It should be noted that the data points for the magnetic hysteresis curves were not collected at each field, but rather the film was brought up to a specific field and then measured at zero field (remanence). This was due to the fact that the GGG substrate has a large paramagnetic signal at even small applied fields.

87
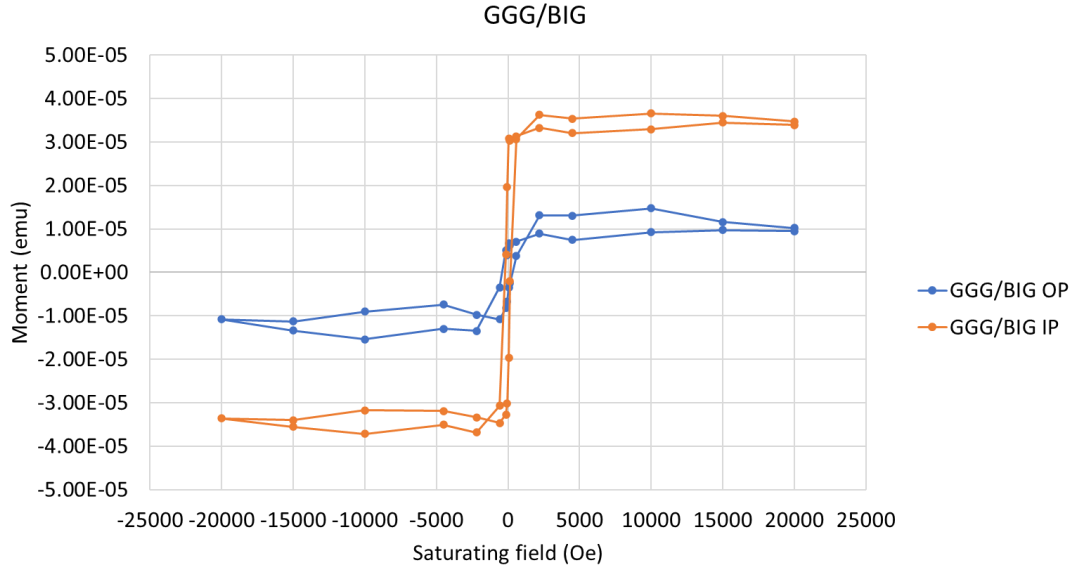
Figure 5.1 Magnetic hysteresis curves of GGG/BIG in the in-plane (IP) and out-of-plane (OP) directions. A higher magnetic remanence is seen in the OP direction.

One reason for the sub-optimal magnetic properties of the BIG film is likely due to the fact that our samples do not have the correct bismuth:iron ratio which is known to be critical to achieve the desirable magneto-optical properties. Fully substituted, or stoichiometric $Bi_3Fe_5O_{12}$ has high Faraday rotation and low optical losses [70]. Stoichiometric $Bi_3Fe_5O_{12}$ should have a Bi:Fe ratio of 0.6, where this ratio can be significantly affected by the ambient oxygen pressure and the target-substrate distance [77]. However, Fig. 5.2 which shows the EDS measurement of BIG, indicates that the Bi:Fe ratio is equal to 0.2. Further work is to be done to determine the optimal deposition conditions and annealing in BIG to obtain stoichiometric BIG to develop the required magnetic properties.
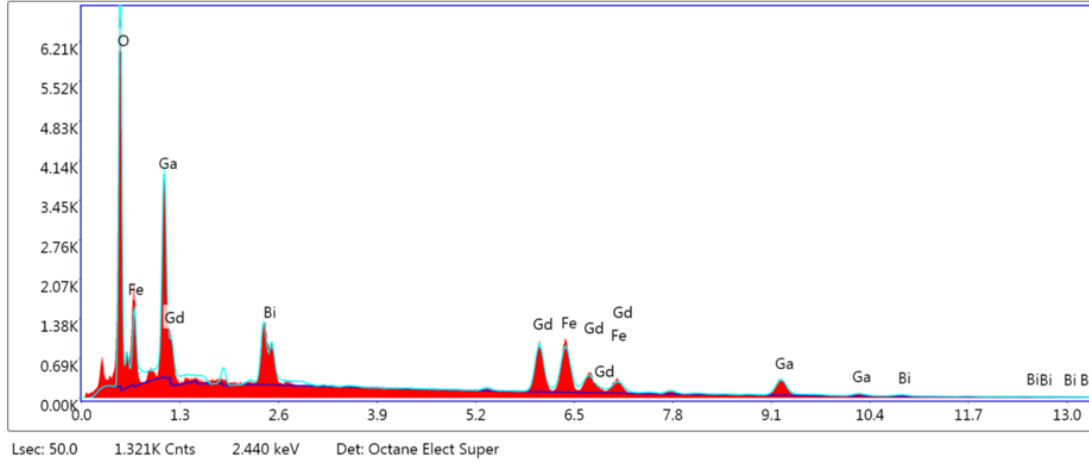
Figure 5.2 Energy-dispersive x-ray spectroscopy results for GGG/BIG grown with no oxygen flow. The Bi/Fe ratio is measured to be 0.2.

5.4   Magneto-optical properties of CoCrPt and all-optical switching

CoCrPt SFMs have been grown on Ta/Ru seed layers for the purpose of investigating their magneto-optical and AOS properties. Figure 5.3 shows polar MOKE hysteresis curves for Si/SiO$_2$/Ta(5nm)/Ru(10nm)/CoCrPt(1.7nm)/Ru(0.5nm)/CoCrPt(1.3nm)/Ru(x) where x = 5nm (a) and 2nm in (b). These films were grown with a 0.5nm Ru spacer layer to provide strong IEC strength. One issue with CoCrPt films for these optical measurements is that the Kerr rotation in these films is low. To improve the sensitivity of the measurement the Ru capping layer thickness was decreased. It was found that reducing the Ru capping layer thickness from 5nm to 2nm led to a 60% increase in Kerr signal, while still acting as an effective capping layer to protect the magnetic properties of the CoCrPt films.

Figure 5.4 presents Kerr loops for a structure with a thicker Ru exchange coupling interlayer of 0.8nm: Si/SiO$_2$/Ta(5nm)/Ru(10nm)/CoCrPt(1.7nm)/Ru(0.8nm)/CoCrPt(1.3nm)/Ru(x) where x = 5nm (a) and 2nm in (b). The Ru spacer layer was increased to 0.8nm in this structure with the aim being to study the differences in AOS between two SFMs with varying IEC strengths. Fig. 5.4a shows that the signal to noise ratio is very poor when the Ru capping layer is 5nm thick. This is expected since the MOKE hysteresis measurement records the reflection of polarized light from the films. When the Ru capping layer is thicker, more light is absorbed and/or reflected by the top surface before interacting with the magnetic layer underneath. Reducing the Ru capping layer to 2nm thick in Fig. 5.4b led to an increase of the Kerr rotation. The goal of reducing the capping

layer to increase Kerr rotation signal is to increase the ability to see domain contrast in the Kerr microscope images of the CoCrPt films during AOS fs pump-probe laser studies.

Figure 5.5 shows Kerr microscope images of (a) $Si/SiO_2/Ta(5nm)/Ru(10nm)/CoCrPt(5nm)Ru(2nm)$, (b) $Si/SiO_2/Ta(5nm)/Ru(10nm)/CoCrPt(1.7nm)/Ru(0.5nm)/CoCrPt(1.3nm)/Ru(2nm)$, and a 20nm TbCo film for reference. These images were obtained at Radboud University after exposure to multiple 100 fs, 1kHz, 800 nm pump laser pulses. Figure 5.5c shows clear evidence of AOS where the light and dark areas correspond to two different magnetization directions. However, no contrast can be observed for either CoCrPt film structure, despite the effort to reduce the Ru capping layer thickness.
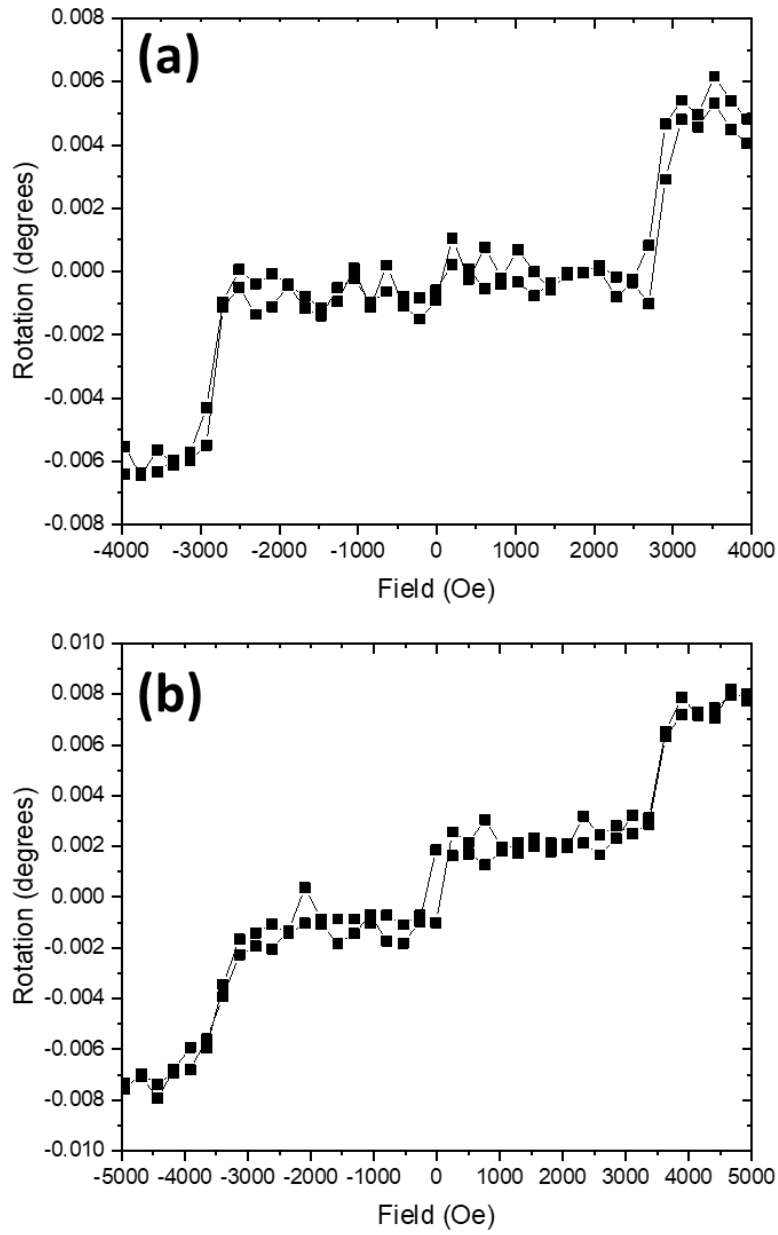
Figure 5.3 Kerr hysteresis curve at λ = 632.8 nm for (a)
Si/SiO$_2$/Ta(5nm)/Ru(10nm)/CoCrPt(1.7nm)/Ru(0.5nm)/CoCrPt(1.3nm)/Ru(5nm) and (b)
Si/SiO$_2$/Ta(5nm)/Ru(10nm)/CoCrPt(1.7nm)/Ru(0.5nm)/CoCrPt(1.3nm)/Ru(2nm) SFMs.
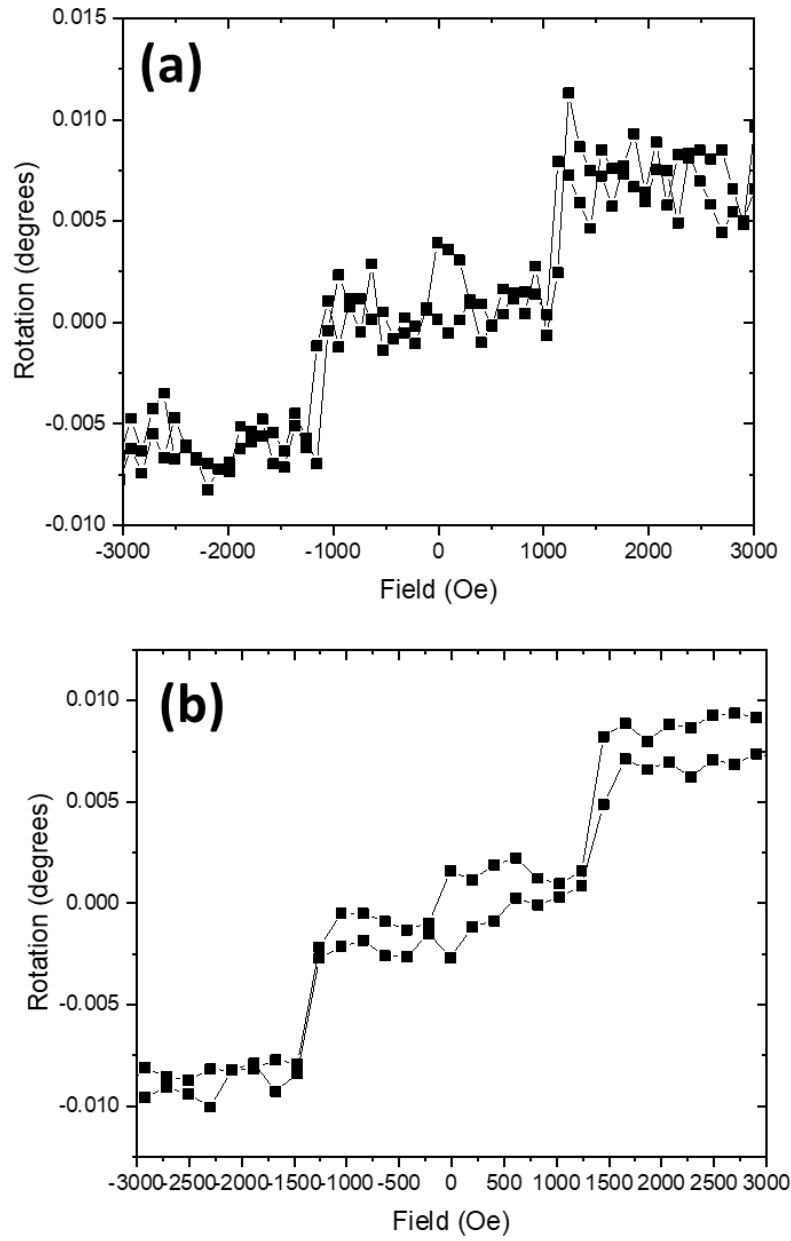
Figure 5.4 Kerr hysteresis curve at $\lambda = 632.8$ nm for (a) Si/SiO$_2$/Ta(5nm)/Ru(10 nm)/CoCrPt(1.7 nm)/Ru(0.8 nm)/CoCrPt(1.3 nm)/Ru(5 nm) and (b) Si/SiO$_2$/Ta(5 nm)/Ru(10 nm)/CoCrPt(1.7nm)/Ru(0.8 nm)/CoCrPt(1.3 nm)/Ru(2 nm) SFMs.

(a)   (b)   (c)

0.5 mm
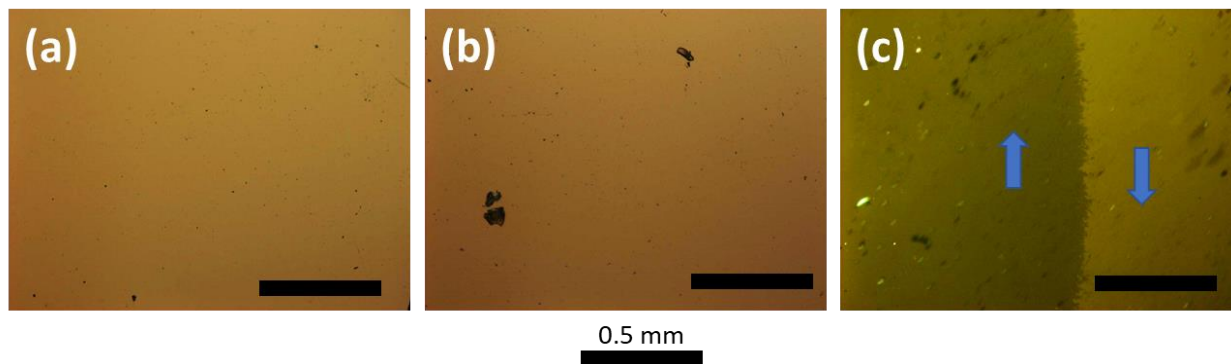
Figure 5.5 Magneto-optical microscopy images of a)
Si/SiO$_2$/Ta(5nm)/Ru(10nm)/CoCrPt(5nm)/Ru(2nm), b)
Si/SiO$_2$/Ta(5nm)/Ru(10nm)/CoCrPt(1.7nm)/Ru(0.5nm)/CoCrPt(1.3nm)/Ru(2nm), and c)
TbCo(20nm) for comparison. All images were taken after exposure to 100 fs, 800 nm pump laser
pulses. No contrast indicating magnetization switching is observed for the CoCrPt samples as it
is clearly observable in the reference TbCo sample.

Potential reasons for the lack of domain contrast observed in Fig. 5.5a &b could be that the films do not exhibit AOS for the laser pulses used, the films are too thin to provide enough signal, or the wavelength used to collect Kerr images of the films were potentially at a minimum of the dispersion relation of the Kerr rotation for CoCrPt (~630nm).

To study the wavelength dependence of the in Kerr rotation and ellipticity in the 400nm-1000nm wavelength range, measurements were performed at Universidad Técnica Federico Santa María, Chile on CoCrPt samples and are presented in Fig. 5.6. These CoCrPt structures were capped with Ta-oxide to further determine if an increase in Kerr rotation could be achieved over 2nm Ru capping layers. There is no significant increase found for the Kerr rotation of Ta-oxide capped CoCrPt versus Ru capped CoCrPt. No strong dependency of the Kerr rotation on wavelength is observed for the CoCrPt thin films (Fig. 5.6). There is, however, a trend towards higher ellipticity around 800nm-1000nm.

To overcome the limitation of low Kerr rotation or insufficient contrast in the CoCrPt films an experiment was performed to measure AOS utilizing the VSM before and after exposure to femtosecond laser pulses to detect changes in the remanent magnetization after light exposure. As described in the materials and methods section, films were first saturated in a 2 T field by inserting the sample into the VSM. The field was then brought to zero and the remanent moment was recorded. While being inserted or taken out of the VSM, a high-permeability magnetic shield surrounded the field to shield the films from magnetic fields originating from the VSM motor.

Films were then exposed to 100 fs, 800 nm, 1 kHz laser pulses for 30 seconds. After laser irradiation, the films were mounted in the VSM to measure the magnetization at zero applied field. The results of these experiments for MgO/Ta(5nm)/Ru(10nm)/CoCrPt(1.7nm)/Ru(0.6nm)/CoCrPt(1.3nm)/Ru(5nm) are shown in Fig 5.7 for varying laser fluence. The helicity of the laser pulses was also varied between right and left circularly polarization and irradiation was also performed with linearly polarized light. The y-axis in Fig. 5.7 is M_R/M_0, with M_R the magnetic remanence of the film after exposure to the fs laser pulses, and M_0 the initial remanence recorded after saturation via a 2 T applied magnetic field. $M_R/M_0 = 1$ indicates no change in the magnetization of the film, $M_R/M_0 = 0$ indicates complete demagnetization of the film, and $M_R/M_0 = -1$ indicates complete reversal of the magnetization. It was observed that for all laser fluences except for 15 mJ/cm^2, only partial or complete demagnetization occurred regardless of the polarization of the light. At 15 mJ/cm^2 laser fluence, the film is observed to reverse directions, almost completely ($M_R/M_0 \sim 0.75$-0.8). However, the reversal at 15 mJ/cm^2 occurs regardless of light helicity. This suggests that the AOS observed is not helicity-dependent switching, meaning the physical mechanism for magnetization reversal is not due to IFE but rather a heating mechanism. Below 15 mJ/cm^2 laser fluence the temperature of the film is likely not high enough for switching, but the demagnetization effect increases from 5-10 mJ/cm^2. Above 15 mJ/cm^2 laser fluence the films are believed to be damaged. Future work for this experiment will include measuring single ferromagnetic CoCrPt films as well as studying CoCrPt SFM films with varied IEC strengths.
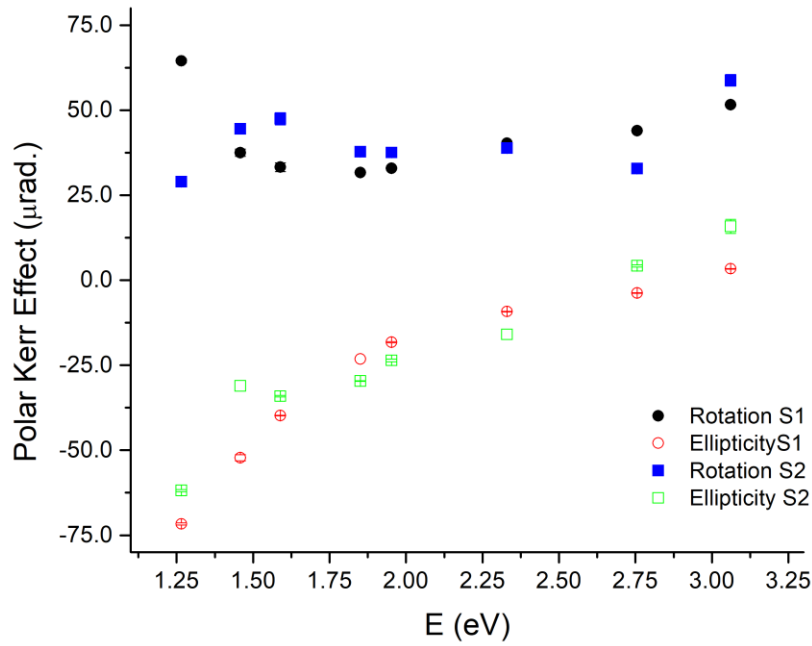
Figure 5.6 Polar Kerr rotation and ellipticity as a function of light energy for S1: MgO/Ta(5nm)/Ru(10nm)/CoCrPt(5nm)/Ta-oxide(10nm) and S2: Si/SiO$_2$(300nm)/Ta(5nm)/Ru(10nm)/CoCrPt(5nm)/Ta-oxide(10nm) films.
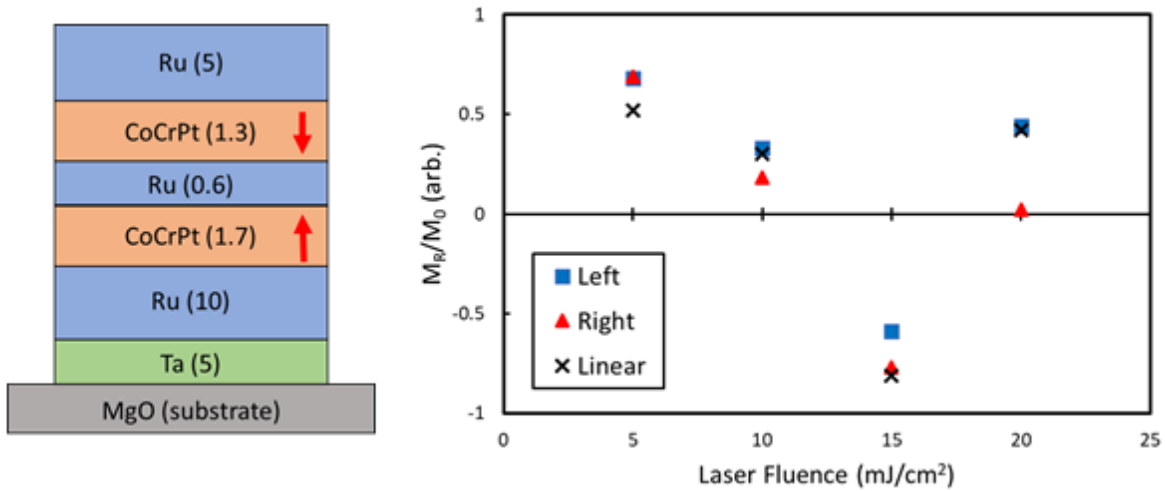
Figure 5.7 All-optical switching results for films whose cross-section is shown on the left. M$_R$/M$_0$ represents the ratio of the magnetic remanence after exposure to femtosecond laser pulses and the remanence of before exposure. **M$_R$/M$_0$** is plotted as a function of laser fluence.

5.5 Magneto-optical properties of Co/Pd and growth on TiN with ultra-thin seed layers

[Co/Pd]$_n$ multilayers are typically grown on oxidized silicon using Ta, Pd, or Ti seed layers to achieve Co (111) growth perpendicular to the film plane. The origin of the PMA in Co/Pd multilayers derives from the interface anisotropy due to broken symmetry and electronic hybridization at the Co/Pd interfaces [72]. Thus, one problem to overcome is the growth of Co/Pd multilayers on TiN underlayers which will be required to employ LSPR to induce large opto-magnetic fields in TiN/[Co/Pd]$_n$ structures. The thickness of any seed layers inserted between the TiN and [Co/Pd]$_n$ interface will also need to be minimized to ensure effective enhancement of the OMF into the magnet. Figure 5.8 shows the polar MOKE hysteresis curves of [Co(0.4nm)/Pd(0.8nm)]$_5$ on c-sapphire/TiN(10nm) substrates employing Ti seed layers of different thicknesses from 1nm-5nm. PMA in the Co/Pd multilayers is strong even when grown on 1 nm thick Ti seed layers and exhibit squareness values close to unity. [Co(0.4nm)/Pd(0.8nm)] multilayers were also directly deposited without Ti seed layers on various substrates (Fig. 5.9) such as (a) c-sapphire/TiN(10nm), (b) MgO/TiN(30nm), and (c) Si/SiO$_2$. Figure 5.9a-b show reduced squareness and Fig. 5.9c shows similar squareness to the results presented in Fig. 5.8. However, a substrate which is transparent in the visible spectrum is required for AOS switching experiments. Ultimately sapphire is chosen as the substrate since it is both transparent in the visible region and is widely available.

Figure 5.10 shows the films: (a) sapphire/TiN(30)/Ti(1)/[Co(0.4)/Pd(0.8)]$_8$/ZnO(10) and (b) sapphire/TiN(30)/Ti(1)/[Co(0.4)/Pd(0.8)]$_8$/ZnO(10) with all thicknesses in nm. The films were sputtered onto 2 side polished 2" sapphire wafers. Measurements of the Kerr rotation in Fig. 5.10 were taken at various positions away from the center of the wafer to ensure uniformity in magnetic properties across the wafer area. Future work will involve the patterning of these two thin films into nanopillar arrays for AOS time-resolved studies. The diameter and the period of the arrays will be determined by FEA modelling to excite LSPR at the pump laser. The FEA model utilizes the Wave Optics module of COMSOL software with the Electromagnetic Waves, Frequency Domain interface, where the electromagnetic wave equation is solved in the frequency domain for various nanopillar array designs to determine the nature of the plasmonic resonances. Further improvements to these films were made by replacing the MgO/Ta capping layer with a ZnO dielectric capping layer which will reduce optical losses. The number of Co/Pd periods in the

multilayer was incremented from 5 to 8 to increase the Kerr rotation signal and to make the film closer in thickness to the metallic magnet modelled in [17].
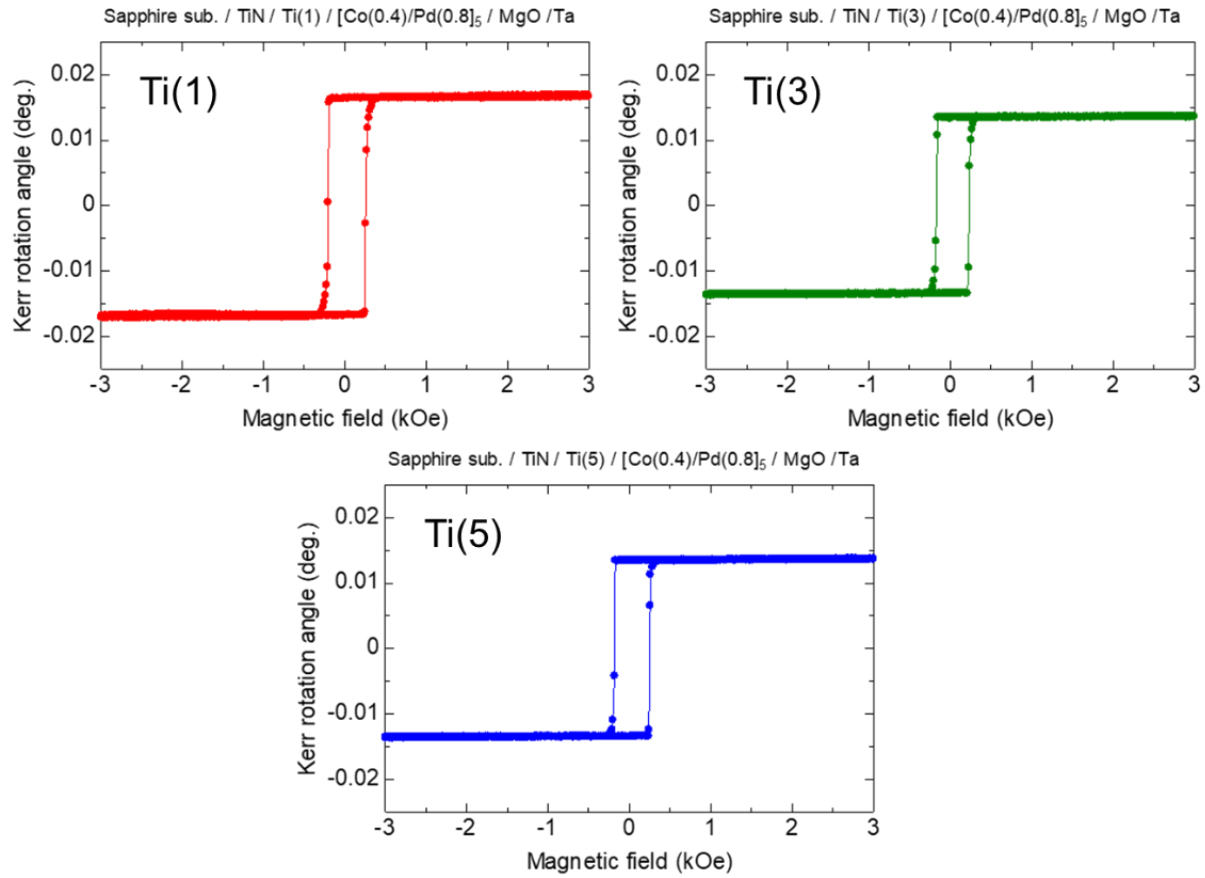
Figure 5.8 Kerr hysteresis curves at λ = 400nm of sapphire/TiN(30nm)/Ti(x)/[Co(0.4nm)/Pd(0.8nm)]₅/MgO(3nm)/Ta(2nm) films with x = 1 to 5 nm.
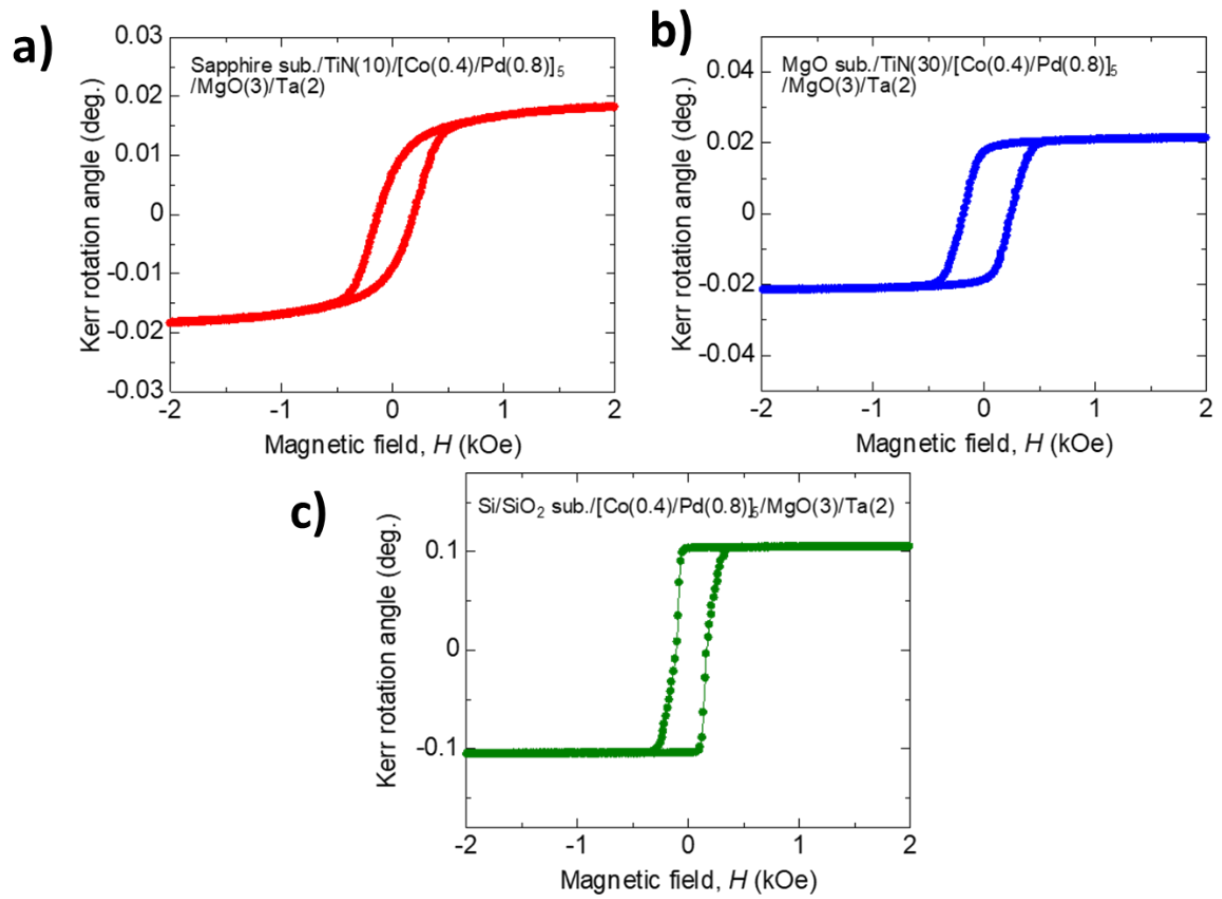
Figure 5.9 Kerr hysteresis curves at λ = 400nm of [Co(0.4nm)/Pd(0.8nm)]$_5$/MgO(3nm)/Ta(2nm) grown on a) sapphire/TiN(10nm), b) MgO/TiN(30nm), and c) Si/SiO$_2$ substrates/underlayers.
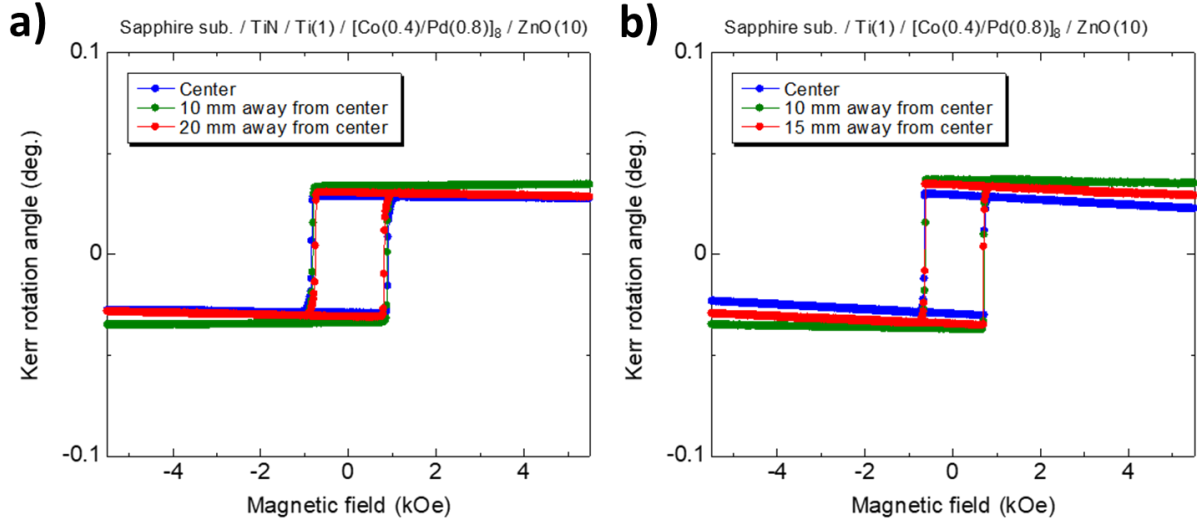
Figure 5.10 Kerr hysteresis curves at λ = 400nm of a) sapphire/TiN(30nm)/Ti(1nm)/[Co(0.4nm)/Pd(0.8nm)]$_8$/ZnO(10nm) and b) the same structure but without the 1 nm Ti seed layer.

5.6   Modelling Opto-magnetic Field Enhancement in CoFe$_2$O$_4$

As mentioned, Co-ferrite (CoFe$_2$O$_4$) ferromagnetic thin films are attractive candidates for use in magneto-photonic structures given their high Faraday rotations, PMA, and versatility with regard to deposition. This work adopts the model used by Dutta *et al.* [17] to consider the OMF enhancement of Co-ferrite nanopillar arrays using TiN plasmonic resonators. Modelling is performed using the COMSOL (FEA software) wave optics module with the Electromagnetic Waves, Frequency Domain interface. This software is often used to model nanostructures that are on the scale of the wavelength of light used and allows for the modelling of plasmonic resonances. The input parameters for the model include the real and imaginary electrical permittivities of each constituent material. The real and imaginary electrical permittivity (ε_1 and ε_2) is calculated from the real and imaginary part of the refractive index (n and k) as $\varepsilon_1 = n^2\text{-}k^2$ and $\varepsilon_2 = 2nk$. Co-ferrite n and k values, which are wavelength-dependent, are used from [76] and shown in Fig. 5.11. In the model, light is incident normal to the nanopillar structure from the substrate side as shown in Fig. 1.8.
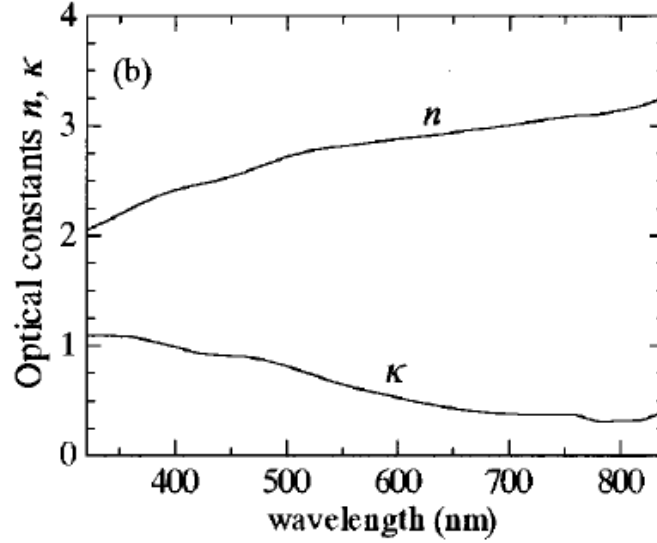
Figure 5.11 Optical properties of $CoFe_2O_4$ (*n* and *k*) from [76] used for OMF enhancement modelling in COMSOL.

As shown by Eq. 4.1 and Eq. 4.2, the *H_{OM}* field can be expressed as the cross-product of the electric field and its complex conjugate multiplied by the opto-magnetic susceptibility. Upon excitation of LSPR, the *H_{OM}* field is increased due to the higher intensity of the electric field. This is achieved by designing the diameter of the pillars and the period such that LSPR is excited at a given wavelength. Two nanopillar arrays were modeled (depicted in Fig. 5.12) with the following film structure: Magneto-plasmonic stack (MPS) – sapphire/TiN(30nm)/$CoFe_2O_4$(10nm)/ZnO(10nm) and non-plasmonic stack (NPS) – sapphire/$CoFe_2O_4$(10nm)/ZnO(10nm). The NPS does not have the TiN layer and thus should not have a plasmon resonance.
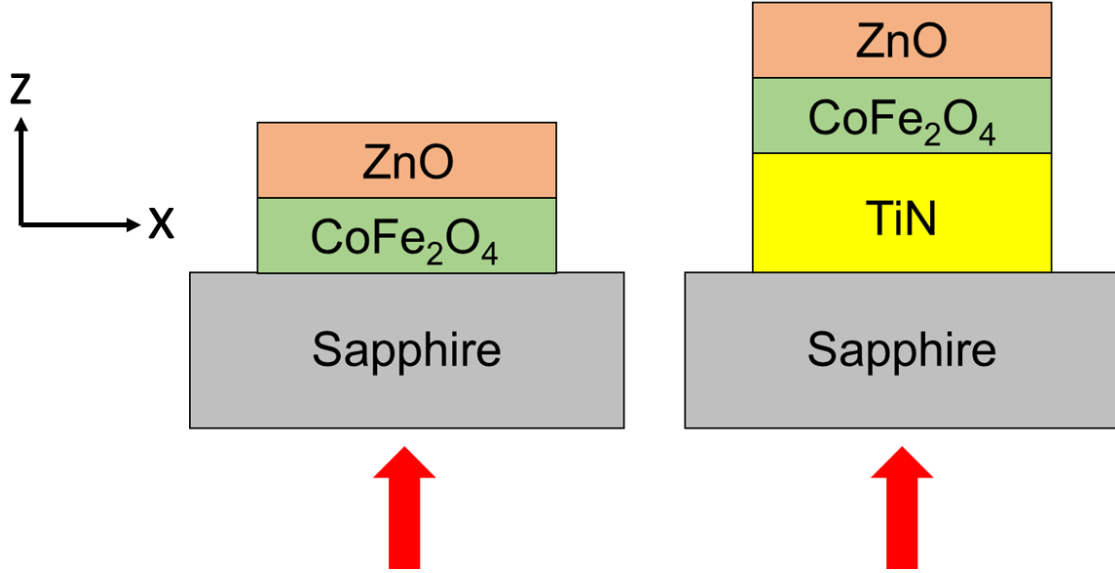
Figure 5.12 Cross-section of left: MPS and right: NPS consisting of sapphire/CoFe$_2$O$_4$(10nm)/ZnO(10nm) and sapphire/TiN(30nm)/CoFe$_2$O$_4$(10nm)/ZnO(10nm), respectively. Red arrows indicate the incident irradiation in the z-direction.

Figure 5.13 presents the $|ExE^*|$ values for the Co-ferrite NPS and MPS with 20nm diameter and 30nm period at λ = 700 nm. The ratio of the $|ExE^*|$ values for the MPS/NPS gives the ratio of the z-component of the H_{OM} for these two structures since H_{OM} is proportional to $|ExE^*|$. The $|ExE^*|$ value is reported as function of the length of the pillar (with x = 0 nm corresponding to the center of the nanopillar diameter) at the interface of the substrate (or TiN) and the Co-ferrite layer. It was found that a peak in this ratio occurs around 700nm due to the plasmon resonance that occurs at this wavelength for the given diameter and pillar. Comparing $|ExE^*|$ at the center (x = 0 nm) of the MPS and NPS, an enhancement in H_{OM} of ~2.6x is seen for this nanopillar array with and without the TiN plasmonic layer. This enhancement is comparable to results reported for 10nm GdFeCo (~3.4x enhancement) in Dutta *et al*. [17] where the nanopillar diameter is 50nm. Figure 5.14 displays the electric field intensity plots (V/m) for the 20 nm diameter, 30 nm period MPS (a)-(c) and NPS (d)-(f) nanopillars described in Figs. 5.12 and 5.13. It is observed that the electric field intensity is the highest at the TiN/CoFe2O4 interface (Fig. 5.14a) for the MPS structure indicating a plasmon resonance for this wavelength (700nm) at this interface.
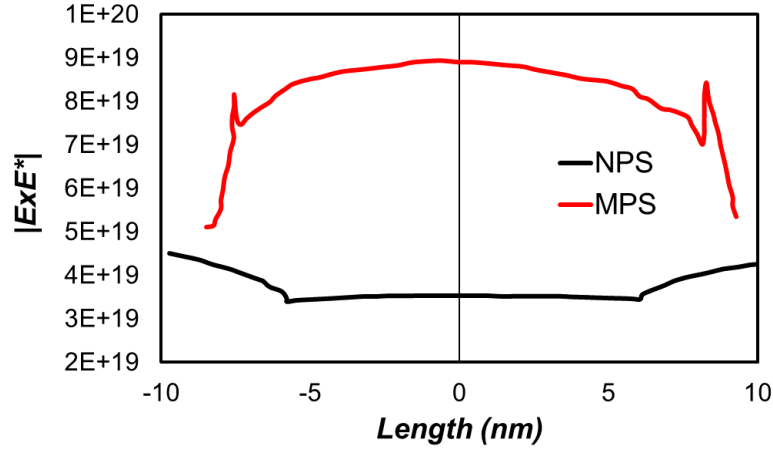
Figure 5.13 $|ExE^*|$ (at $\lambda = 700$nm) along the TiN-CoFe$_2$O$_4$ and sapphire-CoFe$_2$O$_4$ interface for the MPS and NPS stacks, respectively. The nanopillar geometry consists of 20nm diameter pillars with 30nm period. The MPS stack is: sapphire/TiN(30nm)/CoFe$_2$O$_4$(10nm)/ZnO (10nm). The NPS stack is: sapphire/CoFe$_2$O$_4$(10nm)/ZnO (10nm).
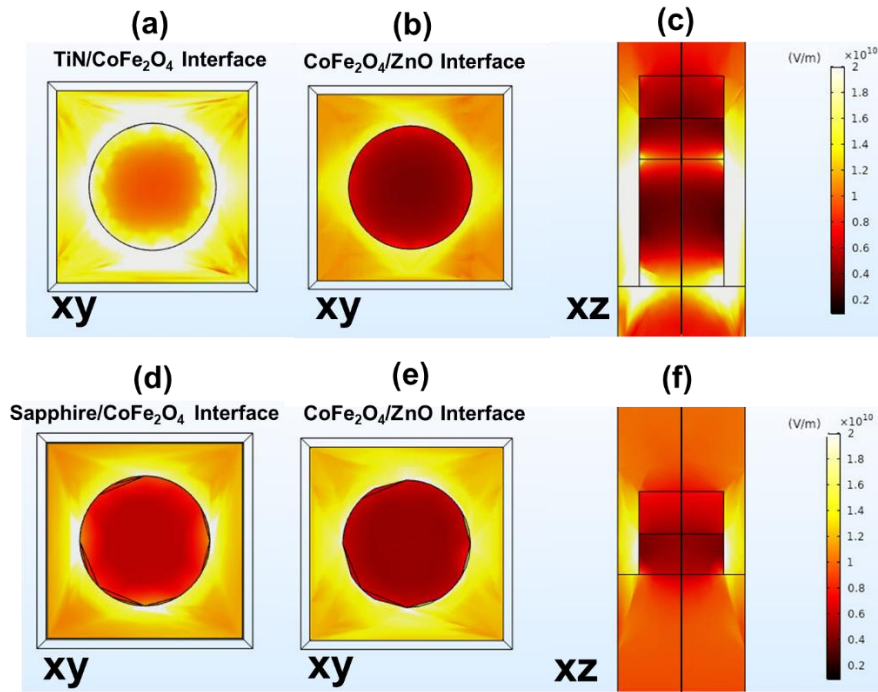
Figure 5.14 (a)-(b) Electric field intensity (V/m) plots along the xy (TiN/CoFe$_2$O$_4$) and xy (CoFe$_2$O$_4$/ZnO) interfaces, respectively, for the MPS structure described in Figs. 5.12 and 5.13. (c) Electric field intensity for the MPS in the xz plane. (d)-(e) Electric field intensity plots along the xy (sapphire/CoFe$_2$O$_4$) and xy (CoFe$_2$O$_4$/ZnO) interfaces, respectively, for the NPS structure without TiN. (f) Electric field intensity for the NPS in the xz plane. Illumination is with circularly polarized light at 700nm wavelength.

Table 5.1 displays the OMF enhancement values at $\lambda = 700$nm for the Co-ferrite MPS and NPS structures at various pillar diameters and periods for either the Co-ferrite/ZnO interface or the (substrate or TiN)/Co-Ferrite interface. The enhancement values are shown to be lower at the magnet/cap interface for this structure, similar to models of OMF enhancement in BIG [17]. The largest values of enhancement at the substrate or TiN/Co-ferrite interface occur at 20nm diameter and 30nm period. At the (substrate or TiN)/Co-Ferrite interface, the enhancement is observed to decrease as the ratio of the diameter to period increases. However, for the Co-Ferrite/ZnO interface the enhancement ratio appears to be at a maximum value for 60nm diameter and70 nm period. Further work is to be done to determine the optimum ratio of the diameter to period and whether the highest enhancements can be obtained at the bottom or top interface of the Co-Ferrite layer.

The enhancement values for 20nm diameter, 30nm period nanopillar arrays at $\lambda = 400$nm, 700nm, and 800nm are reported in Table 5.2. Wavelengths of 400nm and 800nm are reported due to being the extrema of wavelengths considered, while 700nm is the wavelength at which the highest enhancement is observed. It is reported that the enhancement varies dramatically between the bottom or top interface of the Co-ferrite layer. This likely depends on the specific material that is studied as seen in Dutta *et al*. where the enhancement for a dielectric (metallic) magnetic layer is observed at the bottom (top) of the magnetic layer interface. The Co-Ferrite dielectric material studied here appears to coincide with these results, with the highest enhancements observed at the bottom interface of the magnetic layer. The peak in the enhancement values around 700nm indicate that an LSPR is achieved in the structure.

Table 5.1 The ratio of $|ExE*|$ for the MPS and the NPS at $\lambda = 700$ nm for various pillar diameters and periods (measured center-to-center for the nanopillars). The MPS stack is: sapphire/TiN(30nm)/CoFe$_2$O$_4$(10nm)/ZnO (10nm). The NPS stack is: sapphire/CoFe$_2$O$_4$(10nm)/ZnO(10nm).

Diameter (nm)	Period (nm)	$|ExE*|$ (MPS)/ $|ExE*|$ (NPS)	
		Co-ferrite/ZnO interface	(substrate or TiN)/Co-Ferrite interface
20	30	0.68	2.57
30	40	0.95	2.44
40	50	1.25	2.29
50	60	1.38	2.4
60	70	1.43	1.9
70	80	1.37	1.67
80	90	1.32	1.51
90	100	1.17	1.31

Table 5.2 The ratio of $|ExE*|$ for the MPS and NPS (with stacks the same as in Table 5.1) for 20nm diameter, 30nm period nanopillar arrays at varying wavelength.

Wavelength (nm)	$|ExE*|$ (MPS)/ $|ExE*|$ (NPS)	
	Co-ferrite/ZnO interface	(substrate or TiN)/Co-Ferrite interface
400	0.67	0.4
700	0.68	2.57
800	0.31	2.15

5.7   Conclusions

In conclusion, BIG, CoCrPt, Co/Pd multilayers, and Co-ferrite films which are potential materials for plasmon-enhanced AOS are investigated. Materials with large Kerr or Faraday rotation, fast magnetization dynamics, large PMA, low optical loss, and versatile materials growth are the strongest candidates for use in hybrid magneto-photonics devices. The Kerr rotation of

CoCrPt and CoCrPt /Ru/CoCrPt SFMs have been measured as a function of wavelength. It was observed that no Kerr contrast was observed in Kerr microscope images, which could be due to poor Kerr rotation or poor signal due to the small thicknesses of the CoCrPt layers.

Co/Pd multilayers have been grown on TiN underlayers with ultrathin Ti seed layers down to 1nm thickness. MOKE hysteresis loops were measure and indicate Co/Pd has a high Kerr rotation. Co/Pd thin films were deposited on 2" diameter c-sapphire wafers and exhibited uniform magneto-optical properties across the wafer area and these will be patterned at Spintec, France for time-resolved measurements at Radboud University, The Netherlands. Further work in progress will determine the nanopillar geometry and periodicity in such structures to promote OMF enhancement. BIG, a dielectric material predicted to have large OMF enhancement, has been deposited PLD but remains to have the incorrect stoichiometry as well as magnetic properties. Future work will involve further investigation into the processing parameters and how they affect the magnetic properties, crystal structure and stoichiometry.

The OMF enhancement utilizing Co-ferrite films on TiN layers has been modelled. An OMF enhancement of up to ~2.6x has been observed for nanopillars of sapphire (substrate)/TiN(30nm)/$CoFe_2O_4$(10nm)/ZnO(10nm) with a nanopillar diameter 20nm and period 30nm. Future work will require the deposition and characterization of these Co-ferrite films on TiN to determine Co-ferrite will exhibit PMA on these underlayers with or without a suitable seed layer. Fabrication of the nanopillars using the design provided by modelling will then ensue. Once the nanopillars are fabricated, the AOS switching properties will then be investigated using a pump-and-probe laser setup.

As of writing this thesis, similar modelling work is in progress to calculate the potential opto-magnetic field enhancements in CoCrPt and Co/Pd multilayers.

6. CONCLUSIONS

6.1   Thesis summary

The work presented in this dissertation describes the successful sputter deposition and magnetic characterization of CoCrPt/Ru/CoCrPt SFM, the key building block for the realization of novel ultrafast switching MTJ devices. The growth of CoCrPt thin films on Ta/Ru dual seed layers results in a magnetic material with high c-axis orientation perpendicular to the thin film plane as evidenced from the FWHM of 4.13° derived from XRD rocking curve measurements. The magnetic properties of these alloys including: large magnetic anisotropy, high magnetic squareness ~1 and minimized IP remanence, makes them very attractive for SFM spintronics applications. The exchange energy between AFM coupled CoCrPt layers spaced by Ru is readily controlled by the Ru layer thickness. A maximum value for IEC -0.04 erg/cm^2 was determined for a 0.4nm Ru layer and an external applied magnetic field of ~2500 Oe was required to break the exchange. Magnetic transitions in CoCrPt/Ru/CoCrPt SFM structures as a function of temperature were measured and analyzed using an energy balance equation (Eq. 3.1) based on the Zeeman energy, IEC energy, and potential barrier energies for magnetization reversal. The analysis was expanded to predict magnetization transitions of the SFM systems by either interpolation or extrapolation if the temperature dependence of the magnetic moment, IEC energy, and the potential barriers are known. This result is important for successfully incorporating these SFM structures in recording and logic devices where the performance of the SFM structure is expected to be affected by the device operational temperature environment.

Unpatterned MTJ thin film structures were grown that incorporated reference and recording SFM structures separated by an MgO tunnel barrier. Magnetic measurements of these MTJ stacks show that CoCrPt grown directly on 0.5nm thick MgO barriers, hinders the development of the required magnetic properties for subsequently grown SFM free layers. This is most likely due to the inability of the MgO layers grown thus far, to induce the correct crystalline growth in CoPtCr due to deficiencies in the MgO crystalline structure, the presence of pinholes and excessive roughness. To circumvent this deficiency, CoCrPtTa seed layers were deposited on MgO prior to deposition of CoPtCr which resulted in improvements of the SFM magnetic characteristics. However, to obtain the necessary SFM magnetic properties to be used as a free layer in an MTJ

device, further materials development is needed to improve the crystalline structure of both MgO and the free layer SFM. This development will be guided in the future by CIPT measurements to determine the TMR ratio required for a working MTJ device. Future work will also include patterning of the blanket films into a full MTJ device to perform time-resolved resistance measurements to determine the switching speed of the device. This work will be conducted in collaboration with researchers at Spintec in Grenoble, France.

This dissertation has also presented the successful growth of CoCrPt onto the plasmonic material TiN using ultrathin (CoCrPt)Ta seed layers. The magnetic and crystallographic properties of the CoCrPt and (CoCrPt)Ta seed have been investigated as a function of the Ta-content in the seed layer is well as its thickness. High squareness and PMA were measured in CoCrPt films grown on CoCrPtTa interlayer thickness down to 1nm. The crystallographic properties of the $(CoCrPt)_x Ta_y$ interlayers were controlled by changing the Ta content. Increasing Ta-doping of CoCrPt resulted initially in a crystalline to amorphous phase transformations, and the subsequent development of an hcp-crystalline structure characterized by the coexistence of $(10\bar{1}0)$ and (0002) crystalline orientations. The desired (0002) orientation for PMA development was found to depend on the Ta-content. Optimal magnetic properties are observed in the CoCrPt layer when the 1nm (CoCrPt)Ta seed layer contains 40% Ta, nominally . This work paves the way for CoCrPt alloys to be used with TiN for applications in plasmon-enhanced AOS experiments. Co/Pd multilayered films have also been grown with large PMA on TiN underlayers using ultrathin Ti interlayers in collaboration with researchers at Tohoku University, Japan. Initial work on depositing BIG films on GGG has been performed and shows that the Bi:Fe ratio is largely deficient and future work needs to provide a solution to achieve the correct stoichiometry in BIG.

In addition to PMA, candidate magnetic materials for AOS studies are required to exhibit large Kerr rotation at the wavelength of the pump laser employed in time-resolved pump-probe Kerr measurements with fs sources. To this effect, the magneto-optical properties of CoCrPt FM and CoCrPt SFM films have been investigated as a function of wavelength. It has been determined that the Kerr rotation and Kerr contrast of these films is currently too small and needs to be optimized to enable AOS measurements. The Co/Pd multilayer films studied show higher Kerr rotation and are to be explored as an alternative material for plasmon-enhanced AOS. Co-ferrites are an attractive material for these applications due to its large Faraday rotation, robust deposition qualities, and its availability. Co-ferrite films have been modeled in plasmonic nanopillars

107

containing TiN as the plasmonic material. Enhancements in the opto-magnetic field at $\lambda = 700$ nm in these structures have been observed up to ~2.6x for 20nm diameter, 30nm period nanopillar arrays.

6.2   Research outlook and future work

Plasmon-enhanced All-optical Switching of a Magnetic Tunnel Junction

It has been demonstrated that all-optical switching can be utilized in spintronic devices such as the MTJ. The miniaturization of modern recording and logic devices down to single nm scales introduce an additional challenge to confine light to those dimensions. With the correct geometry and materials layer adjacent to the magnetic recording layer of the MTJ, it is possible to excite localized surface plasmon resonances which couple the incident light with the functional magnetic layers of an MTJ device. Furthermore, when excited with circularly polarized light this plasmon resonance can enhance the opto-magnetic field (OMF) generated within a magnetic film, allowing switching in a nonthermal manner via the inverse Faraday effect and by changing the helicity of light, the out-of-plane magnetization can be switching reversibly. This approach will help pave the way to sub-wavelength on-chip photonic devices that can switch at THz rates, much faster than current precession-limited switching of non-volatile devices.

The proposed future work will build upon previous results in which the plasmon resonance of a nanoscale magnetic structure was modeled. This modeling effort will help determine the proper geometry and materials needed to induce a plasmon resonance in an MTJ structure in order to more efficiently couple the incident light to the device for all-optical switching. The objectives for this future work are as follows: 1) Model and demonstrate plasmon-enhanced switching of a magnetic nanopillar utilizing a metallic layer such as gold adjacent to the magnetic material to induce a plasmon resonance. 2) Incorporate this structure as a recoding layer in an MTJ device that will be capable of electrically reading out the magnetic state of the recording layer as it is optically switched. 3) Demonstrate increased efficiency of switching by comparing laser fluence required to switch a device with and without an induced plasmon resonance. 4) Investigate the dynamic characteristics of plasmon-enhanced switching via pump-and-probe measurements.

To successfully meet these objects, the project will proceed in the following order: 1) Magnetic materials such as Co/Pd or Co-ferrites multilayers adjacent to a metallic layer with low loss will be modeled using finite element analysis software to determine the correct geometry of

the nanomagnet to excite a plasmon resonance at a given wavelength. 2) The nanomagnets will be fabricated, and the dynamic properties of the nanomagnets will be assessed using fs optical pulses in a pump and probe laser setup. 3) An MTJ device will be fabricated, incorporating the plasmon resonance structure. The dynamics of the MTJ still then be explored using optical and electrical characterization.

All-optical switching (AOS) via fs laser pulses of a recording layer in an MTJ device has recently been demonstrated [78]. A GdFeCo magnetic layer was switched using linearly polarized, 1.55μm, 400 fs laser pulses. The reversal mechanism is a thermal process, where the GdFeCo is brought into a non-equilibrium state. As shown in Fig. 6.1a, the MTJ stack consists of a Co/Pd multilayer reference layer, an MgO tunnel barrier, and a GdFeCo free layer capped with a transparent conducting layer of ITO. The top ITO layer allows for electrical readout of the device (Fig. 6.1b) while being transparent to the laser pulse, allowing the device to be written by AOS and electrically read. Fig. 6.1c-d shows magneto-optic Kerr images of the device before and after it is exposed to a single laser pulse and demonstrates complete reversal of the free layer. Fig. 6.1e shows the resistance change of the device after it is reversed using a magnetic field. This change of resistance is then used as a benchmark for the change in resistance seen as a 0.5 Hz laser is used to switch the device as seen in Fig. 6.1f.

In this case the device is quite large, 12μm, such that it is on the same order of size as the spot size of the laser used which is 20μm. As the device is scaled down to the nanometer regime, it will be imperative to efficiently couple the incoming laser pulse to the device. Utilizing a carefully designed low-loss metallic layer such as gold adjacent to the free layer of the device, a localized surface plasmon resonance can be induced in order to efficiently heat the GdFeCo layer to its non-equilibrium state. This will not only decrease the energy needed for switching, but also allow for AOS to be confined to the nanoscale.

Another advantage of inducing a plasmon resonance is the increase of the opto-magnetic field (OMF) induced in a material with the use of circularly polarized light as shown by Dutta *et al.* [17]. With the use large opto-magnetic fields, the switching of the magnetic material can be nonthermal in nature. Thus, a wider variety of new materials can be explored for AOS, including higher anisotropy materials.
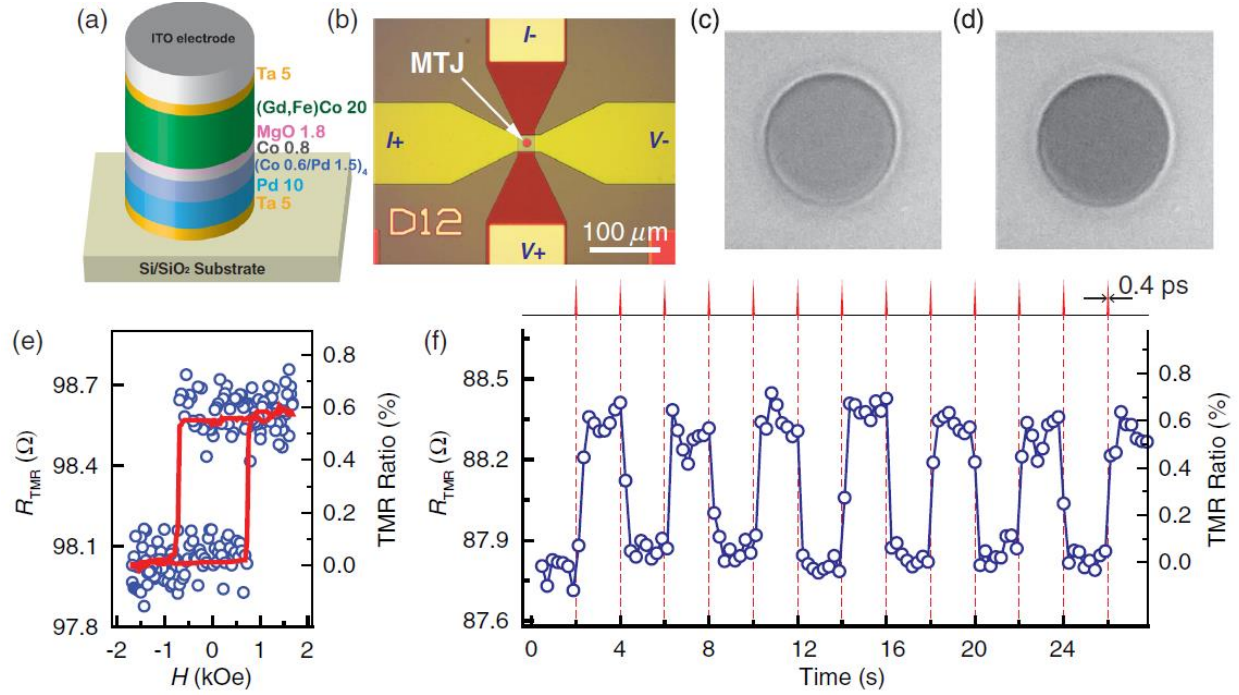
Figure 6.1 (a) Cross-section of the MTJ device, (b) Optical image of the MTJ device with patterned electrodes, (c)-(d) Kerr microscope images of the pillar before and after exposure to a single laser pulse, (e) Resistance change of the MTJ as a magnetic field is swept from positive to negative magnetization saturation, and (f) Resistance change of the device as it switched with 0.5 Hz laser pulses. Figure from [78]. Reprinted with permission, copyright American Physical Society.

Figure 6.2 illustrates the cross-section of the proposed device. The structure is similar to the structure shown in Fig. 6.1a. However, there is a gold layer inserted at the interface between the recording of "free" magnetic layer and the top contact. The geometry of this device is to be determined for a given laser pulse wavelength such that a plasmon resonance will be induced by the Au layer.

110
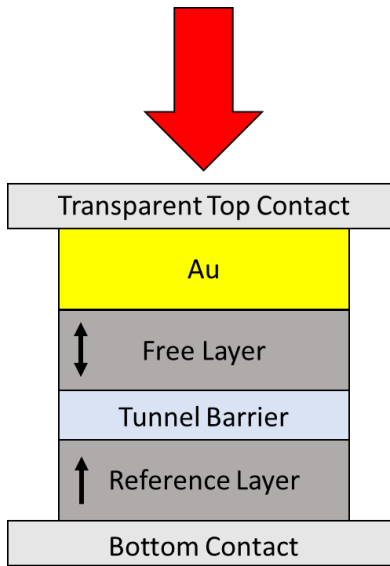
Figure 6.2 Cross-section of the proposed plasmon-enhanced MTJ AOS structure. Black arrows indicate the magnetization direction of the recording and reference layers. The red arrow indicated the incident laser pulse which is at normal incidence.

REFERENCES

[1]   S. Ikeda *et al.*, "A perpendicular-anisotropy CoFeB – MgO magnetic tunnel junction," *Nat. Mater.*, vol. 9, no. 9, pp. 721–724, 2010.

[2]   J. C. Slonczewski, "Current-driven excitation of magnetic multilayers," *J. Magn. Magn. Mater.*, vol. 159, no. 1–2, pp. L1–L7, 1996.

[3]   D. C. Ralph and M. D. Stiles, "Spin transfer torques," *J. Magn. Magn. Mater.*, vol. 320, no. 7, pp. 1190–1216, 2008.

[4]   H. Zhao *et al.*, "Sub-200ps spin transfer torque switching in in-plane magnetic tunnel junctions with interface perpendicular anisotropy," *J. Phys. D. Appl. Phys.*, vol. 45, no. 2, 2012.

[5]   D. E. Nikonov and I. A. Young, "Benchmarking of Beyond-CMOS Exploratory Devices for Logic Integrated Circuits," *IEEE J. Explor. Solid-State Comput. Devices Circuits*, vol. 1, pp. 3–11, Dec. 2015.

[6]   J. Sun, "Spin-current interaction with a monodomain magnetic body: A model study," *Phys. Rev. B*, vol. 62, no. 1, pp. 570–578, 2000.

[7]   K. Komagaki *et al.*, "Influence of diffused boron into MgO barrier on pinhole creation in CoFeB/MgO/CoFeB magnetic tunnel junctions," *IEEE Trans. Magn.*, vol. 45, no. 10, pp. 3453–3456, 2009.

[8]   M. Lakshmanan, "The fascinating world of the Landau–Lifshitz–Gilbert equation: an overview," *Philos. Trans. R. Soc. A Math. Phys. Eng. Sci.*, vol. 369, no. 1939, pp. 1280–1300, Mar. 2011.

[9]   L. Berger, "Emission of spin waves by a magnetic multilayer traversed by a current," *Phys. Rev. B - Condens. Matter Mater. Phys.*, vol. 54, no. 13, pp. 9353–9358, Oct. 1996.

[10]   E. Beaurepaire, J. C. Merle, A. Daunois, and J. Y. Bigot, "Ultrafast spin dynamics in ferromagnetic nickel," *Phys. Rev. Lett.*, vol. 76, no. 22, pp. 4250–4253, 1996.

[11]   A. Kirilyuk, A. V. Kimel, and T. Rasing, "Ultrafast optical manipulation of magnetic order," *Rev. Mod. Phys.*, vol. 82, no. 3, pp. 2731–2784, 2010.

[12]   C. D. Stanciu *et al.*, "All-optical magnetic recording with circularly polarized light," *Phys. Rev. Lett.*, vol. 99, no. 4, pp. 1–4, 2007.

[13] V. I. Belotelov, E. A. Bezus, L. L. Doskolovich, A. N. Kalish, and A. K. Zvezdin, "Inverse Faraday effect in plasmonic heterostructures," *J. Phys. Conf. Ser.*, vol. 200, no. SECTION 9, 2010.

[14] S. M. Hamidi, M. Razavinia, and M. M. Tehranchi, "Enhanced optically induced magnetization due to inverse Faraday effect in plasmonic nanostructures," *Opt. Commun.*, vol. 338, pp. 240–245, 2015.

[15] T. M. Liu *et al.*, "Nanoscale Confinement of All-Optical Magnetic Switching in TbFeCo - Competition with Nanoscale Heterogeneity," *Nano Lett.*, vol. 15, no. 10, pp. 6862–6868, 2015.

[16] A. R. Khorsand *et al.*, "Role of magnetic circular dichroism in all-optical magnetic recording," *Phys. Rev. Lett.*, vol. 108, no. 12, p. 127205, Mar. 2012.

[17] A. Dutta, A. V. Kildishev, V. M. Shalaev, A. Boltasseva, and E. E. Marinero, "Surface-plasmon opto-magnetic field enhancement for all-optical magnetization switching," *Opt. Mater. Express*, vol. 7, no. 12, p. 4316, Dec. 2017.

[18] K. Garello *et al.*, "Ultrafast magnetization switching by spin-orbit torques," *Appl. Phys. Lett.*, vol. 105, no. 21, p. 212402, Nov. 2014.

[19] G. Prenat *et al.*, "Ultra-Fast and High-Reliability SOT-MRAM: From Cache Replacement to Normally-Off Computing," *IEEE Trans. Multi-Scale Comput. Syst.*, vol. 2, no. 1, pp. 49–60, Jan. 2016.

[20] J. Železný *et al.*, "Relativistic néel-order fields induced by electrical current in antiferromagnets," *Phys. Rev. Lett.*, vol. 113, no. 15, p. 157201, Oct. 2014.

[21] P. E. Roy, R. M. Otxoa, and J. Wunderlich, "Robust picosecond writing of a layered antiferromagnet by staggered spin-orbit fields," *Phys. Rev. B*, vol. 94, no. 1, p. 014439, Jul. 2016.

[22] S. Wienholdt, D. Hinzke, and U. Nowak, "THz switching of antiferromagnets and ferrimagnets," *Phys. Rev. Lett.*, vol. 108, no. 24, p. 247207, Jun. 2012.

[23] H. Zhong, S. Qiao, S. Yan, L. Liang, Y. Zhao, and S. Kang, "Terahertz spin-transfer torque oscillator based on a synthetic antiferromagnet," *J. Magn. Magn. Mater.*, vol. 497, p. 166070, Mar. 2020.

[24] S. Parkin, X. Jiang, C. Kaiser, A. Panchula, K. Roche, and M. Samant, "Magnetically engineered spintronic sensors and memory," *Proc. IEEE*, vol. 91, no. 5, pp. 661–679, 2003.

[25] S. S. P. Parkin *et al.*, "Giant tunnelling magnetoresistance at room temperature with MgO (100) tunnel barriers," *Nat. Mater.*, vol. 3, no. 12, pp. 862–867, Dec. 2004.

[26] D. Watanabe and Et Al., "Interlayer exchange coupling in perpendicularly magnetized synthetic ferrimagnet structure using CoCrPt and CoFeB," *J. Phys. Conf. Ser.*, vol. 200, no. 7, p. 72104, 2010.

[27] S. Bandiera *et al.*, "Comparison of synthetic antiferromagnets and hard ferromagnets as reference layer in magnetic tunnel junctions with perpendicular magnetic anisotropy," *IEEE Magn. Lett.*, vol. 1, pp. 1–4, 2010.

[28] C. Augustine, A. Raychowdhury, D. Somasekhar, J. Tschanz, K. Roy, and V. K. De, "Numerical analysis of typical STT-MTJ stacks for 1T-1R memory arrays," in *Technical Digest - International Electron Devices Meeting, IEDM*, 2010.

[29] J. Hayakawa *et al.*, "Current-induced magnetization switching in MgO barrier magnetic tunnel junctions with CoFeB-based synthetic ferrimagnetic free layers," in *IEEE Transactions on Magnetics*, 2008, vol. 44, no. 7, pp. 1962–1967.

[30] P. Grünberg, R. Schreiber, Y. Pang, M. B. Brodsky, and H. Sowers, "Layered Magnetic Structures: Evidence for Antiferromagnetic Coupling of Fe Layers across Cr Interlayers," *Phys. Rev. Lett.*, vol. 57, no. 19, pp. 2442–2445, Nov. 1986.

[31] S. S. P. Parkin, N. More, and K. P. Roche, "Oscillations in Exchange Coupling and Magnetoresistance in Metallic Superlattices Structures: Cu/Ru, Co/Cr and Fe/Cr," *Physical Review Letters*, vol. 64, no. 19. pp. 2304–2308, 1990.

[32] S. S. P. Parkin, "Systematic Variation of the Strength and Oscillation Period of Indirect Magnetic Exchange Coupling through the 3d, 4d, 5d Transition Metals," vol. 67, no. 25, pp. 3598–3601, 1991.

[33] S. S. P. Parkin and D. Mauri, "Spin engineering: Direct determination of the Ruderman-Kittel-Kasuya-Yosida far-field range function in ruthenium," *Phys. Rev. B*, vol. 44, no. 13, pp. 7131–7134, Oct. 1991.

[34] A. Barthélémy *et al.*, "Magnetic and transport properties of Fe/Cr superlattices (invited)," *J. Appl. Phys.*, vol. 67, no. 9, pp. 5908–5913, May 1990.

[35] K. Y. Camsari, A. Z. Pervaiz, R. Faria, E. E. Marinero, and S. Datta, "Ultrafast Spin-Transfer-Torque Switching of Synthetic Ferrimagnets," *IEEE Magn. Lett.*, vol. 7, no. 99, pp. 1–5, 2016.

[36]   T. R. Albrecht *et al.*, "Bit patterned media at 1 Tdot/in2 and beyond," *IEEE Trans. Magn.*, vol. 49, no. 2, pp. 773–778, 2013.

[37]   T. Keitoku, J. Ariake, N. Honda, and K. Ouchi, "Preparation of Co-Cr-Pt alloy film with high perpendicular coercivity and large negative nucleation field," *J. Magn. Magn. Mater.*, vol. 235, no. 1–3, pp. 34–39, 2001.

[38]   T. Shimatsu *et al.*, "High perpendicular magnetic anisotropy of CoPtCr/Ru films for granular-type perpendicular media," *IEEE Trans. Magn.*, vol. 40, no. 4 II, pp. 2483–2485, 2004.

[39]   S. N. Piramanayagam, "Perpendicular recording media for hard disk drives," *J. Appl. Phys.*, vol. 102, no. 1, 2007.

[40]   A. W. Hull, "X-Ray crystal analysis of thirteen common metals," *Phys. Rev.*, vol. 17, no. 5, pp. 571–588, May 1921.

[41]   C. L. Platt, K. W. Wierman, E. B. Svedberg, T. J. Klemmer, J. K. Howard, and D. J. Smith, "Structural and magnetic properties of CoCrPt perpendicular media grown on different buffer layers," *J. Magn. Magn. Mater.*, vol. 247, no. 2, pp. 153–158, Jun. 2002.

[42]   D. Watanabe, S. Mizukami, M. Oogane, H. Naganuma, Y. Ando, and T. Miyazaki, "Fabrication of MgO-based magnetic tunnel junctions with CoCrPt perpendicularly magnetized electrodes," *J. Appl. Phys.*, vol. 105, no. 7, pp. 126–129, 2009.

[43]   A. Inomata, E. N. Abarra, B. R. Acharya, H. Akimoto, and I. Okamoto, "Exchange coupling strength in synthetic ferrimagnetic media," in *IEEE Transactions on Magnetics*, 2001, vol. 37, no. 4 I, pp. 1449–1451.

[44]   D. C. Worledge and P. L. Trouilloud, "Magnetoresistance measurement of unpatterned magnetic tunnel junction wafers by current-in-plane tunneling," *Appl. Phys. Lett.*, vol. 83, no. 1, pp. 84–86, 2003.

[45] M. N. Baibich *et al.*, "Giant Magnetoresistance of (001)Fe/(001)Cr Magnetic Superlattices," *Phys. Rev. Lett.*, vol. 61, no. 21, pp. 2472–2475, Nov. 1988.

[46]   G. Binasch, P. Grünberg, F. Saurenbach, and W. Zinn, "Enhanced magnetoresistance in layered magnetic structures with antiferromagnetic interlayer exchange," *Phys. Rev. B*, vol. 39, no. 7, pp. 4828–4830, 1989.

[47] S. Yakata *et al.*, "Thermal stability and spin-transfer switchings in MgO-based magnetic tunnel junctions with ferromagnetically and antiferromagnetically coupled synthetic free layers," *Appl. Phys. Lett.*, vol. 95, no. 24, Dec. 2009.

[48] S. Ikeda *et al.*, "Tunnel magnetoresistance of 604% at 300 K by suppression of Ta diffusion in CoFeBMgOCoFeB pseudo-spin-valves annealed at high temperature," *Appl. Phys. Lett.*, vol. 93, no. 8, 2008.

[49] O. Koplak *et al.*, "Magnetization switching diagram of a perpendicular synthetic ferrimagnet CoFeB/Ta/CoFeB bilayer," *J. Magn. Magn. Mater.*, vol. 433, pp. 91–97, 2017.

[50] B. Beauchamp and E. E. Marinero, "Temperature-dependent Magnetic Transitions in CoCrPt-Ru-CoCrPt Synthetic Ferrimagnets," Apr. 2020.

[51] R. B. Morgunov *et al.*, "Influence of the magnetic field sweeping rate on magnetic transitions in synthetic ferrimagnets with perpendicular anisotropy," *Appl. Phys. Lett.*, vol. 114, no. 22, Jun. 2019.

[52] J. B. Staunton, L. Szunyogh, A. Buruzs, B. L. Gyorffy, S. Ostanin, and L. Udvardi, "Temperature dependence of magnetic anisotropy: An ab initio approach," *Phys. Rev. B - Condens. Matter Mater. Phys.*, vol. 74, no. 14, p. 144411, Oct. 2006.

[53] B. D. Cullity and C. D. Graham, *Introduction to Magnetic Materials*. Hoboken, NJ, USA: John Wiley & Sons, Inc., 2008.

[54] A. V Kimel, B. A. Ivanov, R. V Pisarev, P. A. Usachev, A. Kirilyuk, and T. Rasing, "Inertia-driven spin switching in antiferromagnets," *Nat. Phys.*, 2009.

[55] J. Y. Chin *et al.*, "Nonreciprocal plasmonics enables giant enhancement of thin-film Faraday rotation," *Nat. Commun.*, vol. 4, pp. 1596–1599, 2013.

[56] D. K. Gramotnev and S. I. Bozhevolnyi, "Plasmonics beyond the diffraction limit," *Nature Photonics*, vol. 4, no. 2. Nature Publishing Group, pp. 83–91, Feb-2010.

[57] U. Guler, V. M. Shalaev, and A. Boltasseva, "Nanoparticle plasmonics: Going practical with transition metal nitrides," *Materials Today*, vol. 18, no. 4. Elsevier, pp. 227–237, 01-May-2015.

[58] U. Guler, A. Boltasseva, and V. M. Shalaev, "Refractory plasmonics," *Science*, vol. 344, no. 6181. American Association for the Advancement of Science, pp. 263–264, 18-Apr-2014.

[59] W. Li *et al.*, "Refractory Plasmonics with Titanium Nitride: Broadband Metamaterial Absorber," *Adv. Mater.*, vol. 26, no. 47, pp. 7959–7965, Dec. 2014.

[60] A. Kossoy, V. Merk, D. Simakov, K. Leosson, S. Kéna-Cohen, and S. A. Maier, "Optical and Structural Properties of Ultra-thin Gold Films," *Adv. Opt. Mater.*, vol. 3, no. 1, pp. 71–77, Jan. 2015.

[61] H. Liu *et al.*, "Enhanced surface plasmon resonance on a smooth silver film with a seed growth layer," *ACS Nano*, vol. 4, no. 6, pp. 3139–3146, Jun. 2010.

[62] D. Shah, H. Reddy, N. Kinsey, V. M. Shalaev, and A. Boltasseva, "Optical Properties of Plasmonic Ultrathin TiN Films," *Adv. Opt. Mater.*, vol. 5, no. 13, p. 1700065, Jul. 2017.

[63] O. Hellwig *et al.*, "Bit patterned media optimization at 1 Tdot/in ^{2} by post-annealing," *J. Appl. Phys.*, vol. 116, no. 12, p. 123913, Sep. 2014.

[64] S. Hashimoto and Y. Ochiai, "Co/Pt and Co/Pd multilayers as magneto-optical recording materials," *J. Magn. Magn. Mater.*, vol. 88, no. 1–2, pp. 211–226, Jul. 1990.

[65] W. C. Chen, C. Y. Peng, and L. Chang, "Heteroepitaxial growth of TiN film on MgO (100) by reactive magnetron sputtering," *Nanoscale Res. Lett.*, vol. 9, no. 1, pp. 1–5, Oct. 2014.

[66] S. Mizukami *et al.*, "Laser-induced fast magnetization precession and gilbert damping for CoCrPt alloy thin films with perpendicular magnetic anisotropy," *Appl. Phys. Express*, vol. 3, no. 12, p. 123001, Dec. 2010.

[67] M. F. Toney, E. E. Marinero, M. F. Doerner, and P. M. Rice, "High anisotropy CoPtCrB magnetic recording media," *J. Appl. Phys.*, vol. 94, no. 6, pp. 4018–4023, Sep. 2003.

[68] I. S. Lee and D. W. Kim, "Magnetic properties and domain patterns of CoCrPtTa perpendicular films with Ta content," *Thin Solid Films*, vol. 388, no. 1–2, pp. 245–250, Jun. 2001.

[69] W. R. Eppler and M. H. Kryder, "Garnets for short wavelength magneto-optic recording," *J. Phys. Chem. Solids*, vol. 56, no. 11, pp. 1479–1490, Nov. 1995.

[70] T. Tepper and C. A. Ross, "Pulsed laser deposition and refractive index measurement of fully substituted bismuth iron garnet films," *J. Cryst. Growth*, vol. 255, no. 3–4, pp. 324–331, 2003.

[71] A. Barman, S. Wang, O. Hellwig, A. Berger, E. E. Fullerton, and H. Schmidt, "Ultrafast magnetization dynamics in high perpendicular anisotropy [CoPt]n multilayers," in *Journal of Applied Physics*, 2007, vol. 101, no. 9, p. 09D102.

[72] S. Pal, B. Rana, O. Hellwig, T. Thomson, and A. Barman, "Tunable magnonic frequency and damping in [Co/Pd]8 multilayers with variable Co layer thickness," *Appl. Phys. Lett.*, vol. 98, no. 8, p. 082501, Feb. 2011.

[73] T. Kato *et al.*, "Perpendicular anisotropy and gilbert damping in sputtered Co/Pd multilayers," *IEEE Trans. Magn.*, vol. 48, no. 11, pp. 3288–3291, 2012.

[74] C. H. Lambert *et al.*, "All-optical control of ferromagnetic thin films and nanostructures," *Science (80-.).*, vol. 345, no. 6202, pp. 1337–1340, Sep. 2014.

[75] B. X. Gu, "Magnetic properties and magneto-optical effect of Co0.5Fe2.5O4 nanostructured films," *Appl. Phys. Lett*, vol. 82, p. 3707, 2003.

[76] E. Takeda *et al.*, "Faraday effect enhancement in Co–ferrite layer incorporated into one-dimensional photonic crystal working as a Fabry–Pérot resonator," in *Journal of Applied Physics*, 2000, vol. 87, no. 9, pp. 6782–6784.

[77] A. Masuda, K. Matsuda, Y. Yonezawa, A. Morimoto, and T. Shimizu, "Mechanism of stoichiometric deposition of volatile elements in multimetal-oxide films prepared by pulsed laser ablation," *Japanese J. Appl. Physics, Part 2 Lett.*, vol. 35, no. 2 B, 1996.

[78] J. Y. Chen, L. He, J. P. Wang, and M. Li, "All-Optical Switching of Magnetic Tunnel Junctions with Single Subpicosecond Laser Pulses," *Phys. Rev. Appl.*, vol. 7, no. 2, p. 021001, Feb. 2017.

PUBLICATIONS

Under review: B. Beauchamp, E.E. Marinero, Temperature-dependent Magnetic Transitions in CoCrPt-Ru-CoCrPt Synthetic Ferrimagnets, (2020). http://arxiv.org/abs/2004.11406.

Under review: A. Chu, B. Beauchamp, D. Shah, A. Dutta, A. Boltasseva, V. Shalaev, E.E. Marinero, Hybrid Magneto Photonic Material Structure for Plasmon Assisted Magnetic Switching, (2020). https://arxiv.org/abs/2006.09524